UNIVERSITÀ DEGLI STUDI DI VERONA

SCIENZE CHIRURGICHE ODONSTOMOLOGICHE E MATERNO-INFANTILI
SCUOLA DI DOTTORATO DI SCIENZE DELLA VITA E DELLA SALUTE
DOTTORATO DI RICERCA IN SCIENZE CARDIOVASCOLARI

NOVEL STRATEGIES FOR THE MORPHOLOGICAL AND BIOMECHANICAL ANALYSIS OF THE CARDIAC VALVES BASED ON VOLUMETRIC CLINICAL IMAGES

S.S.D. ING-IND/34

Tutor:
Prof. GIOVANNI LUCIANI

Advisors:
Prof. EMILIANO VOTTA
Dott. FRANCESCO ONORATI
Prof. ALBERTO REDAELLI

Supervisor of the Ph.D. Program:
Prof. GIOVANNI LUCIANI

Ph.D. Candidate:
OMAR ANTONIO PAPPALARDO

XXX Cycle

Contents

Abstract

Introduction

In the western-countries, approximately 2% of the population is affected by valvular heart diseases[1]. These pathologies can be classified in stenotic or regurgitant depending on the disease phenotype. In both cases the diagnosis is performed mainly through the 2D echocardiography[2], even though cardiac structures are characterized by complex dynamic 3D geometries. Several studies demonstrated that 3D echocardiography can better describe the 3D complex morphology of heart valves, as compared to 2D echocardiography[3–6]. However, the information yielded by volumetric imaging data has not been yet standardized in clinics, most likely due to limited availability of such technologies in the clinical routine, as well as due to limited operators experience and post-processing tools. For these reasons, volumetric imaging has not been yet fully exploited.

Moreover, the use and the importance of volumetric imaging data, such as 3D echocardiography and multi detector computed tomography, has been growing dragged by the increase of transcatheter devices implants[7], which require patient selection, pre-procedural planning and procedure guidance. These steps are commonly performed through the use of medical imaging to overcome the lack of direct view and access to the cardiac structures during operation. In this evolving scenario, the use of the 3D imaging is mandatory and pivotal in the interventional cardiology field[8]. In particular, 3D imaging modalities can provide detailed information on the dimensions and spatial relationships of the cardiac structures that are crucial to choose the best suited treatment including device size and the procedural approach[8].

Numerous commercial and custom software have been developed and used for the analysis of data derived from 3D echocardiography[9–13], whereas for computed tomography data the procedural planning still consists in the navigation of the full 3D volume through 2D cut planes [14,15].

A further advancement of the pre-procedural planning phase could be accomplished exploiting numerical tools to perform biomechanical simulations. These could be beneficial in computing the effects of surgical or percutaneous procedures, also comparing different implantation techniques or different devices.

In the recent years, numerous works based on finite element simulations (considered as the gold-standard) focused on computing the effects of surgical or percutaneous techniques on the mitral valve apparatus[16–20], reconstructing patient-specific 3D geometries and working conditions of the valve leaflets and sub-structures. However, these numerical simulations rarely include proper mechanical characterizations of pathological tissues, and they also over-simplify the geometrical features of the involved structures (e.g., leaflets thickness).

Moreover, the vast majority of the numerical tools developed so far still require a huge amount of computational expense and time-demand, being far from practical application in the clinical routine. Only few works proposed alternative approaches to the finite element analysis in the attempt of reducing computational demands, but none of them proved the accuracy of such methods vs. finite element analysis[21–23].

In the previously described scenario, the first aim of this work was the standardization of the analyses of volumetric imaging data by defining a single segmentation process of heart valves regardless of the imaging modality input, and the development of valve-specific algorithms to automatically define the 3D geometry of the analyzed cardiac structure.

The second aim was the implementation of automated approaches for the quantification of clinically-relevant variables and diagnostic markers. In specific, the activities were focused on the computation of the aortic valve opening area considering the entire 3D geometry of the leaflets, on the quantification of the spatial relationship between the tricuspid valve and the right coronary artery and on the assessment of the thickness pattern and mechanical behavior of the myxomatous leaflet tissue.

Finally, the last aim was the advancement of the biomechanical simulation regarding the mitral valve, following a twofold approach: on the one hand, by improving the realism of the models adopted for the biomechanical characterization of valve tissues, while, on the other hand, by decreasing the computational demand of numerical simulations by implementing ad-hoc mass-spring models.

Main findings

This work was focused on the morphological and biomechanical analysis of the heart valves exploiting the volumetric data.

Novel methods were implemented to perform cardiac valve structure and sub-structure segmentation by defining long axis planes evenly rotated around the long axis of the valve. These methods were exploited to successfully reconstruct the 3D geometry of the mitral, tricuspid and aortic valve structures. Firstly, the reconstructed models were used for the morphological analysis providing a detailed description of the geometry of the valve structures, also computing novel indexes that could improve the description of the valvular apparatus and help their clinical assessment. Additionally, the models obtained for the mitral valve complex were adopted for the development of a novel biomechanical approach to simulate the systolic closure of the valve, relying on highly-efficient mass-spring models thus obtaining a good trade-off between the accuracy and the computational cost of the numerical simulations.

In specific:

- First, an innovative and semi-automated method was implemented to generate the 3D model of the aortic valve and of its calcifications, to quantitively describe its 3D morphology and to compute the anatomical aortic valve area (AVA) based on multi-detector computed tomography images. The comparison of the obtained results vs. effective AVA measurements showed a good correlation. Additionally, these methods accounted for asymmetries or anatomical derangements, which would be difficult to correctly capture through either effective AVA or planimetric AVA.
- Second, a tool to quantitively assess the geometry of the tricuspid valve during the cardiac cycle using multidetector CT was developed, in particular focusing on the 3D spatial relationship between the tricuspid annulus and the right coronary artery. The morphological analysis of the annulus and leaflets confirmed data reported in literature. The qualitative and quantitative analysis of the spatial relationship could standardize the analysis protocol and be pivotal in the procedure planning of the percutaneous device implantation that interact with the tricuspid annulus.
- Third, we simulated the systolic closure of three patient specific mitral valve models, derived from CMR datasets, by means of the mass spring model approach. The comparison of the obtained results vs. finite element analyses (considered as the gold-standard) was performed tuning the parameters of the mass spring model, so to obtain the best trade-off between computational expense and accuracy of the results. A configuration mismatch between the two models lower than two times the in-plane resolution of starting imaging data was yielded using a mass spring model set-up that requires, on average, only ten minutes to simulate the valve closure.

- Finally, in the last chapter, we performed a comprehensive analysis which aimed at exploring the morphological and mechanical changes induced by the myxomatous pathologies in the mitral valve tissue. The analysis of mitral valve thickness confirmed the data and patterns reported in literature, while the mechanical test accurately described the behavior of the pathological tissue. A preliminary implementation of this data into finite element simulations suggested that the use of more reliable patient-specific and pathology-specific characterization of the model could improve the realism and the accuracy of the biomechanical simulations.

Bibliography

1. Nkomo, V. T. *et al.* Burden of valvular heart diseases: a population-based study. *Lancet* **368,** 1005–1011 (2006).
2. Baumgartner, H. *et al.* 2017 ESC/EACTS Guidelines for the management of valvular heart disease. *Eur. Heart J.* **38,** 2739–2791 (2017).
3. Lang, R. M. *et al.* EAE/ASE Recommendations for Image Acquisition and Display Using Three-Dimensional Echocardiography. *J. Am. Soc. Echocardiogr.* **25,** 3–46 (2012).
4. Muraru, D., Badano, L. P., Vannan, M. & Iliceto, S. Assessment of aortic valve complex by three-dimensional echocardiography: a framework for its effective application in clinical practice. *Eur. Hear. J. - Cardiovasc. Imaging* **13,** 541–555 (2012).
5. Muraru, D., Badano, L. P., Sarais, C., Soldà, E. & Iliceto, S. Evaluation of Tricuspid Valve Morphology and Function by Transthoracic Three-Dimensional Echocardiography. *Curr. Cardiol. Rep.* **13,** 242–249 (2011).
6. Pepi, M. *et al.* Head-to-head comparison of two- and three-dimensional transthoracic and transesophageal echocardiography in the localization of mitral valve prolapse. *J. Am. Coll. Cardiol.* **48,** 2524–30 (2006).
7. Grover, F. L. *et al.* 2016 Annual Report of The Society of Thoracic Surgeons/American College of Cardiology Transcatheter Valve Therapy Registry. *J. Am. Coll. Cardiol.* **69,** 1215–1230 (2017).
8. Delgado, V., van der Kley, F., Schalij, M. J. & Bax, J. J. Optimal imaging for planning and guiding interventions in structural heart disease: a multi-modality imaging approach. *Eur. Hear. J. Suppl.* **12,** E10–E23 (2010).
9. Chandra, S. *et al.* A three-dimensional insight into the complexity of flow convergence in mitral regurgitation: adjunctive benefit of anatomic regurgitant orifice area. *AJP Hear. Circ. Physiol.* **301,** H1015–H1024 (2011).
10. Ton-Nu, T.-T. *et al.* Geometric Determinants of Functional Tricuspid Regurgitation: Insights From 3-Dimensional Echocardiography. *Circulation* **114,** 143–149 (2006).
11. Veronesi, F. *et al.* Effect of mitral valve repair on mitral-aortic coupling: a real-time three-dimensional transesophageal echocardiography study. *J. Am. Soc. Echocardiogr.* **25,** 524–31 (2012).
12. Prihadi, E. A. *et al.* Feasibility, Accuracy, and Reproducibility of Aortic Annular and Root Sizing for Transcatheter Aortic Valve Replacement Using Novel Automated Three-Dimensional Echocardiographic Software: Comparison with Multi–Detector Row Computed Tomography. *J. Am. Soc. Echocardiogr.* (2017). doi:10.1016/j.echo.2017.10.003
13. Levack, M. M. *et al.* Three-Dimensional Echocardiographic Analysis of Mitral Annular Dynamics: Implication for Annuloplasty Selection. *Circulation* **126,** S183–S188 (2012).
14. Clavel, M.-A. *et al.* Aortic Valve Area Calculation in Aortic Stenosis by CT and Doppler Echocardiography. *JACC Cardiovasc. Imaging* **8,** 248–257 (2015).

15. van Rosendael, P. J. *et al.* Computed tomography for planning transcatheter tricuspid valve therapy. *Eur. Heart J.* **38,** ehw499 (2016).

16. Choi, A., Rim, Y., Mun, J. S. & Kim, H. A novel finite element-based patient-specific mitral valve repair: Virtual ring annuloplasty. *Biomed. Mater. Eng.* **24,** 341–347 (2014).

17. Rim, Y., Choi, A., McPherson, D. D. & Kim, H. Personalized computational modeling of mitral valve prolapse: Virtual leaflet resection. *PLoS One* **10,** 1–15 (2015).

18. Sturla, F. *et al.* Biomechanical drawbacks of different techniques of mitral neochordal implantation: When an apparently optimal repair can fail. *J. Thorac. Cardiovasc. Surg.* **150,** 1303–1312 (2015).

19. Sturla, F. *et al.* In vitro and in silico approaches to quantify the effects of the Mitraclip system on mitral valve function. *J. Biomech.* (2016). doi:10.1016/j.jbiomech.2016.11.013

20. Siefert, A. W., Rabbah, J. P. M., Pierce, E. L., Kunzelman, K. S. & Yoganathan, A. P. Quantitative Evaluation of Annuloplasty on Mitral Valve Chordae Tendineae Forces to Supplement Surgical Planning Model Development. *Cardiovasc. Eng. Technol.* **5,** 35–43 (2014).

21. Mansi, T. *et al.* An integrated framework for finite-element modeling of mitral valve biomechanics from medical images: Application to MitralClip intervention planning. *Med. Image Anal.* **16,** 1330–1346 (2012).

22. Sprouse, C., Mukherjee, R. & Burlina, P. Mitral valve closure prediction with 3-d personalized anatomical models and anisotropic hyperelastic tissue assumptions. *IEEE Trans. Biomed. Eng.* **60,** 3238–3247 (2013).

23. Hammer, P. E., Vasilyev, N. V., Perrin, D. P., Nido, P. J. del & Howe, R. D. Fast Image-based Model of Mitral Valve Closure for Surgical Planning. *MICCAI Work.* **6918,** 1–8 (2008).

Chapter 1

Introduction

1.1 Anatomy

1.1.1 Heart

The cardiovascular system consists of a closed circuit composed of arteries, arterioles, capillaries, venules, veins and the heart. Blood flow within the cardiovascular system is guided by the mechanical force exerted by the heart, which muscle fibers alternatively contract and relax to push blood towards peripheral vessels and to allow its passive return. The mechanisms involved in the contraction and relaxation of the heart are characterized by high complexity, in terms of electrical-chemical-mechanical interplay that regulates the functioning of the pumping apparatus and of the anatomical structures involved. The heart can be schematically represented as a series of two different pumps, i.e., left and right pump, each divided into two chambers (atrium and ventricle) that manage systemic (left pump) and pulmonary circulation (right pump). Inside the heart's cavities, unidirectional blood flow is controlled by the four heart valves: the mitral and tricuspid (atrio-ventricular) valves and the pulmonary and aortic (semilunar) valves. The former two are between the atria to the ventricles, whereas the semilunar valves allow the blood for leaving the ventricle towards the arteries.

1.1.2 Mitral Valve

The mitral valve (MV) is located on the left side of the heart and prevents systolic backflow from the left ventricle to the left atrium. The MV complex is composed by the mitral annulus (MA), two leaflets (anterior and posterior), the chordae tendineae and the papillary muscles (PMs).

The MA is a fibroelastic ring with a 3D saddle shape and its geometry can be divided into anterior (one-third) and posterior (two-thirds) portions. The former is mostly fibrous (collagen fibers) since it is continuous with the aortic annulus, identifying the “horn” of the saddle; the latter is more loosely anchored to the surrounding tissue, allowing it to move during myocardial contraction and relaxation[1]. The structure of the MA features three-dimensional deformation during the cardiac cycle, thus experiencing changes in circumference, excursion, curvature, shape and size, which in turn makes it susceptible to ventricular remodeling[2]. This 3D dynamic conformation has been shown to lessen mechanical stress exerted on the MV leaflets during systole and improve leaflet coaptation[3].

The anterior and posterior MV leaflets are delimited by the antero-lateral and the postero-medial commissures, basically located on the MA posterior portion at the lowest points of the saddle in proximity to the two fibrous trigones. Each leaflet presents a series of segments, leading to the standard nomenclature for the A1 (anterior), A2 (middle) and A3 (posterior) segments for the anterior leaflet and an analogous set of scallops (P1, P2, P3) for the posterior leaflet. The anterior mitral leaflet commonly has a trapezoid-like shape and is larger, longer and thicker than the posterior one, which is relatively short in the annulus-free margin direction but with a larger circumferential base. Nearby the commissures, leaflets' tissue achieves its minimum extension (0.5-1 cm), whereas it is redundant in the middle allowing for leaflets apposition and tight coaptation[4].

The chordae tendineae are fibrous (linked collagen and elastin network) strings that originate with highly variable branching from the PM tips and insert fan-like into the leaflets[5,6]. Primary (or marginal) chords attach to the free edge of the rough zone of both leaflets; secondary (or basal) chords, thicker and more extensible, attach to the ventricular surface in the region of the rough zone (i.e. body of the leaflet). Occasionally, chordae originate directly from ventricular wall, namely tertiary ones.

The remaining structures in the sub-valvular apparatus are the two papillary muscles (PMs), originating from the left ventricular wall in the apical region, beneath the commissures, which they are named after as antero-lateral and postero-medial PM, respectively. The former has typically a single head whereas the latter is commonly double-headed. The interplay of both the PMs and the chordae aim to physiologically avoid the billowing of the MV towards the atrium, determining the configuration and tension state of each leaflet at end-systole.

When such a mutual mechanism is altered, a MV prolapse commonly occurs. The prolapse is a common MV disease, affecting almost the 3% of the general population[7] and it is defined as the abnormal displacement of one or both leaflets into the atrium, resulting in varying degrees of MV regurgitation[8]. The etiology can rely on a degeneration of the valve tissue (named *degenerative* or *primary* MV regurgitation) or be related to a heart muscle damage or to a ventricular remodeling in size/shape (named *functional* or *secondary* MV regurgitation). Being the former the most frequent[9], it typically has two main histological phenotypes: diffuse myxomatous degeneration (Barlow's Disease, BD) and fibroelastic deficiency (FED).

1.1.3 Tricuspid Valve

The tricuspid valve (TV) is located on the right side of the heart and allows blood flow from the right atrium to the right ventricle. It is the largest and most apically positioned cardiac valve[10] and, similarly to MV, is composed by the tricuspid annulus (TA), the three leaflets (anterior, posterior and septal), the chordae tendineae and the papillary muscles (PMs).

The tricuspid annulus (TA), or hinge line, defines the junction between the right atrial and right ventricular myocardium and it pinpoints the attachment line where the leaflets insert on. The TA is a non-planar structure with an oval saddle shape, being the highest and lowest points nearby the antero-septal and postero-septal commissures, respectively[11,12]. As MA, even the TA 3D conformation is continuously changing during the cardiac cycle[13]; there is normally a reduction of 19% in annular circumference with atrial systole[14,15]. A permanent alteration in TA configuration occurs when TV functional regurgitation arises, progressively becoming more circular and flatter[16,17].

Although the term ‘annulus’ confers the impression of a well formed fibrous ring-like structure separating atrial from ventricular myocardium, the TV leaflets are actually attached to a poorly formed fibrous annulus that is not as clear to delineate as with MV[18]. The tricuspid annulus is larger than the mitral annulus[19] and in low-pressure pulmonary environment the leaflets are thinner and more translucent[20]. The anterior leaflet is the largest and most mobile of the three leaflets with a semi-circular shape, the septal leaflet is the least mobile with a semi-oval shape and the posterior leaflet is the smallest one featuring variable shape[21]. The commissures are generally identified as the TA profile indentations[16].

The TV sub-valvular apparatus is similar to the MV one but has greater variability. It consists of three PMs: i) anterior (the most prominent) which provides chordae to anterior and posterior leaflet; ii) posterior (missing in 20% of healthy population[22]) that gives chordae to posterior and septal cusps; iii) septal, which mostly does not feature any specific tip, being the chordae directly arising from ventricular wall toward anterior and septal leaflets.

1.1.4 Aortic Valve

The aortic root is defined as the first outflow tract from left ventricle to the ascending aorta. Its components are the sinuses of Valsalva, the fibrous interleaflet triangles, and the three aortic valve (AV) leaflets. The latter originate from the supporting left ventricular structures, which makes difficult the definition of an aortic “annulus” since there is not such discrete anatomic structure[23]. However, a practical surgical definition of the aortic valve annulus is the semi-lunar crown-like structure delimited by the hinges of the leaflets[24]. The three peaks of the annulus profile delimited the three cusp of the valve that are named according to the corresponding coronary vessels, namely left, right and non-coronary. Each cusp is attached to the wall of the aorta by the outward edges of its semicircular border. The level at which this attachment occurs is known as the sinotubular junction, where the three commissures can be pinpointed as the points where insertions line of adjacent cusps meet each other. Finally, just above the AV, arising from the respective Valsalva sinus, left (LCA) and right (RCA) coronary artery supply blood to the myocardium itself, running nearby the annular plane.

Even the AV complex is a dynamic structure, with its principal dimensions changing continuously during the phases of the cardiac cycles according to loading pressure regime inside the aortic root. Towards systolic peak, AV annulus diameter has been noted to decrease by 16%[25].

1.2 Imaging Modalities

Medical imaging technologies are crucial in every day clinical practice (i.e., diagnosis, prognosis) as well as in the research fields. The entire clinical workflow targeted for treatment of cardiovascular disease, including assessment, planning, and therapy guidance, relies on qualitative and quantitative analysis of several types of images.

1.2.1 Cardiac Computed Tomography

Cardiac computed tomography (cardiac CT) is a procedure that uses a special X-ray machine to generate detailed images of the heart. During the cardiac CT scan the X-ray tube rotates around the body to acquire multiple images from different angles and combines them to reconstruct three-dimensional volumes of the heart.

A Computed Tomography Angiography (CTA) procedure uses Iodine-based contrast dye injected into veins while scanning to highlight blood vessels and soft tissue areas. Each portion of the heart can be scanned at several phases of the cardiac cycle. Retrospective Electrocardiography (ECG) gating is used to correlate the CT data with the corresponding phase and reconstruct a series of volumes which cover a complete cardiac cycle (Multiphase CT or CTA). New scanners, as the SOMATOM Definition Flash CT, Siemens Healthcare, Forchheim, Germany, achieve a temporal resolution of 75 milliseconds and require 0.6 seconds for a complete thorax scan at a radiation dose of 1 millisievert (mSv).

The main limitation of cardiac CT is the radiation caused by the X-rays. Nevertheless, due to its relatively high spatial resolution, this imaging modality provides accurate morphologic rendering of the heart, which is useful in various clinical scenarios such as calcium assessment and scoring, or the visualization of the coronary arteries. Cardiac CT is reliable in depicting the aortic and mitral valve in contrast enhanced CTA procedures. It has been reported that CT imaging can quantify the mitral regurgitant orifice as well as the mitral valve morphology[26]. Recent studies demonstrated the usage of CTA to measure the orifice area in normal and stenotic aortic valves in close correlation with Transesophageal Echocardiography[23]. As regards the right heart investigation, CT has been found to provide high-resolution anatomical evaluation as well as accurate functional assessment without any geometric assumptions[27].

Multi-slice computed tomography (MSCT) may contribute to evaluation of the severity of valve heart disease (VHD), particularly in aortic stenosis[28,29], and of the thoracic aorta. MSCT plays a key role in the workup of patients with VHD considered for transcatheter intervention, in particular transcatheter aortic valve implantation (TAVI), and provides valuable information for pre-procedural planning.

1.2.2 Cardiovascular Magnetic Resonance

Cardiac magnetic resonance (CMR) imaging uses a high-strength magnetic field, mainly 1.5 Tesla, to excite hydrogen nuclei within a body region by a pulse of radio waves, at a resonance frequency of 63MHz. Images are built from wave echoes emitted during excitation decay, while contrast arises from different particle concentration of individual tissues. Discrimination between blood and myocardium tissue is possible in arbitrary planes without contrast medium.

After growing considerably over the past years, CMR is now firmly established in large centers and considered the most versatile non-invasive diagnostic modality. It enables high-resolution static and moving images of cardiac structures when combined with ECG synchronization. Furthermore, phase-contrast protocols produce velocity-encoded images of the blood flow. The nonionizing technology offers CMR a fundamental advantage compared to X-ray and gamma ray modalities. Nevertheless, relative long examination times of 45-90min, compared to 15min for CT studies, obstruct CMR application for full 4D imaging.

CMR offers invaluable information about the valvular anatomy and function. It is the modality of choice for the analysis of dilated aorta with aortic regurgitation and most accurate to evaluate ventricular function[30]. It is ideally suited in pediatric cardiology to assess complex congenital heart disease of the valves and great vessels. Since it is flow-based imaging sequence, CMR even allows for assessment of valvular and hemodynamic abnormalities[27], such as tricuspid regurgitation.

1.2.3 Echocardiography

Echocardiography is the principal imaging modality to evaluate all cardiovascular disease related to morphological, functional or hemodynamic dysfunctions[31] . Echocardiography is based on ultrasound technology, which uses a transducer loaded with an array or matrix of piezo-electric elements to generate ultrasound pulses, with a frequency between 1-15MHz. These traverse the human body and produce echoes captured by the device to assemble images. The result is a virtually risk-free, non-invasive imaging modality, which in comparison with other techniques, such as CT or MRI, is cost-effective and widely available in most clinical units.

The downsides of ultrasound are low signal-to-noise ratio due to tissue frequency attenuation, artifacts caused by echo dropouts and speckle noise as well as suboptimal acoustic windows and insufficient depth penetration, which overall lead to limited image quality. Nevertheless, a wide range of techniques were developed to overcome these limitations and enable ultrasound technology not only for diagnosis, but also to guide interventional procedures, such as valve replacement or repair, or apply therapy for example in fragmentation of kidney and gall bladder stones.

Transthoracic Echocardiography (TTE) - the ultrasound transducer is coupled to the skin surface using a special gel and angulated to obtain images from four standard positions: parasternal, apical, subcostal and suprasternal. TTE is the standard diagnostic method for patients with valvular heart disease, as it provides quantitative and qualitative information about the anatomy and function of the valves, as well as the etiology and severity of valvular stenosis and regurgitation[32]. Evaluation usually includes aortic and mitral valve area, LV volume, mass and ejection fraction, aortic root anatomy and right heart structure and function.

Transesophageal Echocardiography (TEE) - To obtain images from the proximity of the major cardiovascular structures, a special probe is introduced in the esophagus during the exam. TEE provides high-resolution images and is considered essential in many cases including studies in presence of prosthetic valves or evaluation of mitral valve and aortic lesions and regurgitant severity. Recently introduced real-time 3D scanners enable unique perspective and time resolved imaging of the valves, which advance visualization and quantification capabilities and improve severity assessment and treatment planning[31].

Doppler and Color Flow Imaging - Doppler echocardiography quantifies blood flow velocity based on the shift in frequency of the reflected ultrasound waves, a phenomenon known as the Doppler Effect. In color flow imaging, the measured blood velocities are color coded and displayed superimposed to the anatomical echo images. Doppler provides essential measurement in VHD assessment, including regurgitant volumes, valve areas and pressure gradients.

1.3 On the use of volumetric data

Much of the recent advancement in valvular heart disease evaluation and treatment can be attributed to the advent of noninvasive cardiac imaging modalities, such as echocardiography, CMR and CT, which are now being used extensively for diagnostics and risk evaluation[33]. Volumetric acquisition enables the visualization of cardiac districts from virtually any perspective, better appreciating patient-specific anatomical complexity, as well as an accurate quantitative functional evaluation of chamber volumes and mass avoiding geometric assumptions[34]. The accuracy and reproducibility of a two-dimensional (2D) imaging modality is generally suboptimal. A comprehensive two-dimensional (2D) echocardiographic examination still requires numerous probe manipulations; alternatively, 3D windows include both area and depth (i.e., volumetric imaging) within the imaging plane, requiring less probe manipulation thus decreasing operator-dependent artifacts [10].

Furthermore, when using 2D acquisition a parallel alignment of the plane to the orifice is sometimes impossible to get in short-axis view but, even more, “monoplanar display” view is insufficient when exploring structures characterized by a markedly non-planar morphology, such as the mitral and tricuspid valves[11,32,35–38]. For instance, 2D echocardiography is not able to provide data about mitral annular shape as well as MV prolapse diagnosis should not be made basing on 2D four-chamber classic view only since it might be not efficient in prolapse localization and quantification[10].

Considering the dynamically changing configuration of the cardiac structures within the cardiac cycle, one should be aware of the relevance of introducing fourth-dimension information, namely the time[39]. Dynamic 3D imaging, such as real-time 3D echocardiography and 4D CT, can be crucial in the assessment of the spatial and functional relationship with surrounding tissues, such as the LV outflow tract and mitral annulus or the AV complex itself[29,40]. These features can be beneficial in applications requiring real-time imaging and response, such as 3D image-guided cardiac procedures[41].

In addition, volumetric data can be used to obtain 3D patient-specific computational models of the cardiac valves, which can be exploited both for the morphological and the biomechanical analysis. The former is mainly accomplished by post-processing the clinical volumetric data and it allows for the quantitative description of the valvular geometry in the diagnostic and prognostic process[42]. The latter is performed to study the stress-strain behavior of the valvular structure in physiological and pathological conditions[43] and to predict and compare the effects of different surgical procedure on the same valvular structure[44].

1.3.1 Morphological analysis

Precise morphological and functional knowledge about the heart valves' apparatus is a prerequisite during the entire clinical workflow including diagnosis, therapy-planning, surgery, or percutaneous intervention, as well as patient monitoring and follow-up[45]. This scenario increasingly relies on non-invasive imaging modalities, such as cardiac CT and transesophageal echocardiography (TEE), which enable for dynamic 4-D scans of the beating heart over the whole cardiac cycle, encoding comprehensive structural and dynamic information. Although this extensive amount of information is barely exploited in the clinical practice due to its complexity, there has been growing interest in developing geometrical model, which can provide quantitative anatomical assessment by means of semi- or fully-automated images analysis[46,47].

1.3.2 Mitral Valve

Transesophageal echocardiography (TEE) is the commonly used technique for the evaluation of MV function. Indeed, 3D TEE datasets provide more complete and higher resolution comparing to 2D TEE and 3D TTE, respectively[48]. Several previous studies[30,42,39] have stressed the importance of the quantification of global annular dimensions and leaflet area for the accurate classification of the causes of MV disease and for the determination of the course of treatment in such cases. In particular, Maffessanti and colleagues[30], as well as Chandra et al[2], demonstrated that a volumetric analysis can be crucial when assessing the effects induced by a prolapse on MV anatomy (e.g., in FED or BD scenarios) to accurately improve the specific surgical planning. Clinically, in such cases, the most common used parameters are planarity and eccentricity of MV annulus as well as tenting height and volume; however, it was shown that when a single plane-based evaluation is performed the measurements were inaccurate[49,50].

In the degenerative MV scenario, in particular concerning the Barlow's Disease, the leaflets thickness could even be considered clinically relevant as a prognostic parameter. Using 2D TEE 4-chamber classic view, thickness was computed in a single mid-point of each leaflet[4], demonstrating an increase in leaflet area as well as in their thickness in patient affected by dilated cardiomyopathy. Whereas Anwar et al.[51] proposed a new score which includes MV leaflets thickness quantified from 2D cut-planes of RT 3D TEEE.

CMR has been exploited as a valid alternative in MV disorder investigation, especially when evaluating valve motion as well as valvular flow characteristics in regurgitant or stenotic diseases in patients with poor acoustic window[52,53]. Although echocardiography remains gold-standard, a fair number of studies have already proved cine-CMR as a valid imaging modality for assessment of significant regurgitation in patients with MV prolapse, pinpointing CMR-derived hallmarks associated to MV disease[37,54].

Finally, the growing interest in minimally invasive procedures is leading to increasing demand on accurate and reliable MV morphological assessment in the research field, in which CT might be more appropriate for geometric measurement in transcatheter intervention planning[33]. Pre-operative CT can provide structural details, such as calcification, as well as valvular thickening, being important in the geometrical complexity evaluation thanks to its superior spatial resolution[55]. Same conclusions have been previously yielded[56–58], confirming that 3D imaging, such as CT, could be pivotal in the MV complex morphological and dynamic quantification, aiding the decision-making process in transcatheter interventions scenario.

1.3.3 Tricuspid Valve

TV has been under-investigated for many years (referring to as "forgotten valve") since it was originally believed "to be designed to be incompetent"[59] and even because right heart abnormalities are usually asymptomatic[60]. However, recently the interest in the TV has been increasing, in part due to evidence that dysfunction of this valve may be more influential in patients' outcomes, to establish, for instance, if dilatation of the annulus is progressing to regurgitation and to appreciate that the annulus dimensions change during the cardiac cycle[17,61]. In this regard, even more than MV and AV, there is still much to learn about the TV complex as well as the natural changes occurring during ageing in order to better investigate and explain the alterations that may arise to its dynamic and highly mobile structure during disease, also exploiting the advent of multimodality imaging.

The primary imaging of choice for the TV morphological assessment is echocardiography. CT and MRI are also increasingly employed, providing additional information for pre-surgical planning to define complex anatomy, for intraprocedural monitoring or for post-surgical follow-up[38,52]. Mainly used in TTE modality, 3D imaging has been proved efficient in evaluating TV complex morphology[16] as well as locating the regurgitant orifice and measuring tenting volume and height in patients affected by tricuspid regurgitation (TR)[14,62]. With 3D TTE, Ton-Nu and co-workers[11] demonstrated that the typical non-planar configuration of the tricuspid annulus markedly changes in FTR, becoming flatter and increasing dimension mainly along the ventricle free-wall (antero-posterior direction). By means of TEE modality, Ring et al.[63] investigated much more in detail the anatomical and physiological alterations which affect TV in abnormal dilated right hearts. Providing also dynamic analysis of annular structures, they gained insight into the FTR-related dilation mechanism as a prognostic indicator, proving the decrease of septo-lateral motility as the main contributor of TV area change.

Nonetheless, TV investigation through 3D TTE is challenging because of its unfavorable retrosternal position and the high variability of its anatomy. TV can be optimally visualized from a single mid- esophageal four-chamber view using the zoom mode only in 11% of patients, largely because this valve is anteriorly located, and has thinner leaflets compared with the mitral valve[16]. Thus, although 3D TTE remaining pivotal in the intraoperative guidance of implantable devices[64] and a better and more advanced understanding of spatial relationships among TV components is required[65]. To this aim, thanks to its greater spatial resolution, CT scans offers complementary information, such as amount and type of annular tissue (e.g., presence of calcification) as well as relative position of TV annulus respect to the right coronary artery[66]. Indeed, the initial course of the right coronary artery is relatively distant from the annulus, there is a gradual shortening of the distance to the endocardial surface toward the inferior segment of the annulus to less than 3 mm[65]. This could have important implications for invasive intracardiac procedures whether it is to ablate accessory atrioventricular pathways for pre-excitation or to repair the tricuspid valve at the annular level.

Tethering of leaflets as a result of annular remodeling and flattening has been proved as key-hallmark in FTR, even when a TA dilation does not occur[67]. In this study, performing a CMR image-based analysis, the author found that in FTR patients with non-dilated TA the 3D non-planar shape of the annulus is maintained, whereas both the tenting height and the annular longitudinal displacement altered, potentially being considered as one of FTR triggering factors.

1.3.4 Aortic Valve

2D TTE is the standard technique AV stenosis or regurgitation evaluation. Whereas AV volumetric imaging is mainly used for TAVI planning and as a support during the procedure. Indeed, given the anatomical complexity of the aortic root district, combined with specific features of transcatheter prostheses, a comprehensive description of its morphology may be crucial in diagnosis, planning as well as during the intervention[68] . Thus, use of echocardiographic, multislice computed tomographic, and angiographic data may provide complementary information for determining the anatomical suitability, efficacy, and safety of the procedure[41].

In clinical practice, multidetector computed tomography is the 3D imaging technique of choice for TAVI surgical planning, meaning that it allows for aortic annular measurements and therefore for prosthesis sizing[69]. Nevertheless, in the last decade several studies aimed at proving 3D TEE imaging as a valuable alternative, since it can be essential mostly in the in intra-operative guidance[70–72], thus performing annular parameters quantification during intervention.

In this scenario, analysis of both CT and 3D TEE datasets are commonly accomplished either manually or automatically, however being focused on the aortic root sizing, without considering other morphological relationships. Recent effort in clinical image post-processing have been focused on improving efficiency for real-time use[45,73], proposing automated method base on deformable template geometries and shape variation models. Ionasec and colleagues[45] presented an automatic tool for the segmentation and landmarks detection of the aortic valve on CT imaging data, which provides quantification of several anatomical features, such as aortic root principal diameters (atrio-ventricular, sino-tubular, sinuses) as well as annular circumference and area. However, as a major limitation, aortic valve area (AVA) computation is carried out using AVA planimetry method, thus obtaining a 2D approximated measure, as even proposed in a recent study by Queiros et al.[74]. Nonetheless, since new echocardiography-based approach is growing, several studies were recently performed[69,75,76], mainly relying on automated software.

1.4 Biomechanical analysis

In the last two decades, finite elements method has been increasingly adopted for the numerical structural simulation of the cardiac valves[44,77,78]. This approach compute stresses and strains, assuming that the effect of the surrounding blood can be described through prescribed pressures. Three illustrative works that used the three different imaging modalities (CT, TEE and CMR) are here reported.

1.4.1 Mitral Valve

In order to help identifying more robust criteria to select and tune MV repair techniques in different clinically relevant scenarios, and to test novel concepts, different research groups have proposed computational models to simulate the post-operative MV function based on its baseline pre-operative conditions[79,77,80,78]. The current generation of these models exploits the detailed anatomical information yielded by medical imaging to provide patient- specific analyses, paving the way toward the development of virtual surgical-planning tools[81–85].

Sturla et al.[86] simulated the Mitraclip© implant and its effect on three MVs affected by posterior prolapse. The patient-specific MV models were derived by cine-cardiac magnetic resonance imaging. In all the analyzed cases, Mitraclip© implantation significantly improved systolic leaflets coaptation without inducing major alterations in systolic peak stresses.

Wang et al.[87] developed a MV patient-specific finite element (FE) model and exploit the resolution and image quality of MDCT to identify leaflets, the chordae tendinea, the insertion points and the papillary muscles. Dynamic closure of the MV was simulated. The MV systolic configuration yielded by the simulation was similar to the MV geometry reconstructed from MSCT images at middle systole frame.

Rim et al.[88] simulated the quadrangular resection and the annuloplasty procedure on a degenerative MV reconstructed from 3D echocardiographic data. Moreover, they simulated the MV closure in the pre- and post-operative conditions. The pre-resection MV demonstrated a substantial lack of leaflet coaptation and high peak of stress in the free margin of the prolapsing region. Following the virtual resection and ring annuloplasty, the severity of the posterior leaflet prolapse markedly decreased, stress peaks disappeared and complete leaflet coaptation was effectively restored.

1.4.2 Aortic Valve

As previously mentioned from a morphological evaluation standpoint, most of the numerical works related to the aortic root district are focused on the simulation of TAVI [89,90]. In these simulations, the model included the entire aortic root with the three cusps as well as the model of the calcifications, which can be described through either paradigmatic or patient-specific pattern[91].

Morganti et al. [90] performed a computational analysis, that take into account both the patient-specific structure of the native aortic valve from the 2D echocardiography and an accurate evaluation of calcifications through MSCT. They analyzed two patients and for both they computed the stress distributions, geometrical changes and risk of paravalvular leakage.

Sturla et al.[89] evaluated the effect of different calcifications patterns on stent deployment through balloon-expansion. Their analysis suggested a relation between the alteration of the stresses in the native anatomical components and prosthetic implant with the presence and distribution of relevant calcifications. This alteration is dependent on the patient-specific features of the calcific aortic stenosis and may be a relevant indicator of suboptimal TAVI results.

1.4.3 Tricuspid Valve

The only complete numerical model of the TV is the parametric finite element (FE) model developed by Stevanella et al. in 2010[92] which up to now represents the state of the art. Developing this model, no imaging acquisition was performed to define the valve geometry, which instead was constructed merging experimental measurements on porcine and human samples with data taken from literature[93]. Considering the increasing clinical interest in TV this study should be considered as a first step towards the long-term development of tools for TV biomechanical evaluation both in the physiological and pathological scenarios.

1.5 Motivation

In the western-countries, approximately 2% of the population is affected by valvular heart diseases[9]. The standard technique for the diagnosis of these patients is 2D echocardiography[28]. However, with this modality the 28% of the patients affected by these pathologies remains undiagnosed[9]. This percentage could be reduced using mainly the volumetric data to describe the 3D complex morphology of the cardiac valves. However, the information yielded by volumetric imaging data has not been yet standardized in clinics, most likely due limited availability of such technologies in the clinical routine, as well as due to limited operators experience and post-processing tools. For these reasons, volumetric imaging has not been yet fully exploited, and state-of-the-art analyses mainly consist in the navigation of the full 3D volume through 2D cut planes.

Recently, the use and the importance of volumetric imaging data has been growing dragged by the increase of transcatheter devices implants[94], which require patient selection, pre-procedural planning and procedure guidance, performed through the use of medical imaging, to overcome the lack of direct view and access to the cardiac structures during operation. In this evolving scenario, the use of the 3D imaging is mandatory and pivotal in the interventional cardiology field[95]. In particular, 3D imaging modalities (e.g., echocardiography, multidetector row computed tomography, or cardiac magnetic resonance imaging) can provide detailed information on the dimensions and spatial relationships of the cardiac structures that are crucial to choose the best suited treatment including device size and the procedural approach[95].

Commercial and custom software for the analysis of volumetric imaging data have been developed and studies demonstrating the accuracy and the potential of these tools have been conducted[11,42,69,96–99]. However, the navigation of such information is still mainly performed using 2D cut planes of the volume, thus overlooking the need for virtual reconstructions of 3D cardiac structures and the quantification of spatial-temporal relations between heart sub-structures.

Moreover, a further advancement the pre-surgical planning phase could be accomplished exploiting numerical tools to perform biomechanical simulations. These could be beneficial in computing the effects of surgical or percutaneous procedures, also comparing different implantation techniques or different devices.

In the recent year, numerous works based on finite element simulations (considered as the gold-standard) focused on computing the effects of surgical or percutaneous techniques on the mitral valve apparatus[100–104], reconstructing patient-specific 3D geometries and working conditions of the valve leaflets and sub-structures. However, these numerical simulations rarely include proper mechanical characterizations of pathological tissues, as well as they over-simplify the geometrical characteristics of the involved structures (e.g., leaflets thickness).

Moreover, the vast majority of the numerical tools developed so far still require a huge amount of computational expense and time-demand, being far from practical application in the clinical routine. Only few works proposed alternative approaches to the finite element analyses in the attempt of reducing computational demands, but none of them proved the accuracy of such methods vs. finite element analysis[105–107].

1.6 Aims and outline of the work

In the previously described scenario, the first aim of this work was the standardization of the analyses of volumetric imaging data by defining segmentation process of the cardiac valves which was always the same regardless of the imaging modality, and the development of valve-specific algorithms to automatically define the 3D geometry of the analyzed cardiac structure.

The second aim was the implementation of automated approaches for the quantification of clinically-relevant variables and diagnostic markers. In specific, the aims were the computation of aortic valve area considering the entire 3D geometry, the quantification of the spatial relationship between the tricuspid valve and the right coronary artery and the definition of the thickness pattern and mechanical behavior of the myxomatous leaflet tissue.

Finally, the last aim was the advancement of the biomechanical simulation regarding the mitral valve, following a twofold approach: on the one hand, by improving the realism of the models adopted for the biomechanical characterization of valve tissues, while, on the other hand, by decreasing the computational demand of numerical simulations by implementing ad-hoc mass-spring models.

1.7 Thesis Outline

- Chapter 2

This Chapter describes the development of three new methods for the analysis of the anatomical area of the aortic valve to improve the diagnosis of patients affected by aortic valve stenosis. Ad-hoc algorithms were developed to compute the full 3D model of the valve leaflets and sub-structures, as well as of the valves calcification patterns using the 4D Multi Detector Computed Tomography. Automated methods were also implemented to perform a morphological characterization of the valve.

- Chapter 3

  This Chapter describes the morphological and dynamic analysis of the tricuspid valve in patients with severe functional tricuspid regurgitation using the 4D Multi Detector Computed Tomography. The distance between the tricuspid valve annulus and the right coronary artery was qualitatively and quantitatively assessed to improve the pre-procedural planning of tricuspid valve transcatheter therapies.

- Chapter 4

  This Chapter describes the development of a novel mass spring model approach used to simulate the closing phase of the mitral valve apparatus exploiting data yielded by cardiac magnetic resonance. The reliability of the mass spring model was tested by comparing the systolic peak configurations vs. those obtained through gold-standard finite element analyses and vs. ground truth data yielded by magnetic resonance imaging data.

- Chapter 5

  This Chapter describes the development of novel methods for the quantification of mitral valve leaflet regional thickness by means of 3D echocardiography, and the mechanical characterization of the leaflet tissue in presence of myxomatous disorders. This data were then exploited within finite element simulations to perform computations of mitral valve closure during systole, evaluating the effects of this patient-specific and pathology-specific data on the valve closed configuration and biomechanics.

- Chapter 6

  This Chapter provides a general discussion and the conclusive remarks of the PhD dissertation.

The works described in this thesis were realized in collaboration with different clinical and technical centers. In specific, the entire PhD project was developed under the technical supervision of prof. Emiliano Votta and prof. Alberto Redaelli at the Biomechanics Group of Politecnico di Milano (Department of Electronics, Information and Bioengineering). The studies described in chapters 3 and 4 were carried out in collaboration with the Heart Long Centrum of the Leiden University Medical Center (Leiden, Netherlands), while Chapter 2 raised from the collaboration with the Department of Cardiovascular Medicine in Mayo Clinic (Rochester, Minnesota).

1.8 Bibliography

1. Levine, R. A. *et al.* Three-dimensional echocardiographic reconstruction of the mitral valve, with implications for the diagnosis of mitral valve prolapse. *Circulation* **80,** 589–98 (1989).
2. Lang, R. M., Tsang, W., Weinert, L., Mor-Avi, V. & Chandra, S. Valvular Heart Disease: The Value of 3-Dimensional Echocardiography. *J. Am. Coll. Cardiol.* **58,** 1933–1944 (2011).
3. Salgo, I. S. *et al.* Effect of annular shape on leaflet curvature in reducing mitral leaflet stress. *Circulation* **106,** 711–7 (2002).
4. Chaput, M. *et al.* Mitral Leaflet Adaptation to Ventricular Remodeling: Occurrence and Adequacy in Patients With Functional Mitral Regurgitation. *Circulation* **118,** 845–852 (2008).
5. Muresian, H. The clinical anatomy of the mitral valve. *Clin. Anat.* **22,** 85–98 (2009).
6. Lam, J. H., Ranganathan, N., Wigle, E. D. & Silver, M. D. Morphology of the human mitral valve. I. Chordae tendineae: a new classification. *Circulation* **41,** 449–458 (1970).
7. Freed, L. A. *et al.* Prevalence and Clinical Outcome of Mitral-Valve Prolapse. *N. Engl. J. Med.* **341,** 1–7 (1999).
8. Adams, D. H., Rosenhek, R. & Falk, V. Degenerative mitral valve regurgitation: best practice revolution. *Eur. Heart J.* **31,** 1958–1966 (2010).
9. Nkomo, V. T. *et al.* Burden of valvular heart diseases: a population-based study. *Lancet* **368,** 1005–1011 (2006).
10. Lang, R. M. *et al.* EAE/ASE Recommendations for Image Acquisition and Display Using Three-Dimensional Echocardiography. *J. Am. Soc. Echocardiogr.* **25,** 3–46 (2012).
11. Ton-Nu, T.-T. *et al.* Geometric Determinants of Functional Tricuspid Regurgitation: Insights From 3-Dimensional Echocardiography. *Circulation* **114,** 143–149 (2006).
12. Fawzy, H. *et al.* Complete mapping of the tricuspid valve apparatus using three-dimensional sonomicrometry. *J. Thorac. Cardiovasc. Surg.* **141,** 1037–1043 (2011).
13. KWAN, J. *et al.* 3D geometry of a normal tricuspid annulus during systole: A comparison study with the mitral annulus using real-time 3D echocardiography. *Eur. J. Echocardiogr.* **8,** 375–383 (2007).
14. Fukuda, S. *et al.* Three-dimensional geometry of the tricuspid annulus in healthy subjects and in patients with functional tricuspid regurgitation: a real-time, 3-dimensional echocardiographic study. *Circulation* **114,** I492-8 (2006).
15. Miglioranza, M. H. *et al.* Dynamic Changes in Tricuspid Annular Diameter Measurement in Relation to the Echocardiographic View and Timing during the Cardiac Cycle. *J. Am. Soc. Echocardiogr.* **28,** 226–235 (2015).
16. Muraru, D., Badano, L. P., Sarais, C., Soldà, E. & Iliceto, S. Evaluation of Tricuspid Valve Morphology and Function by Transthoracic Three-Dimensional Echocardiography. *Curr. Cardiol. Rep.* **13,** 242–249 (2011).
17. Rogers, J. H. & Bolling, S. F. The Tricuspid Valve: Current Perspective and Evolving Management of Tricuspid Regurgitation. *Circulation* **119,** 2718–2725 (2009).
18. Taramasso, M. *et al.* The Growing Clinical Importance of Secondary Tricuspid Regurgitation. *J. Am. Coll. Cardiol.* **59,** 703–710 (2012).
19. Yacoub, M. H. & Cohn, L. H. Novel approaches to cardiac valve repair: from structure to function: Part II. *Circulation* **109,** 1064–72 (2004).

20. Misfeld, M. & Sievers, H.-H. Heart valve macro- and microstructure. *Philos. Trans. R. Soc. B Biol. Sci.* **362,** 1421–1436 (2007).
21. Anwar, A. M. *et al.* Assessment of normal tricuspid valve anatomy in adults by real-time three-dimensional echocardiography. *Int. J. Cardiovasc. Imaging* **23,** 717–24 (2007).
22. Aktas, E. O., Govsa, F., Kocak, A., Boydak, B. & Yavuz, I. C. Variations in the papillary muscles of normal tricuspid valve and their clinical relevance in medicolegal autopsies. *Saudi Med. J.* **25,** 1176–85 (2004).
23. Piazza, N. *et al.* Anatomy of the Aortic Valvar Complex and Its Implications for Transcatheter Implantation of the Aortic Valve. *Circ. Cardiovasc. Interv.* **1,** 74–81 (2008).
24. Anderson, R. H. Clinical anatomy of the aortic root. *Heart* **84,** 670–3 (2000).
25. Lansac, E. *et al.* A four-dimensional study of the aortic root dynamics. *Eur. J. Cardiothorac. Surg.* **22,** 497–503 (2002).
26. Chandra, S., Sugeng, L. & Lang, R. M. Three-dimensional Echocardiography of the Mitral Valve Leaflet Anatomy and Repair. *Curr. Cardiovasc. Imaging Rep.* **3,** 268–275 (2010).
27. Kochav, J., Simprini, L. & Weinsaft, J. W. Imaging of the Right Heart-CT and CMR. *Echocardiography* **32,** S53–S68 (2015).
28. Baumgartner, H. *et al.* 2017 ESC/EACTS Guidelines for the management of valvular heart disease. *Eur. Heart J.* **38,** 2739–2791 (2017).
29. Muraru, D., Badano, L. P., Vannan, M. & Iliceto, S. Assessment of aortic valve complex by three-dimensional echocardiography: a framework for its effective application in clinical practice. *Eur. Hear. J. - Cardiovasc. Imaging* **13,** 541–555 (2012).
30. Maffessanti, F. *et al.* Quantitative analysis of mitral valve apparatus in mitral valve prolapse before and after annuloplasty: A three-dimensional intraoperative transesophageal study. *J. Am. Soc. Echocardiogr.* **24,** 405–413 (2011).
31. Bohs, L. N. & Trahey, G. E. A novel method for angle independent ultrasonic imaging of blood flow and tissue motion. *IEEE Trans. Biomed. Eng.* **38,** 280–6 (1991).
32. Maffessanti, F. *et al.* Three-dimensional dynamic assessment of tricuspid and mitral annuli using cardiovascular magnetic resonance. *Eur. Heart J. Cardiovasc. Imaging* **14,** 986–95 (2013).
33. Sun, W., Martin, C. & Pham, T. Computational modeling of cardiac valve function and intervention. *Annu. Rev. Biomed. Eng.* **16,** 53–76 (2014).
34. Hung, J. *et al.* 3D Echocardiography: A Review of the Current Status and Future Directions. *J. Am. Soc. Echocardiogr.* **20,** 213–233 (2007).
35. Badano, L. P., Muraru, D. & Enriquez-Sarano, M. Assessment of functional tricuspid regurgitation. *Eur. Heart J.* **34,** 1875–1885 (2013).
36. van Rosendael, P. J. *et al.* Tricuspid valve remodelling in functional tricuspid regurgitation: multidetector row computed tomography insights. *Eur. Hear. J. – Cardiovasc. Imaging* **17,** jev140 (2015).
37. Sturla, F. *et al.* Dynamic and quantitative evaluation of degenerative mitral valve disease: a dedicated framework based on cardiac magnetic resonance imaging. *J. Thorac. Dis.* **9,** S225–S238 (2017).
38. Saremi, F., Hassani, C., Millan-Nunez, V. & Sánchez-Quintana, D. Imaging Evaluation of Tricuspid Valve: Analysis of Morphology and Function With CT and MRI. *Am. J. Roentgenol.* **204,** W531–W542 (2015).

39. Caiani, E. G. *et al.* Quantification of mitral annulus dynamic morphology in patients with mitral valve prolapse undergoing repair and annuloplasty during a 6-month follow-up. *Eur. J. Echocardiogr.* **12,** 375–383 (2011).
40. Elattar, M. A. *et al.* Dynamics of the aortic annulus in 4D CT angiography for transcatheter aortic valve implantation patients. *PLoS One* **12,** e0184133 (2017).
41. Kasel, A. M. *et al.* Standardized Imaging for Aortic Annular Sizing. *JACC Cardiovasc. Imaging* **6,** 249–262 (2013).
42. Chandra, S. *et al.* A three-dimensional insight into the complexity of flow convergence in mitral regurgitation: adjunctive benefit of anatomic regurgitant orifice area. *AJP Hear. Circ. Physiol.* **301,** H1015–H1024 (2011).
43. Votta, E. *et al.* A novel approach to the quantification of aortic root in vivo structural mechanics. *Int. j. numer. method. biomed. eng.* **33,** e2849 (2017).
44. Tasca, G. *et al.* Aortic Root Biomechanics After Sleeve and David Sparing Techniques: A Finite Element Analysis. *Ann. Thorac. Surg.* **103,** 1451–1459 (2017).
45. Ionasec, R. I. *et al.* Patient-specific modeling and quantification of the aortic and mitral valves from 4-D cardiac CT and TEE. *IEEE Trans. Med. Imaging* **29,** 1636–1651 (2010).
46. Grbic, S. *et al.* Complete valvular heart apparatus model from 4D cardiac CT. *Med. Image Anal.* **16,** 1003–1014 (2012).
47. Noack, T. *et al.* Four-dimensional modelling of the mitral valve by real-time 3D transoesophageal echocardiography: proof of concept. *Interact. Cardiovasc. Thorac. Surg.* **20,** 200–208 (2015).
48. Pepi, M. *et al.* Head-to-head comparison of two- and three-dimensional transthoracic and transesophageal echocardiography in the localization of mitral valve prolapse. *J. Am. Coll. Cardiol.* **48,** 2524–30 (2006).
49. Watanabe, N. *et al.* Quantitation of mitral valve tenting in ischemic mitral regurgitation by transthoracic real-time three-dimensional echocardiography. *J. Am. Coll. Cardiol.* **45,** 763–769 (2005).
50. Ryan, L. P. *et al.* Mitral valve tenting index for assessment of subvalvular remodeling. *Ann. Thorac. Surg.* **84,** 1243–9 (2007).
51. Anwar, A. M. *et al.* Validation of a new score for the assessment of mitral stenosis using real-time three-dimensional echocardiography. *J. Am. Soc. Echocardiogr.* **23,** 13–22 (2010).
52. Cawley, P. J., Maki, J. H. & Otto, C. M. Cardiovascular Magnetic Resonance Imaging for Valvular Heart Disease: Technique and Validation. *Circulation* **119,** 468–478 (2009).
53. Gulsin, G. S., Singh, A. & McCann, G. P. Cardiovascular magnetic resonance in the evaluation of heart valve disease. *BMC Med. Imaging* **17,** 67 (2017).
54. Han, Y. *et al.* Cardiovascular Magnetic Resonance Characterization of Mitral Valve Prolapse. *JACC Cardiovasc. Imaging* **1,** 294–303 (2008).
55. Kim, J. H., Kim, E. Y., Jin, G. Y. & Choi, J. B. A Review of the Use of Cardiac Computed Tomography for Evaluating the Mitral Valve before and after Mitral Valve Repair. *Korean J. Radiol.* **18,** 773–785 (2017).
56. Shanks, M. *et al.* Mitral Valve Morphology Assessment: Three-Dimensional Transesophageal Echocardiography Versus Computed Tomography. *Ann. Thorac. Surg.* **90,** 1922–1929 (2010).
57. Kim, S. S. *et al.* Quantification of stenotic mitral valve area and diagnostic accuracy of mitral stenosis by dual-source computed tomography in patients with atrial

fibrillation: comparison with cardiovascular magnetic resonance and transthoracic echocardiography. *Int. J. Cardiovasc. Imaging* **31,** 103–114 (2015).

58. Thériault-Lauzier, P. *et al.* Quantitative multi-slice computed tomography assessment of the mitral valvular complex for transcatheter mitral valve interventions part 2: geometrical measurements in patients with functional mitral regurgitation. *EuroIntervention* **12,** e1021–e1030 (2016).
59. BOLT, W., HOLLMANN, W., KANN, J., VALENTIN, H. & VENRATH, H. [Behavior of pulmonary circulation time and pulmonary capillary pressure in congenital and acquired heart failures]. *Z. Kreislaufforsch.* **46,** 438–45 (1957).
60. Bruce, C. J. & Connolly, H. M. Right-Sided Valve Disease Deserves a Little More Respect. *Circulation* **119,** 2726–2734 (2009).
61. Luxford, J., Bassin, L. & D'Ambra, M. Echocardiography of the tricuspid valve: Acknowledgements. *Ann. Cardiothorac. Surg.* **6,** 223–239 (2017).
62. Min, S.-Y. *et al.* Geometric changes after tricuspid annuloplasty and predictors of residual tricuspid regurgitation: a real-time three-dimensional echocardiography study. *Eur. Heart J.* **31,** 2871–2880 (2010).
63. Ring, L. *et al.* Dynamics of the tricuspid valve annulus in normal and dilated right hearts: a three-dimensional transoesophageal echocardiography study. *Eur. Hear. J. - Cardiovasc. Imaging* **13,** 756–762 (2012).
64. Mediratta, A., Addetia, K. & Lang, R. M. Reply. *JACC Cardiovasc. Imaging* **7,** 1286–1287 (2014).
65. Rosendael, P. J. Van *et al.* Tricuspid valve remodelling in functional tricuspid regurgitation : multidetector row computed tomography insights. 96–105 (2016). doi:10.1093/ehjci/jev140
66. Ancona, F. *et al.* Multimodality imaging of the tricuspid valve with implication for percutaneous repair approaches. *Heart* **103,** 1073–1081 (2017).
67. Maeba, S., Taguchi, T., Midorikawa, H., Kanno, M. & Sueda, T. Four-dimensional geometric assessment of tricuspid annulus movement in early functional tricuspid regurgitation patients indicates decreased longitudinal flexibility. *Interact. Cardiovasc. Thorac. Surg.* **16,** 743–9 (2013).
68. Zamorano, J. L., Gonçalves, A. & Lang, R. Imaging to select and guide transcatheter aortic valve implantation. *Eur. Heart J.* **35,** 1578–87 (2014).
69. Prihadi, E. A. *et al.* Feasibility, Accuracy, and Reproducibility of Aortic Annular and Root Sizing for Transcatheter Aortic Valve Replacement Using Novel Automated Three-Dimensional Echocardiographic Software: Comparison with Multi–Detector Row Computed Tomography. *J. Am. Soc. Echocardiogr.* (2017). doi:10.1016/j.echo.2017.10.003
70. Vahanian, A. *et al.* Transcatheter valve implantation for patients with aortic stenosis: a position statement from the European association of cardio-thoracic surgery (EACTS) and the European Society of Cardiology (ESC), in collaboration with the European Association of Percutaneous Cardiovascular Interventions (EAPCI). *EuroIntervention* **4,** 193–9 (2008).
71. Jilaihawi, H. *et al.* Aortic Annular Sizing for Transcatheter Aortic Valve Replacement Using Cross-Sectional 3-Dimensional Transesophageal Echocardiography. *J. Am. Coll. Cardiol.* **61,** 908–916 (2013).
72. Vaquerizo, B. *et al.* Three-dimensional echocardiography vs. computed tomography for transcatheter aortic valve replacement sizing. *Eur. Hear. J. – Cardiovasc. Imaging* **17,** jev238 (2015).

73. Yefeng Zheng, Y. *et al.* Automatic Aorta Segmentation and Valve Landmark Detection in C-Arm CT for Transcatheter Aortic Valve Implantation. *IEEE Trans. Med. Imaging* **31,** 2307–2321 (2012).
74. Queirós, S. *et al.* Automatic 3D aortic annulus sizing by computed tomography in the planning of transcatheter aortic valve implantation. *J. Cardiovasc. Comput. Tomogr.* **11,** 25–32 (2017).
75. Mediratta, A. *et al.* 3D echocardiographic analysis of aortic annulus for transcatheter aortic valve replacement using novel aortic valve quantification software: Comparison with computed tomography. *Echocardiography* **34,** 690–699 (2017).
76. Calleja, A. *et al.* Automated Quantitative 3-Dimensional Modeling of the Aortic Valve and Root by 3-Dimensional Transesophageal Echocardiography in Normals, Aortic Regurgitation, and Aortic Stenosis: Comparison to Computed Tomography in Normals and Clinical Implications. *Circ. Cardiovasc. Imaging* **6,** 99–108 (2013).
77. Kunzelman, K. S., Reimink, M. S. & Cochran, R. P. Flexible versus rigid ring annuloplasty for mitral valve annular dilatation: a finite element model. *J. Heart Valve Dis.* **7,** 108–116 (1998).
78. Avanzini, A., Donzella, G. & Libretti, L. Functional and structural effects of percutaneous edge-to-edge double-orifice repair under cardiac cycle in comparison with suture repair. *Proc. Inst. Mech. Eng. H.* **225,** 959–971 (2011).
79. Votta, E. *et al.* The Geoform Disease-Specific Annuloplasty System: A Finite Element Study. *Ann. Thorac. Surg.* (2007). doi:10.1016/j.athoracsur.2007.03.040
80. Votta, E. *et al.* 3-D computational analysis of the stress distribution on the leaflets after edge-to-edge repair of mitral regurgitation. *J. Heart Valve Dis.* **11,** (2002).
81. Wong, V. M. *et al.* The effect of mitral annuloplasty shape in ischemic mitral regurgitation: A finite element simulation. *Ann. Thorac. Surg.* (2012). doi:10.1016/j.athoracsur.2011.08.080
82. Votta, E. *et al.* Toward patient-specific simulations of cardiac valves: State-of-the-art and future directions. *J. Biomech.* (2013). doi:10.1016/j.jbiomech.2012.10.026
83. Choi, A., Rim, Y., Mun, J. S. & Kim, H. A novel finite element-based patient-specific mitral valve repair: Virtual ring annuloplasty. in *Bio-Medical Materials and Engineering* (2014). doi:10.3233/BME-130816
84. Ge, L. *et al.* Measurement of mitral leaflet and annular geometry and stress after repair of posterior leaflet prolapse: Virtual repair using a patient-specific finite element simulation. *Ann. Thorac. Surg.* (2014). doi:10.1016/j.athoracsur.2013.12.036
85. Baillargeon, B. *et al.* Human Cardiac Function Simulator for the Optimal Design of a Novel Annuloplasty Ring with a Sub-valvular Element for Correction of Ischemic Mitral Regurgitation. *Cardiovasc. Eng. Technol.* (2015). doi:10.1007/s13239-015-0216-z
86. Sturla, F. *et al.* In vitro and in silico approaches to quantify the effects of the Mitraclip® system on mitral valve function. *J. Biomech.* **50,** 83–92 (2016).
87. Wang, Q. & Sun, W. Finite Element Modeling of Mitral Valve Dynamic Deformation Using Patient-Specific Multi-Slices Computed Tomography Scans. *Ann. Biomed. Eng.* **41,** 142–153 (2013).
88. Rim, Y., Choi, A., McPherson, D. D. & Kim, H. Personalized computational modeling of mitral valve prolapse: Virtual leaflet resection. *PLoS One* (2015). doi:10.1371/journal.pone.0130906
89. Sturla, F. *et al.* Impact of different aortic valve calcification patterns on the outcome of transcatheter aortic valve implantation: A finite element study. *J. Biomech.* **49,**

2520–30 (2016).
90. Morganti, S. *et al.* Prediction of patient-specific post-operative outcomes of TAVI procedure: The impact of the positioning strategy on valve performance. *J. Biomech.* **49,** 2513–2519 (2016).
91. Dimasi, A. *et al.* in 101–115 (Springer, Cham, 2015). doi:10.1007/978-3-319-10981-7_7
92. Stevanella, M., Votta, E., Lemma, M., Antona, C. & Redaelli, A. Finite element modelling of the tricuspid valve: A preliminary study. *Med. Eng. Phys.* **32,** 1213–1223 (2010).
93. Hiro, M. E. *et al.* Sonometric study of the normal tricuspid valve annulus in sheep. *J. Heart Valve Dis.* **13,** 452–60 (2004).
94. Grover, F. L. *et al.* 2016 Annual Report of The Society of Thoracic Surgeons/American College of Cardiology Transcatheter Valve Therapy Registry. *J. Am. Coll. Cardiol.* **69,** 1215–1230 (2017).
95. Delgado, V., van der Kley, F., Schalij, M. J. & Bax, J. J. Optimal imaging for planning and guiding interventions in structural heart disease: a multi-modality imaging approach. *Eur. Hear. J. Suppl.* **12,** E10–E23 (2010).
96. Veronesi, F. *et al.* A study of functional anatomy of aortic-mitral valve coupling using 3d matrix transesophageal echocardiography. *Circ. Cardiovasc. Imaging* **2,** 24–31 (2009).
97. Calleja, A. *et al.* Automated Quantitative 3-Dimensional Modeling of the Aortic Valve and Root by 3-Dimensional Transesophageal. 99–108 (2013). doi:10.1161/CIRCIMAGING.
98. Levack, M. M. *et al.* Three-dimensional echocardiographic analysis of mitral annular dynamics: Implication for annuloplasty selection. *Circulation* **126,** 7–8 (2012).
99. Clavel, M. A. *et al.* Dynamic phenotypes of degenerative myxomatous mitral valve disease: quantitative 3-dimensional echocardiographic study. *Circ. Cardiovasc. Imaging* **8,** (2015).
100. Choi, A., Rim, Y., Mun, J. S. & Kim, H. A novel finite element-based patient-specific mitral valve repair: Virtual ring annuloplasty. *Biomed. Mater. Eng.* **24,** 341–347 (2014).
101. Rim, Y., Choi, A., McPherson, D. D. & Kim, H. Personalized computational modeling of mitral valve prolapse: Virtual leaflet resection. *PLoS One* **10,** 1–15 (2015).
102. Sturla, F. *et al.* Biomechanical drawbacks of different techniques of mitral neochordal implantation: When an apparently optimal repair can fail. *J. Thorac. Cardiovasc. Surg.* **150,** 1303–1312 (2015).
103. Sturla, F. *et al.* In vitro and in silico approaches to quantify the effects of the Mitraclip system on mitral valve function. *J. Biomech.* (2016). doi:10.1016/j.jbiomech.2016.11.013
104. Siefert, A. W., Rabbah, J. P. M., Pierce, E. L., Kunzelman, K. S. & Yoganathan, A. P. Quantitative Evaluation of Annuloplasty on Mitral Valve Chordae Tendineae Forces to Supplement Surgical Planning Model Development. *Cardiovasc. Eng. Technol.* **5,** 35–43 (2014).
105. Mansi, T. *et al.* An integrated framework for finite-element modeling of mitral valve biomechanics from medical images: Application to MitralClip intervention planning. *Med. Image Anal.* **16,** 1330–1346 (2012).
106. Sprouse, C., Mukherjee, R. & Burlina, P. Mitral valve closure prediction with 3-d

personalized anatomical models and anisotropic hyperelastic tissue assumptions. *IEEE Trans. Biomed. Eng.* **60,** 3238–3247 (2013).

107. Hammer, P. E., Vasilyev, N. V., Perrin, D. P., Nido, P. J. del & Howe, R. D. Fast Image-based Model of Mitral Valve Closure for Surgical Planning. *MICCAI Work.* **6918,** 1–8 (2008).

Chapter 2

Assessment of the anatomical aortic valve area through the 3D morphological model

Pappalardo OA[1,2], Benfari G[3,4], Jenkins[4] W, Araoz[5] P, Redaelli A[2], Onorati F[1], Faggian G[1], Votta E[2], Enriquez-Sarano M[4]

[1] Division of Cardiovascular Surgery, Università degli Studi di Verona, Italy
[2] Department of Electronics, Information and Bioengineering, Politecnico di Milano, Italy
[3] Section of Cardiology, Department of Medicine, Università degli Studi di Verona, Italy
[4]Mayo Clinic, Department of Cardiovascular Diseases, Rochester, USA,
[5] Mayo Clinic, Radiology, Rochester, USA

Paper in preparation.

2.1 Introduction

Aortic stenosis (AS) is the most common primary valve disease in Europe and North America leading to surgery or trans-catheter intervention, with a growing prevalence due to the ageing population [1].

AS consists in the narrowing of the aortic valve (AV) lumen due to the inability of AV leaflets to open fully during ventricular systole, resulting in increased pressure drop across the valve [2]. This condition can be caused by increased leaflet stiffness, due to the presence of calcific deposits or scar tissue, or by anatomical alterations associated to congenital diseases [2].

Guidelines assert that echocardiography is the key tool for the diagnosis and evaluation of AS, and is the primary non-invasive imaging method for AS assessment [1]. One of the most important parameters to classify the severity of AS is the aortic valve area (AVA) that usually is measured using Doppler echocardiography [1].

Doppler-based AVA, i.e., effective AVA, is calculated through the continuity equation, assuming that blood flow is characterized by the same velocity space-distribution at inflow and outflow cross-section of the AV, i.e., at the annulus and at the free margin, respectively. Practically, effective AVA assessment depends on three measurements: i) the velocity time-integral measured by pulsed-wave Doppler in the left ventricular outflow tract (LVOT); ii) the velocity time-integral at the valve stenosis measured by continuous-wave Doppler; iii) the cross-sectional area of the LVOT, assumed circular and calculated from the diameter measured at the level of the aortic annulus on a 2D anatomical echo image.

Although effective AVA proved a valid score to classify AS, it can have sub-optimal accuracy due to the underlying assumptions and the errors intrinsically affecting the above-mentioned measurements [3]:

- as frequently observed through Doppler imaging, systolic LVOT flow can be not homogeneous and faster at the septal (anterior) side rather than at the posterior side, possibly causing velocity under- or over- estimations;
- velocity is underestimated when the Doppler echo beam is not orthogonal to the flow direction;
- velocity at the aortic annulus is measured by pulsed-wave Doppler not in the annulus region but more inside the left ventricle, which is typically narrower [3]. Hence, inconsistencies between velocity and cross-sectional area measurements can occur;

- 3D echography and multi- detector computed tomography (MDCT) studies showed that LVOT geometry frequently assumes an elliptical configuration rather than a circular one [4,5].

On this basis, direct measurement of the anatomical AVA has been indicated as a valid surrogate to circumvent the haemodynamic and geometric assumptions of the continuity equation for grading AS. In particular, the measurement of anatomical AVA on a 2D AV planimetry (planimetric AVA) proved crucial for diagnosis when the limitations of Doppler-based methods have a major impact, as in case of, e.g., small size aortas, left ventricle dysfunction, subaortic stenosis or increased LVOT gradients, eccentric jets and significant aortic regurgitation [6].

Several works [7–11] compared planimetric AVA vs. effective AVA and reported a good match between the two measurements. However, planimetric AVA is affected by errors caused by off-axis imaging of the non-planar 3D AV orifice. This effect is relevant especially when the orifice is distorted, as in bicuspid AV or in degenerative stenosis [6].

On this basis, we implemented an innovative and semi-automated method that i) generates the 3D model of the aortic valve and its calcifications, if any, and ii) computes the anatomical AVA based on MDCT images. We applied our method to a preliminary cohort of patients with severe AS and we compared our results vs. effective AVA measurements.

2.2 Study Population

Eighteen patients (clinical data) with severe AS were randomly selected from a wider population of patients, who were clinically indicated for 4D-MDCT, considered in a previous study [8]. For all these patients, informed consent was obtained according to institutional review board approval.

2.3 Multi Detector Computed Tomography data

Contrast enhanced electrocardiography-gated MDCT data acquired in [8] were retrospectively analyzed. These were acquired with a 64-detector scanner (Sensation 64, Siemens Medical Systems, Forchheim, Germany), without the routine use of b-blocker medications.

2.4 Data Analysis

Each MDCT sequence was reorganized as a 4D dataset consisting of volumetric datum, with a linear space resolution of 0.8±0.5 mm, over 20 frames in the R-R interval (Fig. 2.1.a).

Each 4D-MDCT dataset was initially navigated using the open-source software platform 3d Slicer [12]: the three-chamber plane was manually identified, and on this plane peak systole (PS) was identified as the frame characterized by maximal AV opening. In the PS frame, the axis passing through the center of the aorto-ventricular junction and aligned with the long axis of the aorto-ventricular junction was defined.

Through in-house custom software developed in Matlab® (The Mathworks, Inc., Natick, MA, US), 18 planes evenly rotated around the identified axis were automatically defined by interpolating the volumetric data (Fig. 2.1.b). In-plane resolution was set isotropic and equal to the minimum spatial resolution of the original volumetric data. On each plane, AV leaflet profile running from the annulus, i.e., the insertion of the aortic cusps into the sinuses, to the free margin was manually traced (Fig. 2.1.c). The software automatically implemented every subsequent processing step.

Generation of the AV 3D model - For each leaflet profile, traced points were interpolated by a cubic-spline, which was resampled at 32 uniformly distributed points. This process generated a cloud of 32x2x18 points (Fig. 2.1.d) inherently defining a grid organized in 32 curvilinear parallels – running circumferentially around the valve - and 36 curvilinear meridians – running from the annulus to the free margin - that represented the 3D model of the AV (Fig. 2.1.e,f). Through principal component analysis of the Cartesian coordinates of annular points, the best-fit plane (π_{ANN}) of the crown-shaped annulus was identified. The commissural points, defined as the points of the commissural regions most distant from π and positioned downstream of π_{ANN}, were automatically identified using k-mean clustering. Similarly, through principal component analysis of the Cartesian coordinates of the points on the AV free margin, the best-fit plane (π_{FM}) of the free margin was identified.

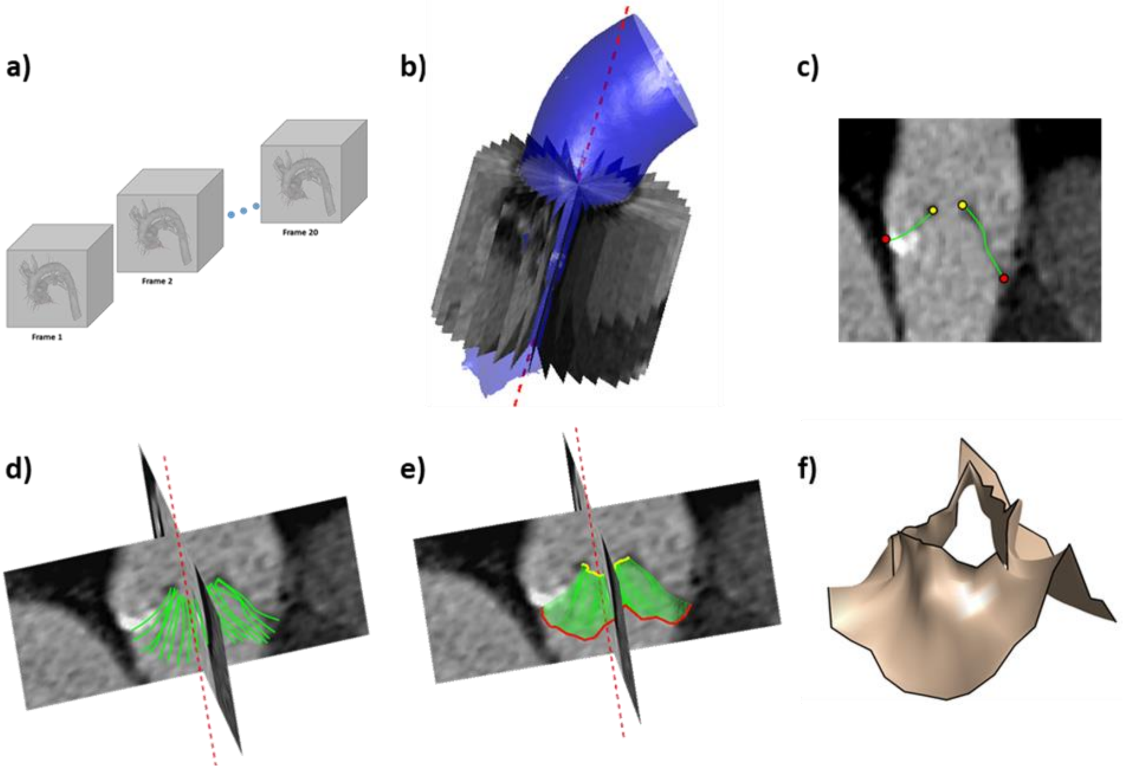

Figure 2.1 – a) Organization of the 20 frames of the 4D-MDCT data in an equal number of volumes. b) Ascending aorta (blue) with the long axis of the aortic valve (red dashed line) and the 18 segmentation planes. c) Radial plane in which the annulus (red points), the free margin (yellow points) and the cusp profile (green line) are segmented. d) 3D visualization of the segmented structures of the aortic valve. e) Lateral view of the mesh model of the aortic valve. f) Final anatomical model of the aortic valve.

Calcifications were reconstructed through two steps: first, the 3D dataset was navigated and a plane with evident calcifications was selected. On this plane, the isosurface defining the silhouette of the calcifications was set by tuning the corresponding isovalue (range 700-872 Hounsfiel Unit). Second, a marching cube algorithm was exploited to obtain the 3D geometry of all calcifications.

2.5 Anatomical AVA measurements

Anatomical AVA was calculated based on the 3D model based on three different definitions:

1) AVA_{SMALL}: smallest 2D anatomical orifice area of aortic cusps (Fig. 2.2.a). For each curvilinear meridian, the point closest to the rotation axis of the 18 image planes was selected. The Cartesian coordinates of the selected points were projected on the π_{ANN} plane; AVA was computed as the 2D surface area encompassed by the obtained projections.

2) $\mathrm{AVA}_{\mathrm{ANN}}$: surface area silhouetted by 2D projection of AV free margin on the π_{ANN} plane (Fig. 2.2.b).

3) $\mathrm{AVA}_{\mathrm{FM}}$: surface area silhouetted by 2D projection of the points of the AV free margin on π_{FM} (Fig. 2.2.c).

Double-blind comparison of these three measurements of anatomical AVA vs. effective AVA data obtained by transthoracic Doppler ultrasound imaging (effective AVA) was performed by an independent expert operator.

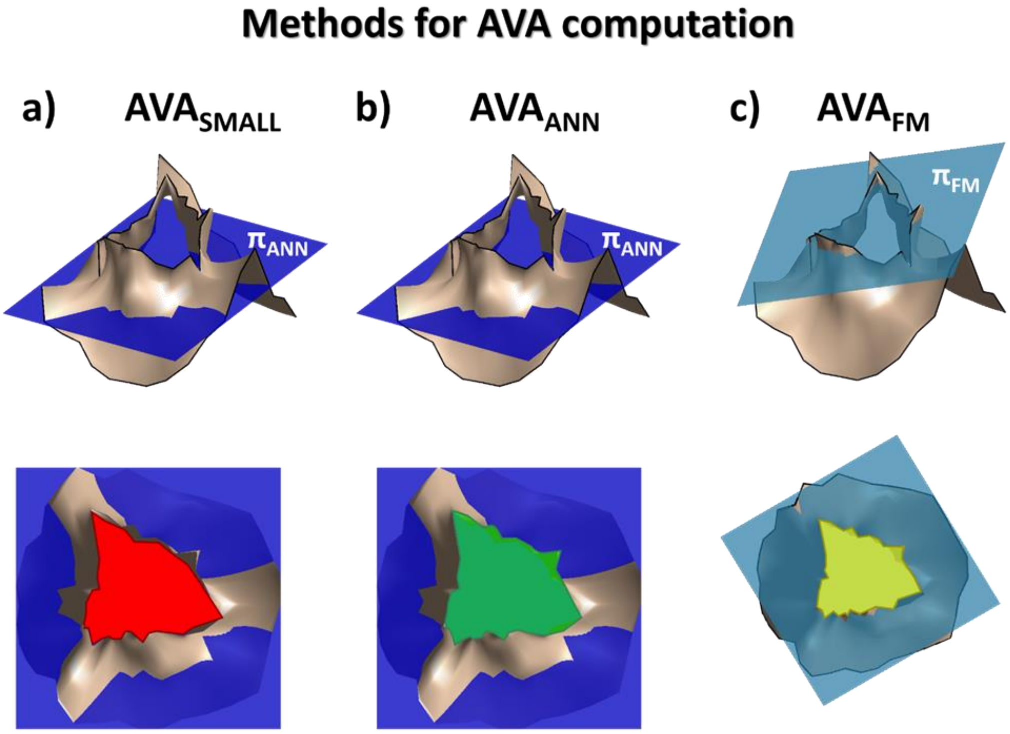

Figure 2.2 – (Top) The three automated methods used to calculate the aortic valve area: $\mathrm{AVA}_{\mathrm{SMALL}}$ (red area), $\mathrm{AVA}_{\mathrm{ANN}}$ (green area) and $\mathrm{AVA}_{\mathrm{FM}}$ (light blue). (Bottom) The annular plane (π_{ANN}), used to project the free margin when computing $\mathrm{AVA}_{\mathrm{SMALL}}$ and $\mathrm{AVA}_{\mathrm{ANN}}$, and the free margin plane (π_{FM}), used to project the free margin when computing $\mathrm{AVA}_{\mathrm{FM}}$, are depicted.

2.6 Sensitivity analysis

In order to search for a trade-off between the time-expense of AV manual tracing and the accuracy of our novel method, two auxiliary 3D models were obtained for each considered AV, based on only nine rotational image planes (one plane every two) and only six planes (one plane every three), respectively. For each auxiliary model, anatomical AVA measurements were obtained and the sensitivity of results to the amount of information exploited in the 3D models was assessed.

2.7 Statistical analysis

Following D'Agostino and Pearson normality test, results were expressed as mean ± SD or percentage. Differences between AVA_{SMALL}, AVA_{ANN} and AVA_{FM} measurements vs. effective AVA were analyzed using 1-way repeated-measures analysis of variance followed by the Dunnet test. Correlation between each MDCT-based measurements and effective AVA was quantified through Bland-Altman representation (mean±standard deviation of differences) and linear regression analysis (Pearson coefficient and slope). The statistical analysis was repeated on data obtained when decreasing the number of segmented planes.

2.8 Results

2.8.1 Aortic Valve 3D Models

3D reconstruction and identification of the cusps were successful in all the analyzed cases, and required approximately 10 minutes for each patient. Calcifications were always present and typically located in the leaflet belly and did not involve the free margin region. However, the calcification patterns where highly variable over patients, ranging from multiple small deposits to wide and c-shaped deposits running from commissure to commissure. In all patients, the calcification pattern was consistent with the AV cusp configuration (Fig. 2.3).

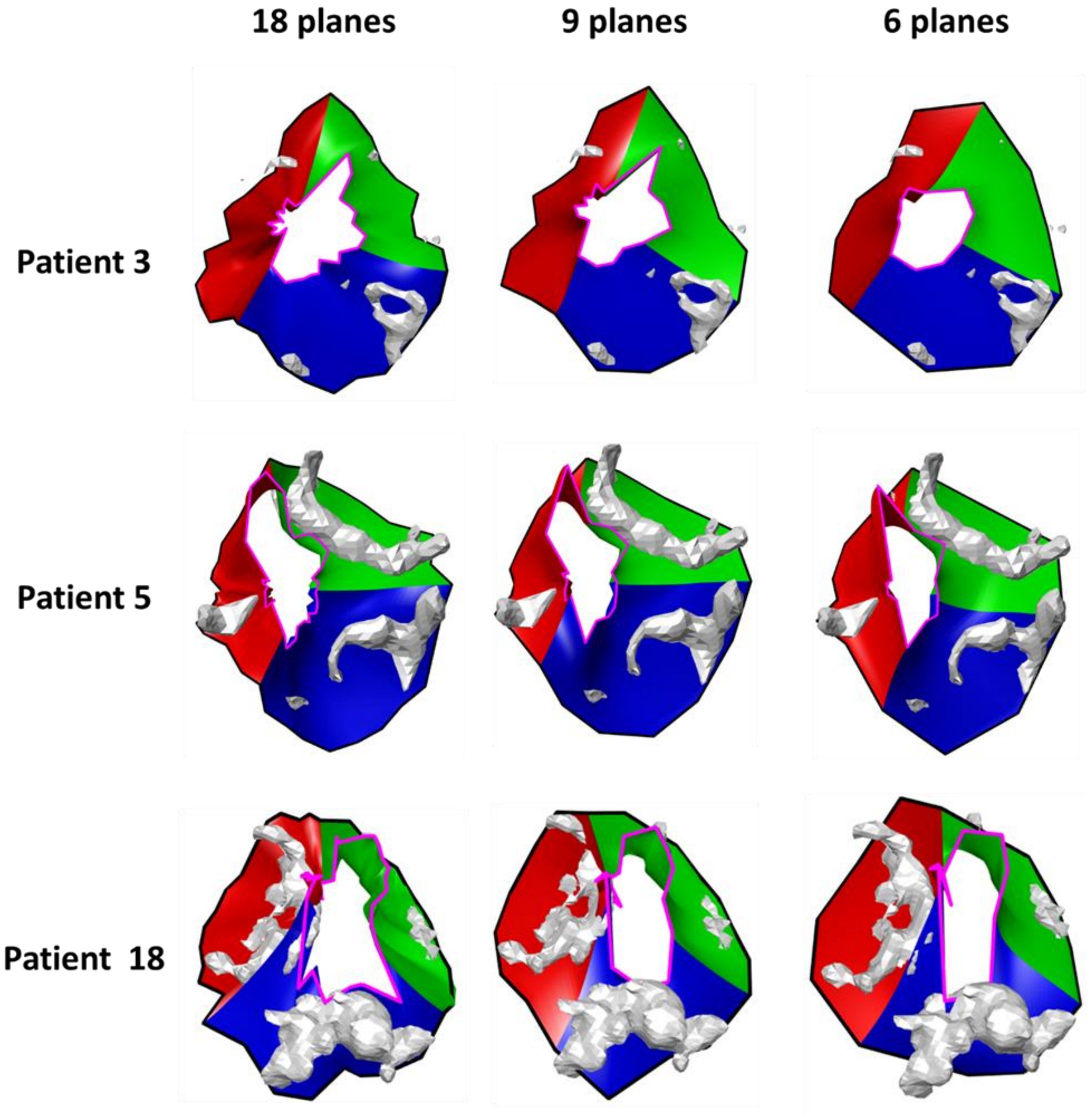

Figure 2.3 – 3D anatomical reconstructions of three AVs representative of different calcification levels. Blue=left coronary cusp; red=right coronary cusp; green=non-coronary cusp; grey=calcifications. For each AV, the result obtained when reducing the number of image planes (18, 9 and 6) is depicted.

When reducing the number of MDCT image-planes exploited in the reconstruction, these qualitative features were consistently reproduced. Yet, small but statistically significant reductions in 3D annulus circumference, 2D annulus area and leaflet surface area were obtained (Table 2.1).

Table 2.1 – Results of Bland Altman analysis (bias, standard deviation (SD) and coefficient of variation (CV)) of the three employed methods for the anatomical AVA computation with three degree of simplification (using the model generated using 18, 9 and 6 planes).

Quantitative Anatomical Measurements

	18 planes	**9 planes**	**6 planes**	**p value**
3D Annulus Circumference [mm]	120±10	106±9	100±7	<0.0001
2D Area Annulus [cm^2]	5.40±0.85	5.32±0.82	5.16±0.75	<0.0001
Total Area Cusps [cm^2]	9.17±1.56	7.97±1.30	7.52±1.24	<0.0001

AVA Quantification

	Bland Altmann Analysis				**Linear Regression**	
	Mean ± SD[mm^2]	**BIAS [mm^2]**	**SD [mm^2]**	**CV [%]**	**r[-]**	**Slope**
AVA$_{SMALL}$	80.05±16.83	-2.06	8.94	12.01	0.85	0.93
AVA$_{SMALL}$ (9 PLANES)	74.05±14.47	-8.06	9.62	13.68	0.79	
AVA$_{SMALL}$ (6 PLANES)	68.68±16.31	-13.43	10.77	16.51	0.77	
AVA$_{ANN}$	87.56±20.02	5.45	10.25	11.71	0.86	1.26
AVA$_{ANN}$ (9 PLANES)	81.15±17.35	-0.96	9.48	12.20	0.84	
AVA$_{ANN}$ (6 PLANES)	75.00±19.49	-7.11	11.47	16.44	0.81	
AVA$_{FM}$	93.22±21.44	11.11	10.09	10.25	0.90	1.13
AVA$_{FM}$ (9 PLANES)	88.13±20.40	6.02	10.99	12.29	0.85	
AVA$_{FM}$ (6 PLANES)	80.25±19.36	-1.86	8.88	12.86	0.89	

2.8.2 Anatomical AVA Measurements

Effective AVA was 82±15 mm^2. When segmenting 18 image planes, AVA$_{SMALL}$, AVA$_{ANN}$ and AVA$_{FM}$ were equal to 80±16, 88 ±20 and 93 ±21 mm^2, respectively. The Bland Altman analysis of the three measurements vs. effective AVA reported a bias (limits of agreement) of 2.1 (-15.7+19.9), 5.5 (-4.8+15.8) and 11.1 (-1.0+21.2) mm^2, respectively. Linear regression of the three measurements vs. effective AVA yielded regression slopes equal to 1.26, 1.13 and 0.93 for AVA$_{ANN}$, AVA$_{FM}$ and AVA$_{SMALL}$, respectively. The respective Pearson coefficients were 0.85, 0.86 and 0.90.

When decreasing the number of segmented planes to 9 and 6, AVA mean values over the study population decreased by approximately 6 and 12 mm^2, respectively, and AVA standard deviation decreased by approximately 2 and 1 mm^2 (Table 2.1). Consistently, the bias of the Bland Altman analysis decreased by approximately 6 and 12 mm^2, whereas the range defined by the limits of agreement increased only marginally in most cases and decreased slightly in two cases (AVA$_{\text{ANN}}$ with 9 planes and AVA$_{\text{FM}}$ with 6 planes) (Table 2.1). The Anova and the Dunnet post-test tests highlighted that reducing the number of segmented image planes induced statistically significant changes in AVA$_{\text{ANN}}$, AVA$_{\text{FM}}$ and AVA$_{\text{SMALL}}$, with the only exception of AVA$_{\text{FM}}$ obtained from 9 planes.

2.9 Novelty of the method

We proposed an innovative workflow to compute the anatomical AVA based on MDCT. To the best of our knowledge, this is the first work combining the reconstruction of the full 3D anatomy of the AV, including calcifications, with the computation of the anatomical AVA through a semi-automated approach. Of note, our workflow automatically quantifies AVA through three indexes: AVA$_{\text{SMALL}}$, AVA$_{\text{ANN}}$ and AVA$_{\text{FM}}$.

2.10 Comparison Anatomical vs. effective AVA

AVA$_{\text{SMALL}}$, AVA$_{\text{ANN}}$ and AVA$_{\text{FM}}$ compared differently vs. effective AVA: AVA$_{\text{SMALL}}$ tends to yield lower values, while AVA$_{\text{ANN}}$ and AVA$_{\text{FM}}$ tend to yield larger ones. This trend could be expected: AVA$_{\text{ANN}}$ is computed by projecting the free margin on the annular plane π_{ANN}; hence, it inherently provides a quantification similar to the planimetric AVA, which has been previously shown to be larger than effective AVA [8]. This effect is further emphasized when considering AVA$_{\text{FM}}$, because in this case the free margin is projected on π_{FM}, which best fits the real lumen of the valve. As a result, the corresponding area is equal or larger than the one obtained by projecting the free margin on any plane with a different space-orientation, including π_{ANN}. Conversely, AVA$_{\text{SMALL}}$ focuses on the smallest section of the AV, and by construction provides lower anatomical AVA values. In any case, Bland Altman analysis vs. effective AVA highlighted that the half-width of the limits of agreement was in the order of 0.2 cm^2 at worst; previous studies that compared planimetric AVA vs. effective AVA reported comparable [10] or larger [8,13] half-width values.

2.11 Accuracy vs. Time-expense trade-off

Reducing the number of segmented planes from 18 to 9 and 6 implies a simplification of the 3D AVA geometry, as confirmed by the associated underestimation of the 3D circumference and the 2D area of the annulus and of the surface area of the cusps. This trend is consistent over the three AVA measures. However, the underestimation of the measure does not implicate a worsening of the Bland-Altman analysis vs. the effective AVA. Indeed, the bias decreases in magnitude when considering a lower number of planes; in particular, the bias characterizing AVA_{ANN} and AVA_{FM} becomes negligible when the models are generated based on 9 image-planes and 6 image-planes, respectively. This trend is consistent with the fact that as the number of image-planes is reduced, information on the 3D details and asymmetries of the free margin and of the annulus is lost. As a result, the free margin profile is simplified, the space-orientation of planes π_{ANN} and π_{FM}, which are used to project that profile, becomes more approximates, and the computed AVA scores become more similar to the result of a 2D assessment. Analyzing the data of this preliminary test, the best trade-off between accuracy and segmentation time-expense was obtained when considering AVA_{FM} based on only 6 image-planes. Of note, AVA_{FM} would be the only score to be computed, then only the free margin points should be traced, thus further reducing the time-expense of segmentation.

2.12 Potential implications of the proposed approach

Our approach measures directly the anatomical AVA. As a result, it rules out the need for the simplifying assumptions needed to estimate the effective AVA based on Doppler-based velocity measurements. Also, the direct anatomical measurement is performed on a full 3D reconstruction of the AV anatomy. As a result, our AVA measurements inherently account for AV asymmetries or anatomical derangements, which would be difficult to correctly capture through either effective AVA of planimetric AVA. Such asymmetries or derangements would be highly relevant when analyzing, e.g., patients affected by bicuspid AV disease or by severe and non-uniformly distributed AV calcification. Furthermore, AVA measurements are obtained by projecting the profile of the annulus or of the free margin on cross-sectional planes, i.e., π_{ANN} and π_{FM}, that are automatically defined through a mathematical criterion of general validity. Hence, the method does not require any manual and user-dependent selection of 2D cutting planes, which is instead required when measuring planimetric AVA.

Moreover, the approach herein proposed automatically complements AVA quantification with the 3D visualization of AV anatomy and of the associated calcification pattern. Hence, not only it provides the end-user with data to support the diagnosis of AS, but also with an exhaustive morphological information to support the planning of surgical or percutaneous interventions. Of note, this extra information could not be obtained through any of the 2D analyses that are currently performed in clinics.

Finally, the three indexes yielded by our method, i.e., AVA_{SMALL}, AVA_{ANN} and AVA_{FM}, are not merely three different ways of measuring the anatomical AVA. Instead, if analyzed together they allow to synthetically describe AV geometry and to classify it according to the scheme proposed in Fig. 2.4. If $AVA_{ANN} \approx AVA_{FM}$, then the planes π_{ANN} and π_{FM} are almost parallel. As result, the AV can have one of two configurations: if $AVA_{SMALL} \approx AVA_{ANN}$ the smallest lumen is located at the free margin and the AV has the shape of a convergent (Fig. 2.4.a), whereas if AVA_{SMALL} is sensibly smaller than AVA_{ANN} than the smallest lumen is located somewhere between the free margin and the annulus, and the AV is configured as a convergent-divergent (Fig. 2.4.b). If AVA_{ANN} and AVA_{FM} are sensibly different, then the plane π_{FM} is tilted with respect to π_{ANN}, which implies an asymmetric configuration of the AV (Fig. 2.4.c). Also in this case, depending on the relationship between AVA_{SMALL} and AVA_{FM}, an asymmetric convergent or an asymmetric convergent-divergent are obtained. This classification is of potential relevance in that each of the three geometrical pattern is inherently related to fluid-dynamic features of the AV. In the first case, the main direction of the jet is central and the maximum velocity of the flow is obtained immediately downstream of the AV free margin. In the second case, the jet is central but the maximum velocity of the flow is obtained upstream from the free margin; furthermore a pressure recovery between the smallest section of the valve and the free margin occurs. In the third case, the jet is eccentric and skewed towards one side of the proximal ascending aorta. As a results, in this case Doppler ultrasound would underestimate the maximum velocity when the ultrasound beam would be aligned with the main axis of the annulus.

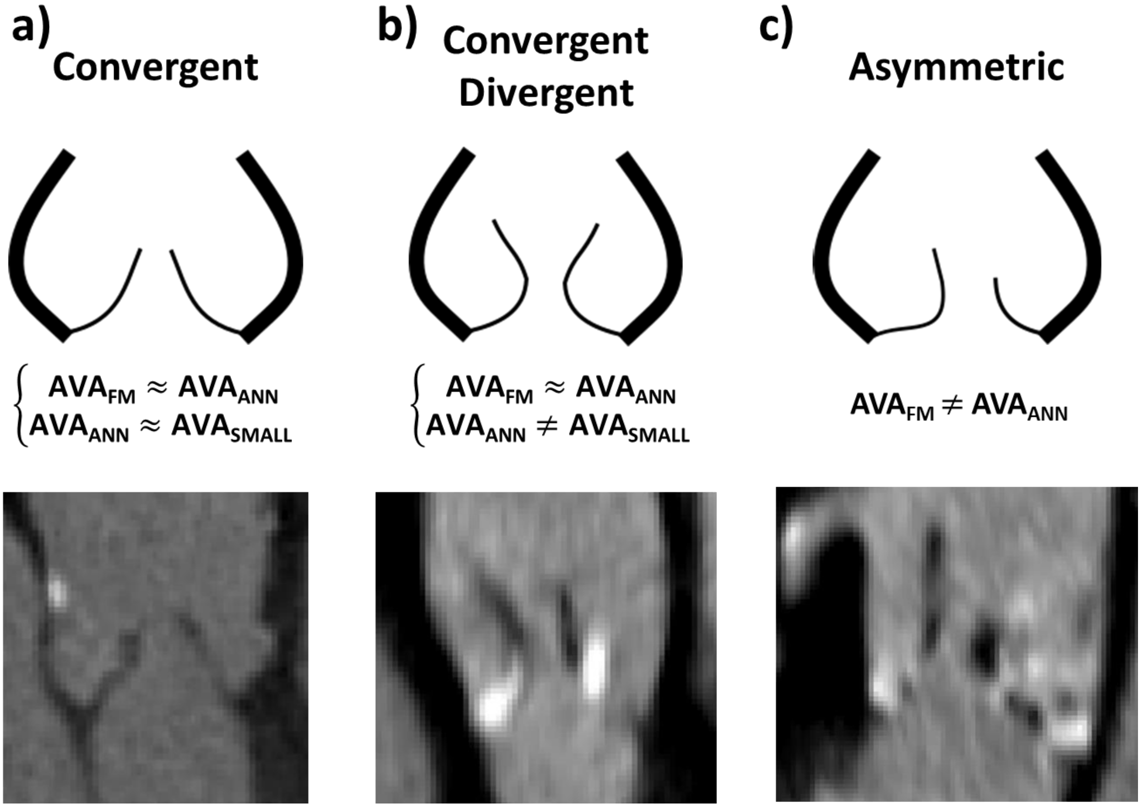

Figure 2.4 – Classification of AV systolic configuration based on the comparison of AVA_{SMALL}, AVA_{ANN} and AVA_{FM}. **a)** Symmetric convergent; **b)** Symmetric convergent-divergent; **c)** Asymmetric. For each class, a schematic 2D sketch (top), the relationship between the anatomical AVA scores (mid) and a representative image-plane (bottom) are depicted.

2.13 Future Developments

In this manuscript, the analysis was performed using MDCT data because the CT technique is the gold standard for the planimetric-AVA and for the evaluation of calcifications. The same workflow could be applied to volumetric datasets derived by 3D echocardiography; in that case, calcifications could not be assessed, but the reconstruction of the 3D AV geometry and the computation of the AVA scores would require no adaptation of the method.

Independently from the use of CT or 3D ultrasound images, the implantation of tracking algorithms based on, e.g., spackle tracking or cross-correlation can be envisioned to allow for the dynamic quantification of AV geometry and of anatomical AVA.

2.14 Limitations

The preliminary results of this analysis showed a good match with low variability between the results yielded by our new method and effective AVA measurements. At the same time, the analysis of our results suggests that our method could yield more exhaustive information, as compared to effective AVA and planimetric AVA computations, both in terms of AV configuration and trans-valvular hemodynamics. However, the study population consisted of only eighteen patients. For any reasonably sound conclusion to be drawn, a much larger study population should be considered. Importantly, in that case the diagnostic and prognostic power of our new methodology could be tested.

2.15 Bibliography

1. Baumgartner, H. *et al.* 2017 ESC/EACTS Guidelines for the management of valvular heart disease. *Eur. Heart J.* **38,** 2739–2791 (2017).
2. Baumgartner, H. *et al.* Recommendations on the echocardiographic assessment of aortic valve stenosis: a focused update from the European Association of Cardiovascular Imaging and the American Society of Echocardiography. *Eur. Hear. J. - Cardiovasc. Imaging* **18,** 254–275 (2016).
3. Flachskampf, F. A. Stenotic Aortic Valve Area. *JACC Cardiovasc. Imaging* **8,** 258–260 (2015).
4. Delgado, V. *et al.* Transcatheter aortic valve implantation: implications of multimodality imaging in patient selection, procedural guidance, and outcomes. *Heart* **98,** 743–754 (2012).
5. Messika-Zeitoun, D. *et al.* Multimodal Assessment of the Aortic Annulus Diameter. *J. Am. Coll. Cardiol.* **55,** 186–194 (2010).
6. Muraru, D., Badano, L. P., Vannan, M. & Iliceto, S. Assessment of aortic valve complex by three-dimensional echocardiography: a framework for its effective application in clinical practice. *Eur. Hear. J. - Cardiovasc. Imaging* **13,** 541–555 (2012).
7. Abdulla, J. *et al.* Evaluation of aortic valve stenosis by cardiac multislice computed tomography compared with echocardiography: a systematic review and meta-analysis. *J. Heart Valve Dis.* **18,** 634–43 (2017).
8. Clavel, M.-A. *et al.* Aortic Valve Area Calculation in Aortic Stenosis by CT and Doppler Echocardiography. *JACC Cardiovasc. Imaging* **8,** 248–257 (2015).
9. Larsen, L. H. *et al.* Aortic valve area assessed with 320-detector computed tomography: comparison with transthoracic echocardiography. *Int. J. Cardiovasc. Imaging* **30,** 165–173 (2014).
10. Alkadhi, H. *et al.* Aortic Stenosis: Comparative Evaluation of 16–Detector Row CT and Echocardiography. *Radiology* **240,** 47–55 (2006).
11. Shah, S., Jenkins, T., Markowitz, A., Gilkeson, R. & Rajiah, P. Multimodal imaging of the tricuspid valve: normal appearance and pathological entities. *Insights Imaging* **7,** 649–67 (2016).
12. Pieper, S., Lorensen, B., Schroeder, W. & Kikinis, R. The NA-MIC Kit: ITK, VTK,

pipelines, grids and 3D slicer as an open platform for the medical image computing community. in **2006,** 698–701 (2006).

13. Larsen, L. H. *et al.* Aortic valve area assessed with 320-detector computed tomography: comparison with transthoracic echocardiography. *Int. J. Cardiovasc. Imaging* **30,** 165–73 (2014).

Chapter 3

Assessment of tricuspid valve morphology and spatial relationship with the right coronary artery

Paper in preparation.

3.1 Introduction

Mild to severe tricuspid valve (TV) regurgitation affects 1.6 million patients in the United States (1). This pathology can be secondary to damage of TV structures (degenerative TV regurgitation) or to structural changes in the right heart (TV annular dilation associated to ventricular enlargement) that lead to improper TV leaflets coaptation, as in the case of functional tricuspid regurgitation (FTR). FTR is characterized by insufficient systolic TV coaptation even if in presence of anatomically normal leaflets and chordae (2). FTR results from the deformation of the right valvulo-ventricular complex and is frequently caused by left- heart disease or pulmonary hypertension (2–5). Of note, approximately 90% of all severe TV regurgitation is related to FTR(5,6). Treatment options for FTR are primarily surgical, but recent developments have shown that percutaneous procedures are an attractive alternative to open surgery, especially in high surgical risk patients (7). Recent emerging percutaneous transcatheter therapies for the TV may expand the treatment options beyond optimal medical therapy alone (8). Currently available transcatheter treatment options for FTR include TV bicuspidization using sutures, TV annulus cinching and reduction of annular length through a band (9,10).

Detailed knowledge of TV anatomy is fundamental to guide TV repair, especially prior to minimally invasive and percutaneous therapy (11,12). (13,14) An important factor in the planning of these procedures is the spatial relationship between the TV annulus and the right coronary artery (RCA), whose course and distance from the TV annulus are variable (15,16). Two-dimensional (2D) echocardiography is the imaging technique of first choice to evaluate FTR grade and TV annular dimensions (17). However, the accurate assessment of the three-dimensional (3D) and ellipsoidal configuration of the TV annulus may challenge 2D echocardiography (3) and require the superior capabilities of 3D echocardiography to gain insights into normal and abnormal TV anatomy (13,14). However, 3D echocardiographic may need highly trained and expert operators performing the examination, typically has a small field of view and may suffer from artifacts depending on the acoustic window.

By contrast, multidetector row computed tomography (MDCT) enables acquisition of 3D data of the heart and heart substructures with high spatial resolution and low noise. By that, MDCT may provide important insights into the geometrical changes of the TV in patients with FTR, but this potential has not been fully investigated in literature yet.

The purpose of the present study was to assess the geometrical changes of the TV during the cardiac cycle in patients with FTR by exploiting MDCT, focusing on the spatial relationship between the tricuspid annulus and the RCA.

3.2 Study population

Patients (n=11) with severe FTR, i.e., FTR grade > 3, and a control group (n=16) with no evidences of FTR were enrolled. The demographics of the two populations are detailed in Tab. 3.1.

Table 3.1 - Demographic data of the patients analyzed.

	Controls (n=11)	**FTR ≥3 (n=16)**	**p-value**
Age [years]	76.73 ± 9.37	79.50 ± 8.56	0.4336
Male [n, %]	[5, 45.5%]	[7, 43.8%]	
Body surface Area [m^2]	1.85 ± 0.17	1.86 ± 0.12	0.8517

3.3 Imaging acquisition

The cohorts of patients were analyzed through a 320-slice multi-detector CT scanner (AquilionOne, Toshiba Medical Systems, Tochigi-ken, Japan) with a collimation of 320±0.5mm and a rotation time of 350ms. Tube voltage and current were 100–135kV and 200–580mA, depending on the patient's body mass index. When indicated, oral ß-blockers were administered to patients with heart rates>65 beats per minute after careful evaluation of the patient's hemodynamic condition, taking aortic valve stenosis into consideration. Based on the patients' body weight, ionic contrast medium (Ultravist 370, Bayer, Whippany, NJ, USA) was infused in the antecubital vein in three phases: 60–80ml contrast with a flow-rate of 5.0–6.0ml/s, followed by a 20ml mixture of 1:1 contrast: saline and 25ml of saline. Initiation of scanning was synchronized to the arrival of the contrast medium in the left ventricle using automated peak enhancement detection with a threshold of +180 Hounsfield Units. A whole volume of 16cm coverage was used. Triggered to the electrocardiogram, the entire cardiac cycle was prospectively imaged. The CT data were reconstructed at each 10% of the RR interval.

3.4 Multi detector computed analysis

Each MDCT sequence was reorganized as a 4D dataset (4D-MDCT) consisting of volumetric datum, with an average in- plane resolution of 0.38 and a mean slice thickness of 1.6 mm, over 10 frames in the R-R interval.

The morphological analysis was performed at mid (MS) and late (LS) systole, as recommended for the geometric analysis of the TV with CT and echocardiography (8,18) and at mid (MD) and late (LD) diastole. These time points (MS, LS, MD, LD) correspond approximately to 20%, 40%, 70% and 90% of the R-R interval, respectively.

Each 4D-MDCT dataset was initially navigated using the open-source software platform 3d Slicer(19): the long-axis two- and four-chamber planes were manually identified, and these planes were used to identify the long axis of TV passing through the center of the valve.

Custom software was developed in Matlab® (The Mathworks, Inc., Natick, MA, US) for the analysis of the morphology and the dynamics of the TV through the cardiac cycle using 4D-MDCT.

In detail, 18 planes evenly rotated around the TV axis were automatically defined by interpolating the volumetric data. In-plane resolution was set isotropic and equal to the minimum spatial resolution of the original volumetric data. In all the analyzed frames, on each plane, the annulus was manually identified (Fig 3.1.b). At LS, the section of the coronary artery and the profile of the closed valve were defined (Fig 3.1.b). Finally, at each analyzed frame, a point $\mathbf{P}_{\mathbf{Ao}}$ was placed in the region of the TV annulus closest to the center of the aortic valve to define a consistent anatomical reference for all the analyzed datasets.

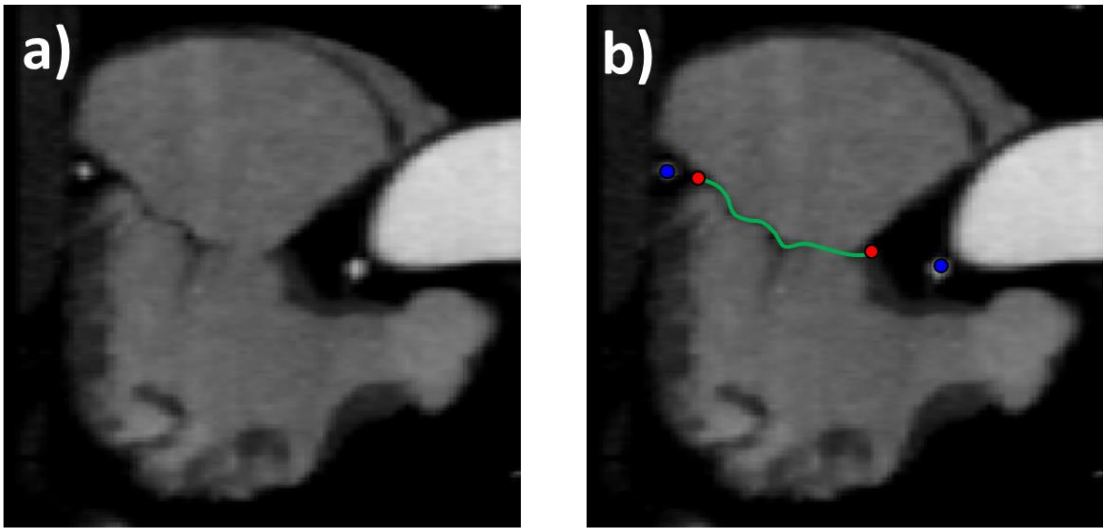

Figure 3.1 - a) One of 18 radial planes of the tricuspid valve**. b)** Segmentation of the tricuspid valve: annulus (red points), leaflets profile (green line), right coronary artery section (blue points)

Through principal component analysis of the Cartesian coordinates of annular points, the best-fit plane of the 36 raw points of the annulus was identified. The annulus points were fitted though 4th order Fourier functions to obtain a continuous 3D annular profile (20).

At the defined four cardiac phases (MS, LS, MD, LD), the following geometrical measurements of TV annulus dimensions were automatically computed (Fig. 3.2):

- Antero-posterior diameter (**D_{AP}**): the diameter along the antero-posterior direction, defined as the maximum diameter of the TV annulus
- Septo-lateral diameter (**D_{SL}**): the diameter along the septo-lateral direction, defined as the minimum diameter of the TV annulus
- Height of the annulus (**H_{Ann}**): defined as the maximal vertical distance between the highest and lowest annular points
- Eccentricity (**E**): computed as ratio between the septo-lateral and the antero-posterior diameter
- 3D perimeter of the annulus
- 2D Area defined as the portion of area delimited by the 2D projection of the annulus profile.

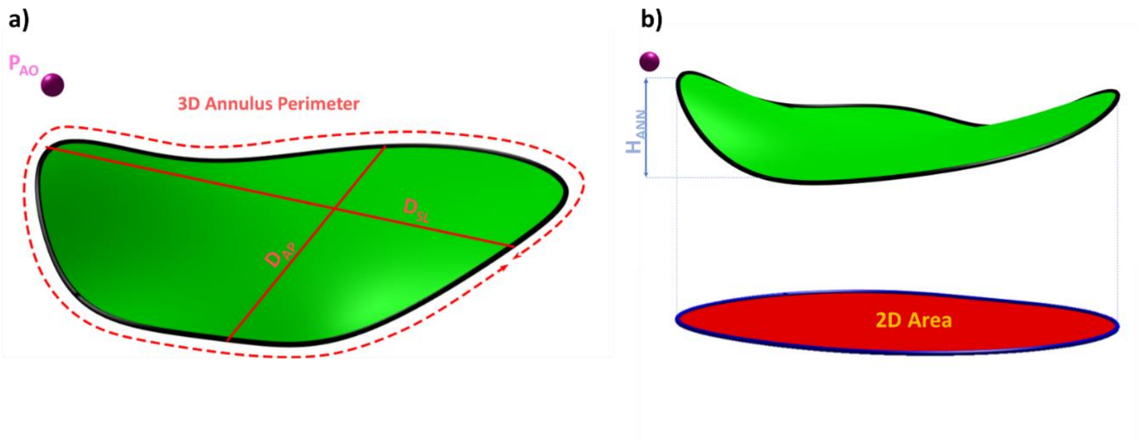

Figure 3.2 - Principal morphological measures of the tricuspid annulus and the aortic reference point (P_{AO}).

At LS, the 3D morphology of the RCA was defined by interpolating the raw coronary points through a 3D natural cubic spline curve (21). For each point of the resulting curve, the Euclidian distance to the TV annulus was computed and decomposed into its vertical and radial components.

At LS, the user-input points of the closed valve profile were interpolated by a 2D cubic spline, which was resampled at 64 uniformly distributed points. The cloud of points (18X64) representing the valve leaflets at late systole were fitted through a Loess function (22) that analytically defines the 3D model of the leaflets in this configuration.

The tenting volume was computed as the part of space limited by the leaflets surface and the annular plane.

3.5 Statistical data analysis

All the statistical computations were performed in GraphPad Prism 7 (GraphPad Software Inc., La Jolla, CA, USA). Continuous variables were expressed as mean ± standard deviation (SD) after Kolmogorov-Smirnov normality test. Changes in dynamics were assessed using 2-way ANOVA for repeated measures with one factor analyzed as a repeated-measure factor. Statistical significance was indicated by a probability value of $p<0.05$.

3.6 Results

3.6.1 Tricuspid valve morphological characterization

In FTR patients, annulus 3D Circumference (Fig. 3.3.a), 2D Area (Fig. 3.3.b), D_{Max} and D_{Min} (Fig. 3.3.c-f) were higher than in controls, irrespective of the time-point of the cardiac cycle, showing also a similar temporal trend. Notably, the minimum value for these variables was observed at LS. For all the above-mentioned variables, a statistically significant difference between controls and patients was observed (Table 4.2, Group analysis) and both populations reported significant dynamic changes over the cardiac cycle (Tab. 3.2 Phase analysis).

Differences in Eccentricity and annular height between controls and FTR patients were not statistically significant (Tab. 3.2 Group). For both populations, Eccentricity was approximately constant during the cardiac cycle with a mean value of 0.77±0.066 and 0.78±0.74 for controls and FTR patients respectively. Annular height in patients with severe

FTR was constant during the cardiac cycle while for controls the maximum (9.18±1.643 mm) was reached at MS and the minimum (6.38±2.53 mm) at MD.

The tenting volume computed at LS for controls (0.85±0.61) and FTR patients (3.36±2.74) was significantly different (p-value = 0.0064).

3.6.2 Tricuspid valve annulus – Right coronary artery geometrical relationship

Two representative cases (1 Control, 1 FTR) were randomly selected from the two populations to exemplify the path of the RCA, as reported in Fig. 3.4a-b. RCA path was color-coded according to the distance from the annulus: in particular, regions characterized by a Euclidian distance lower than 2mm are represented in red.

The minimum distance computed by the three methods for all the FTR patients was reported in Tab. 3.3; the mean values were 4.0mm, 3.8mm and 1.1mm for the Euclidean distance, its radial and vertical components, respectively. A statistically significant difference between the three metrics was observed, suggesting that these are not equivalent (p value < 0.0001).

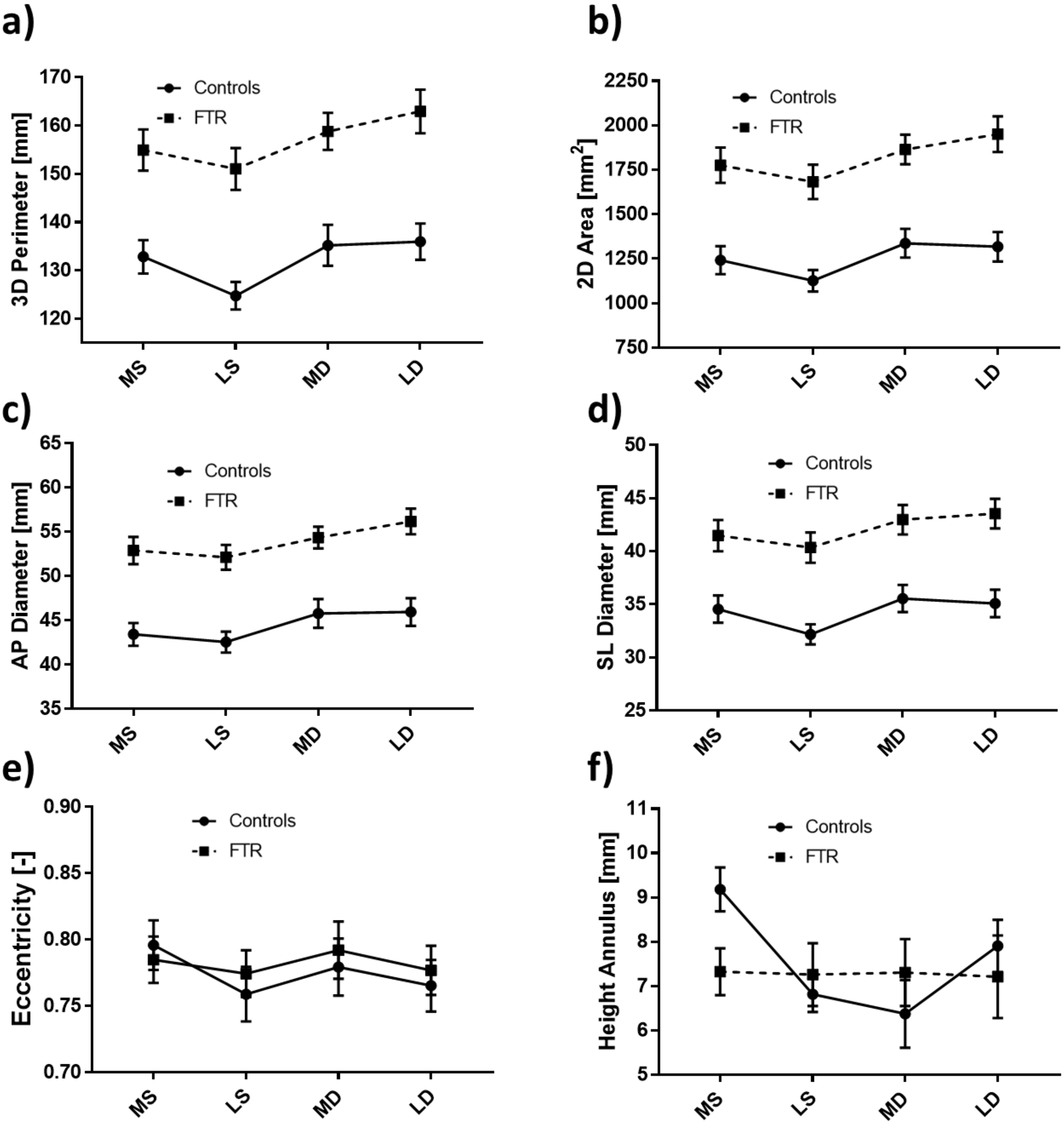

Figure 3.3 - Time-dependent TV geometric features for controls and FTR patients over the cardiac cycle: **a)** 3D circumference, **b)** 2D area, **c)** D_{AP}, **d)** D_{SL}, **e)** Eccentricity, **f)** Height Annulus. Data are expressed as mean ± SEM (standard error of the mean).

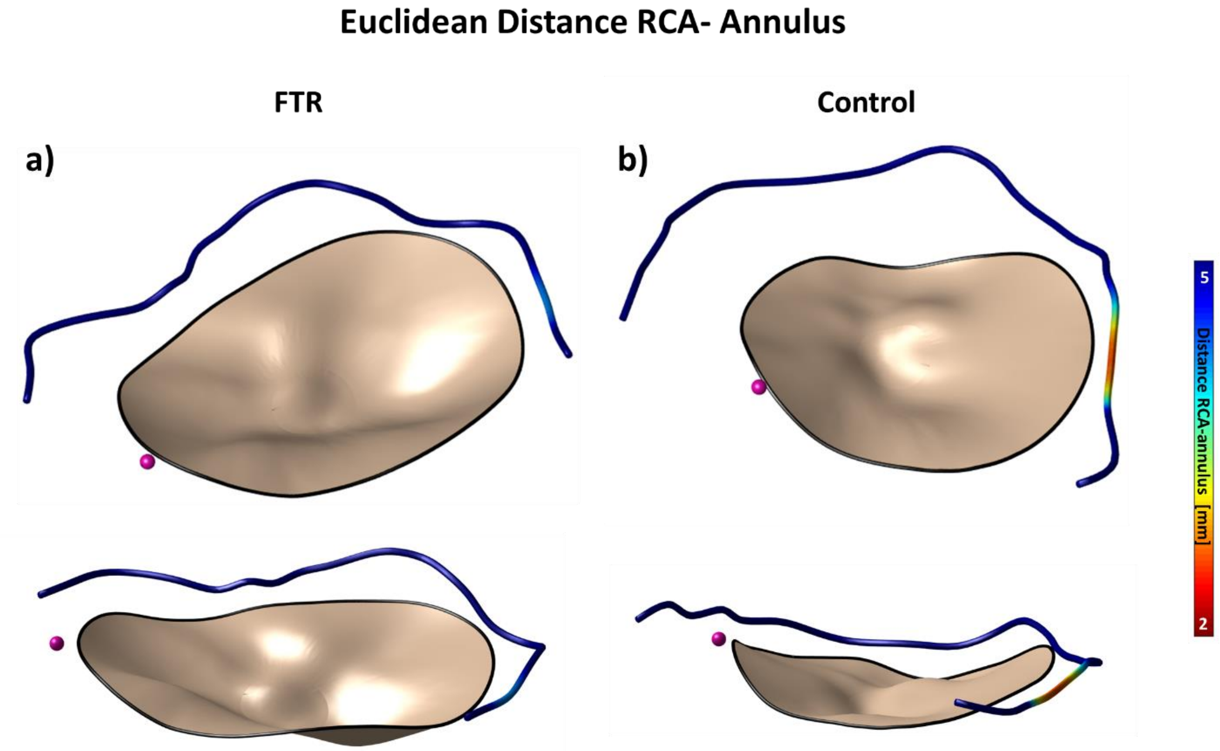

Figure 3.4 - 3D reconstruction of the right coronary artery for a FTR valve (a) and a control TV (b). For each of the two subjects, two different views are depicted. The rendering of the right coronary artery is color-coded based on the local Euclidean distance from the annulus from.

Table 3.2 - Parameters of dynamic TV anular measurements for Normal and FTR patients. Data are expressed as mean ± SD (standard deviation).

	Mid-systole	**Late-systole**	**Mid-Diastole**	**Late-Diastole**	**P-value Group**	**P-value Phase**	**P-value Group Phase Interaction**
2D Area [cm^2]							
Controls	12.42 ± 2.63	11.26 ± 2.02	13.37 ± 2.67	13.18 ± 2.75	0.0001	<0.0001	0.2949
FTR	17.76 ± 3.95	16.82 ± 3.89	18.65 ± 3.32	19.51 ± 3.99			
3D Perimeter [mm]							
Controls	132.85 ± 11.49	124.75251 ± 9.5	135.21 ± 14.01	135.96 ± 12.47	0.0002	<0.0001	0.2310
FTR	154.93 ± 17.09	151.03±17.40	158.82±15.28	165.95±17.99			
D_{AP} [mm]							
Controls	43.44 ± 4.27	42.55 ± 3.96	45.79 ± 5.37	45.95 ± 5.17	<0.0001	<0.0001	0.6442
FTR	52.90 ± 6.12	52.14 ± 5.62	54.36 ± 4.87	56.19 ± 5.83			
D_{SL} [mm]							

Controls	34.56 ± 4.23	32.19 ± 3.16	35.55 ± 4.25	35.09 ± 4.32	0.0004	<0.0001	0.4328
FTR	41.48±5.87	40.36 ± 5.73	42.98 ± 5.55	43.55 ± 5.58			
H [mm]							
Controls	9.18 ± 1.64	6.82 ± 1.32	6.38 ± 2.53	7.91 ± 1.96	0.6901	0.0792	0.0857
FTR	7.33 ± 2.10	7.26 ± 2.83	7.31 ± 3.01	7.21 ± 3.72			
E [-]							
Controls	0.80 ± 0.06	0.76 ± 0.07	0.78 ± 0.07	0.77 ± 0.06	0.7550	0.2501	0.7504
FTR	0.79 ± 0.07	0.77 ± 0.07	0.79 ± 0.09	0.78 ± 0.07			

Tab. 3.3 - Minimum distance between the right coronary artery and the tricuspid annulus computed though the three methods.

	Minimum Distance [mm]		
	Euclidean	**Radial**	**Vertical**
FTR 1	1.14	0.89	0.70
FTR 2	8.66	8.26	2.60
FTR 3	2.09	1.92	0.82
FTR 4	3.01	2.77	1.19
FTR 5	7.00	7.00	0.17
FTR 6	2.69	2.66	0.43
FTR 7	3.14	2.34	2.09
FTR 8	1.57	1.40	0.70
FTR 9	2.60	2.60	0.07
FTR 10	6.01	5.61	2.16
FTR 11	4.21	4.08	1.07
FTR 12	6.99	6.64	2.18
FTR 13	1.19	1.08	0.49
FTR 14	8.18	8.05	1.45
FTR 15	3.28	3.21	0.66
FTR 16	2.60	2.60	0.18

3.7 Novelty

In this work, we developed custom software to define the 3D morphology of the TV during the cardiac cycle and to automatically compute its geometrical characteristics. To the best of our knowledge, this is the first study of its kind in performing a qualitative and quantitative analysis of TV morphology in patients affected by severe FTR (≥3) starting from 4D MDCT, also quantifying the spatial relationship between TV annulus and the course of RCA at late systole.

3.8 Morphological analysis

The 3D geometrical model of the TV was successfully accomplished for all analyzed datasets (n=27), proving our methods to be robust and adaptable to different patient-specific geometries.

The use of 4D MDCT was also reliable in detecting group-specific characteristics, as well as differences between FTR patient and healthy controls, as suggested by the comparison of our data vs. data from the literature. Namely, in the FTR group we found similar patterns of annular perimeter (151.03±17.4 vs. 145.3±14.4 mm) and 2D area (1682.69±389.2 vs. 1539.7±260.2 mm^2), D_{AP} (52.14±5.62 vs. 49.0±4.5 mm) and D_{SL} (40.36±5.73 vs. 40.2±5.1 mm) as compared to a previous work that analyzed severe FTR patients based on MDCT (8). Consequently, also eccentricity was in the same range of variation (0.77±0.12 vs. 0.82±0.10). Also, considering the Controls group, the values of area (11.30±2.02 vs. 9.7±2.4cm2) and perimeter (124±9.47 vs. 113.9±14.3 mm) were similar at late systole to those obtained by (23), while at mid diastole, 2D area (13.37±2.68 vs. 10.7±2.2mm^2) and 3D perimeter (135.21±14.01 vs. 119.9±12.4 mm) were slightly higher.

The comparison performed between FTR patients and controls also confirmed that FTR induces annular dilation, as supported by the trend observed in perimeter, area, D_{AP} and D_{SL}, consistently with recent studies based on MDCT and echocardiography (18,23). Also, consistently with data reported by Ring et al. (24), the lowest value of TV annulus perimeter and area were observed at the late-systolic frame, while the anular height of FTR was characterized by almost constant values during the entire cardiac cycle. At mid systole, the average height of TV annulus was found higher for Controls than for FTR patients, as reported by (18). Finally, the values of tenting volume reported for the Controls (0.85±0.61) and FTR (3.36±2.74) were in agreement with the values reported by Muraru et al.(25,26).

3.9 Spatial relation between the tricuspid annulus and right coronary artery

Given the robustness and reliability in assessing the morphology of TV valve, we automatically quantified its geometrical relation with the RCA. These two cardiac structures are both characterized by a highly three-dimensional geometry and by inter-subject variability.

In addressing the need for understating their relative position, a previous study used volume rendered reconstructions to visualize the anatomy of the coronary arteries and of the endocardium (27). However, these 3D reconstructions were exploited only for qualitative analyses based on methods that do not allow for the precise definition of the TV annulus, nor, consequently, of the spatial relationship between the TV annulus and the in the 3D space. Such quantification was performed only on specific 2D cut-planes of the imaging volume, whose number and definition depended on the anatomy of the analyzed subject.

Instead, the method herein proposed provides for the first time i) a detailed 3D view of the TV structures (annulus and leaflets) in relation with the RCA course, ii) the possibility for the 3D navigation of the reconstructed models for an easy-to-understand qualitative analysis, rapidly identifying regions where the two structures are critically close, and iii) the quantitative assessment of the spatial relation between the two structures in the 3D space. This last feature is worth being stressed, in that it allows for the same semi-automated workflow on every subject, thus improving repeatability, and it allows for coping with possible perspective artifacts of a mere qualitative navigation that can mislead the analysis of 3D anatomical structures (28,29). Our data clearly show that the radial and vertical components do not provide the same information as compared to the corresponding 3D Euclidian distance; hence, limiting the analysis to a 2D component of the latter could be misleading.

Also, our results show that the distance between the RCA and the TV annulus varies notably over the course of the RCA, with a pattern that is subject-specific. This evidence strongly suggests that the entire course of RCA should be taken into consideration when analyzing its relationship with surrounding structures of TV. By exploiting the automatic computation of the Euclidean distance between TV annulus and RCA, the approach was standardized for all the analyzed datasets, yielding the actual distance between the two structures along the entire course of the RCA. Also, our method proved to be advantageous in avoiding the need for manually placing 2D planes to quantify TV-RCA distances.

Finally, we envision determinant scenarios in which the proposed methods and software tool may be viable, such as during the planning of the transcatheter techniques and devices that target the TV annulus and potentially can damage the RCA, e.g., Cardioband (Valtech

Cardio, Or Yehuda, Israel), Mitralign system (Mitralign Inc., Tewksbury,MA, USA) and TriCinch System (4Tech Cardio Ltd., Galway, Ireland).

The Mitralign system induces a bicuspidalization of the TV valve by positioning pledgeted sutures around the insertion points of the anterior and the posterior TV leaflets, improving their coaptation and reducing the TR grade.

For the Tricinch System the TV annulus dimensions are reduced by positioning of a corkscrew anchor at the anterior TV leaflet that is connected through a Dacron band to a self-expandable stent implanted in the inferior vena cava. In the Implantation of the Cardioband, a band is implanted using stainless steel and cinch to reduce the anular dimension.

In the MItaling and Cardioband implantation, for orientation and safety reasons a coronary wire is placed in the right coronary artery and monitored through fluoroscopy, which however can provide only a 2D projection of the cardiac structures.

The tool could be used to retrospectively analyze the clinical outcomes and the prognosis of the patients that undergo one of the previous procedures in order to define previously the critical case.

3.10 Bibliography

1. Taramasso M., Pozzoli A., Guidotti A., et al. Percutaneous tricuspid valve therapies: the new frontier. Eur Heart J 2017;38(9):639–47. Doi: 10.1093/eurheartj/ehv766.
2. Badano LP., Muraru D., Enriquez-Sarano M. Assessment of functional tricuspid regurgitation. Eur Heart J 2013;34(25):1875–85. Doi: 10.1093/eurheartj/ehs474.
3. Lancellotti P., Moura L., Pierard LA., et al. European association of echocardiography recommendations for the assessment of valvular regurgitation. Part 2: Mitral and tricuspid regurgitation (native valve disease). Eur J Echocardiogr 2010;11(4):307–32. Doi: 10.1093/ejechocard/jeq031.
4. Baumgartner H., Falk V., Bax JJ., et al. 2017 ESC/EACTS Guidelines for the management of valvular heart disease. Eur Heart J 2017;38(36):2739–91. Doi: 10.1093/eurheartj/ehx391.
5. Rogers JH., Bolling SF. The Tricuspid Valve: Current Perspective and Evolving Management of Tricuspid Regurgitation. Circulation 2009;119(20):2718–25. Doi: 10.1161/CIRCULATIONAHA.108.842773.
6. Nath J., Foster E., Heidenreich PA. Impact of tricuspid regurgitation on long-term survival. J Am Coll Cardiol 2004;43(3):405–9. Doi: 10.1016/j.jacc.2003.09.036.
7. Agarwal S., Tuzcu EM., Rodriguez ER., Tan CD., Rodriguez LL., Kapadia SR. Interventional Cardiology Perspective of Functional Tricuspid Regurgitation. Circ Cardiovasc Interv 2009;2(6):565–73. Doi: 10.1161/CIRCINTERVENTIONS.109.878983.
8. van Rosendael PJ., Joyce E., Katsanos S., et al. Tricuspid valve remodelling in functional tricuspid regurgitation: multidetector row computed tomography insights. Eur Hear J – Cardiovasc Imaging 2015;17(1):jev140. Doi: 10.1093/ehjci/jev140.
9. Campelo-Parada F., Perlman G., Philippon F., et al. First-in-Man Experience of a Novel Transcatheter Repair System for Treating Severe Tricuspid Regurgitation. J Am Coll Cardiol 2015;66(22):2475–83. Doi: 10.1016/j.jacc.2015.09.068.
10. Latib A., Agricola E., Pozzoli A., et al. First-in-Man Implantation of a Tricuspid Annular Remodeling Device for Functional Tricuspid Regurgitation. JACC Cardiovasc Interv

2015;8(13):e211-4. Doi: 10.1016/j.jcin.2015.06.028.

11. Mak GJ., Blanke P., Ong K., et al. Three-Dimensional Echocardiography Compared With Computed Tomography to Determine Mitral Annulus Size Before Transcatheter Mitral Valve Implantation. Circ Cardiovasc Imaging 2016;9(6):e004176. Doi: 10.1161/CIRCIMAGING.115.004176.
12. Sündermann SH., Gordic S., Manka R., et al. Computed tomography for planning and postoperative imaging of transvenous mitral annuloplasty: first experience in an animal model. Int J Cardiovasc Imaging 2015;31(1):135–42. Doi: 10.1007/s10554-014-0516-7.
13. Muraru D., Badano LP., Sarais C., Soldà E., Iliceto S. Evaluation of Tricuspid Valve Morphology and Function by Transthoracic Three-Dimensional Echocardiography. Curr Cardiol Rep 2011;13(3):242–9. Doi: 10.1007/s11886-011-0176-3.
14. Badano LP., Agricola E., de Isla LP., Gianfagna P., Zamorano JL. Evaluation of the tricuspid valve morphology and function by transthoracic real-time three-dimensional echocardiography. Eur J Echocardiogr 2009;10(4):477–84. Doi: 10.1093/ejechocard/jep044.
15. Díez-Villanueva P., Gutiérrez-Ibañes E., Cuerpo-Caballero GP., et al. Direct injury to right coronary artery in patients undergoing tricuspid annuloplasty. Ann Thorac Surg 2014;97(4):1300–5. Doi: 10.1016/j.athoracsur.2013.12.021.
16. Saremi F., Pourzand L., Krishnan S., et al. Right atrial cavotricuspid isthmus: anatomic characterization with multi-detector row CT. Radiology 2008;247(3):658–68. Doi: 10.1148/radiol.2473070819.
17. Lancellotti P., Tribouilloy C., Hagendorff A., et al. Recommendations for the echocardiographic assessment of native valvular regurgitation: an executive summary from the European Association of Cardiovascular Imaging. Eur Heart J Cardiovasc Imaging 2013;14(7):611–44. Doi: 10.1093/ehjci/jet105.
18. Ton-Nu T-T., Levine RA., Handschumacher MD., et al. Geometric Determinants of Functional Tricuspid Regurgitation: Insights From 3-Dimensional Echocardiography. Circulation 2006;114(2):143–9. Doi: 10.1161/CIRCULATIONAHA.106.611889.
19. Pieper S., Lorensen B., Schroeder W., Kikinis R. The NA-MIC Kit: ITK, VTK, pipelines,

grids and 3D slicer as an open platform for the medical image computing community. vol. 2006. 2006. p. 698–701.

20. Sturla F., Onorati F., Puppini G., et al. Dynamic and quantitative evaluation of degenerative mitral valve disease: A dedicated framework based on cardiac magnetic resonance imaging. J Thorac Dis 2017;9. Doi: 10.21037/jtd.2017.03.84.

21. Lee ETY. Choosing nodes in parametric curve interpolation. Comput Des 1989;21(6):363–70. Doi: 10.1016/0010-4485(89)90003-1.

22. Cleveland WS. Robust Locally Weighted Regression and Smoothing Scatterplots. J Am Stat Assoc 1979;74(368):829–36. Doi: 10.1080/01621459.1979.10481038.

23. Hinzpeter R., Eberhard M., Burghard P., et al. Computed tomography in patients with tricuspid regurgitation prior to transcatheter valve repair: dynamic analysis of the annulus with an individually tailored contrast media protocol. EuroIntervention 2017;12(15):e1828–36. Doi: 10.4244/EIJ-D-16-00891.

24. Ring L., Rana BS., Kydd A., Boyd J., Parker K., Rusk RA. Dynamics of the tricuspid valve annulus in normal and dilated right hearts: a three-dimensional transoesophageal echocardiography study. Eur Heart J Cardiovasc Imaging 2012;13(9):756–62. Doi: 10.1093/ehjci/jes040.

25. Muraru D., Veronesi F., Maddalozzo A., et al. 3D printing of normal and pathologic tricuspid valves from transthoracic 3D echocardiography data sets 2016:1–7. Doi: 10.1093/ehjci/jew215.

26. Sukmawan R., Watanabe N., Ogasawara Y., et al. Geometric changes of tricuspid valve tenting in tricuspid regurgitation secondary to pulmonary hypertension quantified by novel system with transthoracic real-time 3-dimensional echocardiography. J Am Soc Echocardiogr 2007;20(5):470–6. Doi: 10.1016/j.echo.2006.10.001.

27. Rosendael PJ Van., Joyce E., Katsanos S., et al. Tricuspid valve remodelling in functional tricuspid regurgitation : multidetector row computed tomography insights 2016:96–105. Doi: 10.1093/ehjci/jev140.

28. Farooqi KM., Sengupta PP., York N., York N. Echocardiography and Three-Dimensional Printing : Sound Ideas to Touch a Heart. J Am Soc Echocardiogr

2015;28(4):398–403. Doi: 10.1016/j.echo.2015.02.005.

29. Hoyek N., Collet C., Rastello O., Fargier P., Thiriet P., Guillot A. Enhancement of mental rotation abilities and its effect on anatomy learning. Teach Learn Med 2009;21(3):201–6. Doi: 10.1080/10401330903014178.

Chapter 4

Mass-spring models for the simulation of mitral valve function: looking for a trade-off between reliability and time-efficiency

This chapter was based on:

Pappalardo OA[1,2], Sturla F[2], Onorati F[1], Puppini G[3], Selmi M[1,2], Luciani G.B.[1], Faggian G[1], Redaelli A[2], Votta E[2]

[1] Division of Cardiac Surgery, Department of Surgery, Università degli Studi di Verona, Italy
[2] Department of Electronics, Information and Bioengineering, Politecnico di Milano, Italy
[3] Radiology, Università degli Studi di Verona, Italy,
Medical engineering & physics (2017)

4.1 Introduction

The mitral valve (MV) is located between the left atrium and the left ventricle. In physiological conditions, it allows for diastolic blood flow from the former to the latter with minimal energy dissipation, and it prevents from systolic backflow[1]. MV physiologic function requires the correct interplay of its components: annulus, leaflets, papillary muscles (PMs), which originate from the ventricular myocardium, and chordae tendineae, which connect the leaflets to the PMs[1]. In particular, in systole the annulus shrinks, the leaflets coapt and occlude the MV orifice, the PMs contract and together with chordae tendineae allow for correct leaflets positioning[1] (Fig. 4.1).

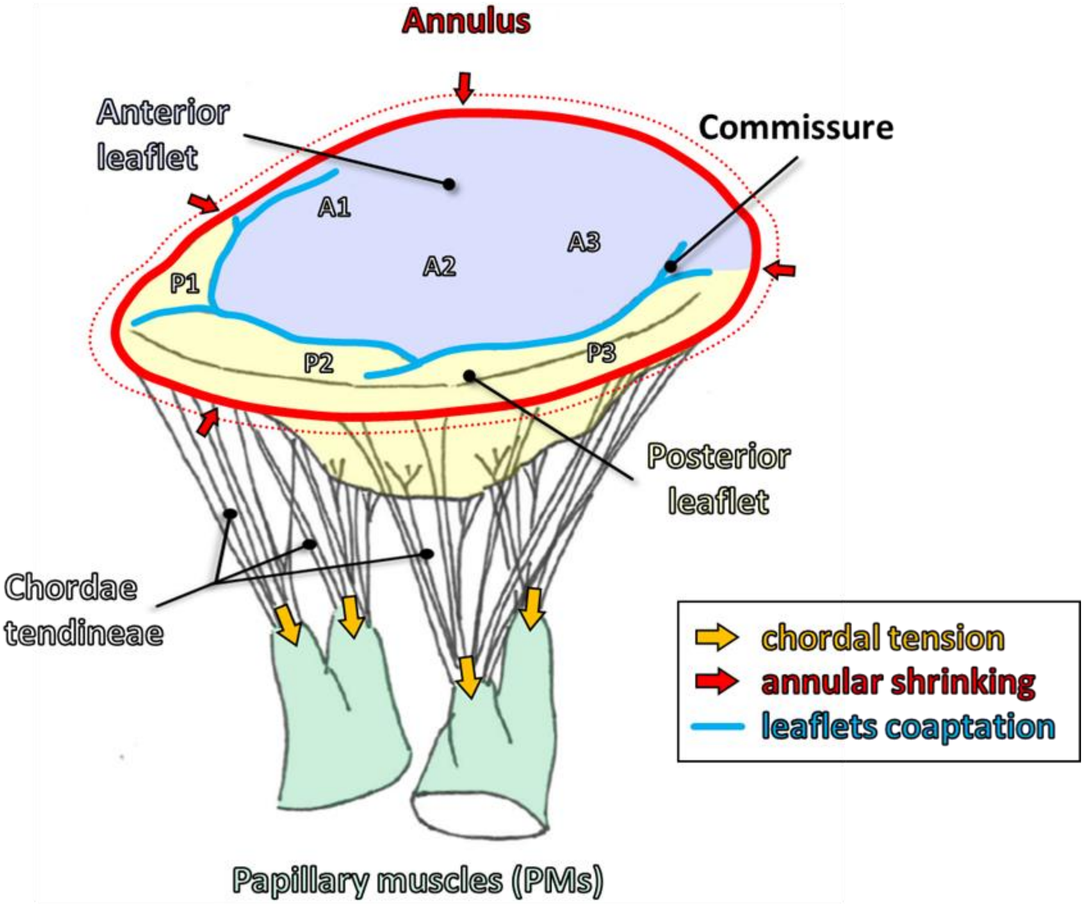

Figure 4.1 – Anatomy and systolic function of the mitral valve, pointing out annular shrinking (red arrows), leaflets coaptation (blue line) and chordal tensions (orange arrows). A1, anterior segment; A2, middle segment; A3, posterior segment; P1, anterolateral scallop; P2, middle scallop; P3, posteromedial scallop.

When this mechanism is altered, mitral regurgitation (MR) occurs. MR is rather common: degenerative MR alone, i.e. the most frequent MR etiology, affects about 2% of the general population in the Western world[2]. The only effective treatment for MR is surgery, MV repair being the procedure of choice over MV replacement owing to lower surgical mortality and better long-term preservation of left ventricular function[3,4]. However, the anatomical and functional complexity of the MV makes surgical repair technically demanding, requiring longer learning curves and expertise in the selection of the most effective techniques for a given scenario[5]. Moreover, in open heart surgery the intraoperative evaluation of the surgical outcome is performed on a motionless and almost flaccid heart, making it difficult to correctly predict the actual post-operative MV function[6]. As a result, MV repair is performed on 50-60% of patients although more than 90% of patients can be treated when referred to highly specialized centers[7].

In order to help identifying more robust criteria to select and tune MV repair techniques in different clinically relevant scenarios, and to test novel concepts, different research groups have proposed computational models to simulate the post-operative MV function based on its baseline pre-operative conditions[8–11]. The current generation of these models exploits the detailed anatomical information yielded by medical imaging to provide patient-specific analyses, paving the way towards the development of virtual surgical-planning tools[12–20].

However, the vast majority of these models are based on the finite element (FE) approach and are far too time-demanding to be used in a real clinical setting[21]. In the pursue of time-efficiency, two alternative approaches have been proposed, mainly borrowed from computer graphics.

The co-rotated linearized FE method was used to simulate MV function based on 3D ultrasound imaging, and to predict the effects of MR treatment by means of the transcatheter Mitraclip® device[22–24]. That method proved capable of simulating the systolic loading of MV leaflets and computing their deformed configuration *in vivo* with mismatches within 6 mm vs. ground truth data. Notably, thanks to the integration of the simulation environment with automated image processing algorithms, simulations yielded results within approximately 15 minutes, including MV anatomy reconstruction, iterative model fine tuning and numerical simulation.

Mass-spring models (MSMs), which differ from FE models in that they describe a continuum structure as a discrete cloud of nodal masses connected through a mesh of springs, were used to simulate the effects on MV dynamics of chordae tendineae surgical modification[25] and of annuloplasty[26] almost in real-time. Both these studies used microcomputed tomography to reconstruct baseline and post-surgery MV anatomy *in vitro*, with fixed annulus and papillary muscles. Hence, it was possible to assess the mismatches between the computed systolic configuration of MV leaflets vs. extremely precise ground truth data (100 µm spatial resolution). Such mismatches were of few millimeters at worst. These evidences suggest that MSMs may provide an effective trade-off between time-efficiency and reliability, and could support surgical planning in MV repair by simulating the effects of MV surgery accounting for the patient-specific MV anatomy. However, to verify this hypothesis it would be mandatory to test the reliability of MSMs when modeling MV dynamics based on *in vivo* clinical imaging, at least by comparing computed results vs. those yielded by state-of-the-art FE models. A comparison of this kind was reported only in[21], but with reference to an idealized aortic valve, whose anatomy is inherently much simpler than MV structure.

On this basis, we implemented the image-based MSM of three healthy MVs, applied it to the simulation of their systolic closure, and we compared its capability to correctly compute the systolic configuration of the considered MVs vs. state-of-the-art subject-specific FE models. In this process, we also quantified the computational expense related to the use of proposed MSM modeling approach.

4.2 Image-based mitral valve geometrical modeling

Following a well-established protocol[27], cardiac magnetic resonance (cMR) imaging was performed on three healthy subjects through a 3.0 TTX Achieva system (Philips Medical Systems, Irvine, Calif). Cine-sequences with 1.25 mm in-plane resolution and 8 mm slice thickness were acquired.

Through in-house software implemented in Matlab® (MATLAB, The MathWorks Inc, Natick, Mass), MV annulus, leaflets and PMs were manually traced in the tele-diastolic frame, i.e., the last frame preceding transient leaflets closure, when the MV was assumed stress-free. Data yielded by manual tracing were automatically filtered and used to reconstruct the 3D geometry of annulus and leaflets, whose non-uniform and compound curvature was accounted for[16], and for the 3D position of PMs tips.

4.3 Finite element models

FE models were implemented in ABAQUS/Explicit 6.10 (SIMULIA, Dessault Systèmes). Leaflets geometry was discretized into approximately 35000 triangular and linear shell elements (characteristic dimension 0.2 mm), with regionally varying thickness from previous studies[28]. As in[27], a complete chordal apparatus, including branches, was defined based on *ex vivo* findings[29,30], and each chorda was discretized into multiple truss elements. MV tissues were described as soft tissues with homogeneous density (1100 kg/m^3, which was increased by a factor of ten to account for blood inertia and to speed up simulations), with hyperelastic stress-strain properties. As in[31], leaflets tissue was modeled as transversely isotropic through the invariant-based strain energy function proposed in[32], assuming the presence of collagen fibers preferentially oriented parallel to the annulus within the tissue. Chordae tendineae stress-strain behavior was modeled through a 2nd order polynomial model (first order and strut chordae) and a 5th order Ogden model (2nd order chordae), fitting the experimental data reported by Kunzelman[33].

Systolic MV closure until peak systole was simulated by imposing a time-dependent P(t) pressure on the ventricular side of MV leaflets:

$$P = 60mmHg \cdot (\sin\left(4\pi t - \frac{\pi}{2}\right) + 1); \qquad t \in [0;\ 0.25\ s]$$

(Eq. 4.1)

Concomitantly, time-dependent nodal displacements were imposed to the nodes representing the PM heads and to those laying on the annulus. Imposed displacements were obtained based on the PMs and annulus profile traced frame-by-frame on cMR images, as in[16].

Leaflets contact was modeled through the scale penalty algorithm available in ABAQUS/Explicit, assuming a 0.05 friction coefficient[8,27,34].

FE simulations were parallelized on 16 CPUs on a scientific workstation (Intel Xeon 2.93 GHz, 16 CPUs, 100 GB RAM).

4.4 Mass-spring models

For each MV, the leaflet mesh generated for the FE model was subsampled through Meshmixer (Autodesk, Inc, San Rafael, CA USA) to obtain the corresponding MSM, in which nodes and element edges were treated as masses and springs, respectively. Three different levels of spatial resolution were considered (Fig. 4.2 and Table 4.1): coarse, intermediate and fine. The chordal apparatus was based on the same scheme adopted in FE elements, but each chorda was modeled as a single spring, neglecting branches.

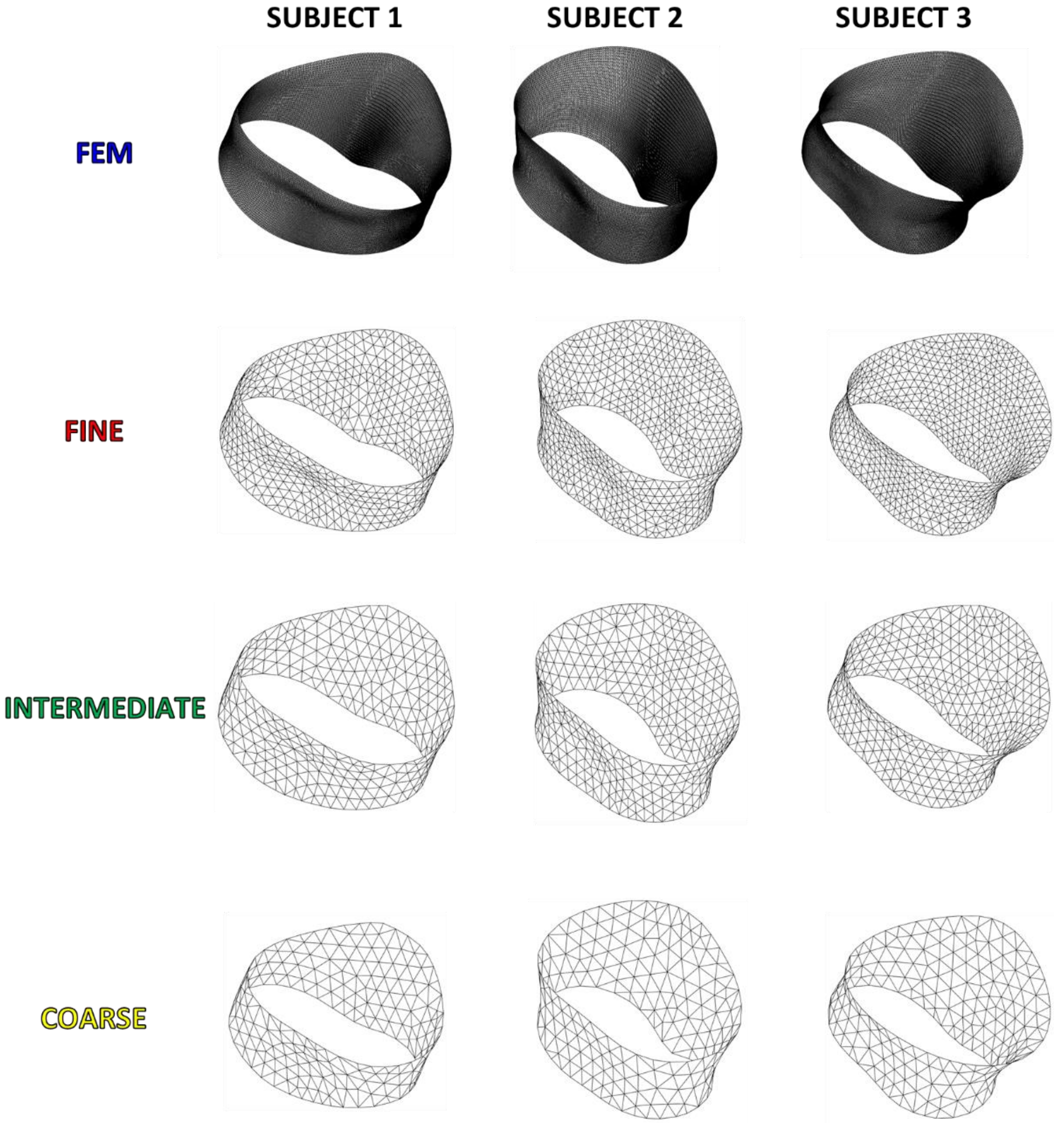

Figure 4.2 – Mitral valve discretized geometries used in MSMs.

MSM Meshes			
	Fine	**Intermediate**	**Coarse**
Number of elements	1250	700	320
Number of nodes	700	400	200
Characteristic dimension[mm]	1.8	2.5	3.5

The dynamics of the masses was computed through an explicit forward Euler scheme, which was implemented in Matlab®:

$$\begin{cases} \ddot{\boldsymbol{x}} = \frac{\boldsymbol{F}}{\boldsymbol{M}} \\ \dot{\boldsymbol{x}}(t+\Delta t) = \dot{\boldsymbol{x}}(t) + \Delta t\ddot{\boldsymbol{x}} \\ \boldsymbol{x}(t+\Delta t) = \boldsymbol{x}(t) + \Delta t\dot{\boldsymbol{x}}(t) \end{cases}$$

(Eq. 4.2)

where **M** is the matrix of the masses, $\boldsymbol{F}$ is the matrix of the system forces, $\ddot{\boldsymbol{x}}, \dot{\boldsymbol{x}}$ and $\boldsymbol{x}$ are the matrix respectively of acceleration, velocity and position of the nodes, and $\Delta \boldsymbol{t}$ is the integration time increment, set to $2.5\cdot10^{-7}$s. The mass of the i-th node of the mesh was:

$$m_i = \frac{\sum_j A_j h_i \rho}{3}$$

(Eq. 4.3)

where $\sum_j A_j$ is the total surface area of the elements sharing the node, ρ is the density of the tissue, which was set to 1100 Kg/m^3, and h_i is the tissue thickness at the node, set accordingly with the same leaflet thickness distribution adopted in the FE models.

The force $\boldsymbol{F}$ acting on each node is decomposed as:

$$\boldsymbol{F} = \boldsymbol{F_{tissue}} + \boldsymbol{F_{press}} + \boldsymbol{F_{cont}} + +\boldsymbol{F_{visc}}$$

(Eq. 4.4)

where $\boldsymbol{F_{tissue}}$ is the resultant force exerted by the springs sharing the node, which model the mechanical response of MV tissues. Springs' elastic constant k was defined so to account for the non-linear and anisotropic stress-strain behavior of MV tissues whenever relevant.

As regards leaflets, k was defined as:

$$k = k(\varepsilon, \alpha_0) = E(\varepsilon, \alpha_0)\frac{h\sum_i A_i}{{l_0}^2}$$

(Eq. 4.5)

where h is the local leaflet thickness, defined as the mean value of the thickness values assigned to the two nodes at the ends of the spring, $\sum_i \boldsymbol{A_i}$is the surface area of the triangular elements sharing the spring, $\boldsymbol{l_0}$ is the initial length of the spring and $\boldsymbol{E(\varepsilon, \alpha_0)}$ is the elastic modulus of the leaflet tissue. $\boldsymbol{E(\varepsilon, \alpha_0)}$ is a function of the spring strain $\boldsymbol{\varepsilon}$ and of the spring initial orientation, defined by the angle α_0 between the spring and the circumferential direction, assumed the preferential direction of the collagen fibers within the leaflet tissue (Fig. 4.3):

$$E(\varepsilon,\alpha_0) = \sqrt{{E_{cf}}^2(\varepsilon)\sin^2\alpha_0 + {E_f}^2(\varepsilon)cos^2\alpha_0}$$

(Eq. 4.6)

where $\boldsymbol{E_f(\varepsilon)}$ and $\boldsymbol{E_{cf}(\varepsilon)}$ are the strain-dependent elastic modulus values in the fiber (*f*) and cross-fiber (*cf*) direction, respectively, which were defined based on a two-step procedure.

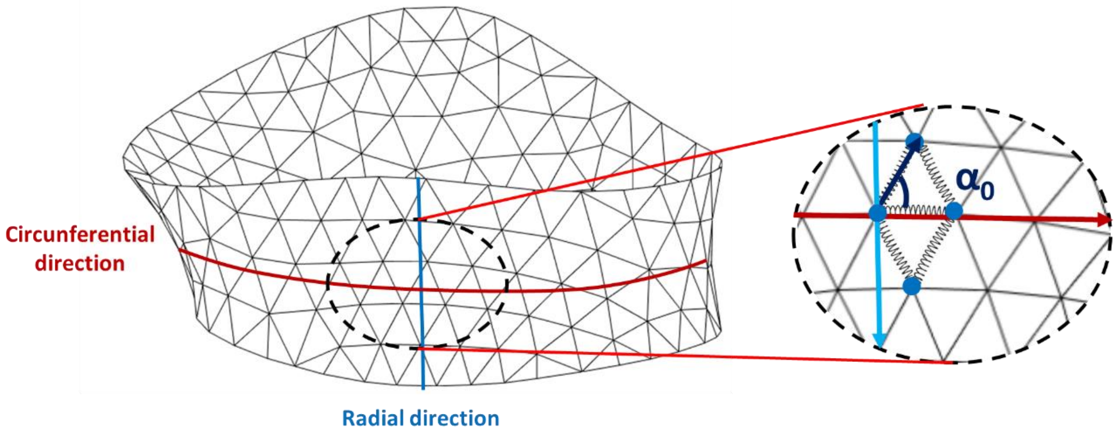

Figure 4.3 – Detail of the leaflet mesh depicting two triangular elements sharing a spring, which connects two point masses.

First, the experimental stress-strain in data reported in[35] for the *f* and *cf* directions based on equi-biaxial tensile tests on porcine MV leaflets were approximated through a piecewise function:

$$\sigma(\varepsilon) = \begin{cases} m\varepsilon, & \varepsilon < \varepsilon_{lim} \\ Ae^{B\varepsilon}, & \varepsilon \geq \varepsilon_{lim} \end{cases}$$

(Eq. 4.7)

where $\boldsymbol{\varepsilon_{lim}}$ is the strain value characterizing the transition from the low-stiffness to the high-stiffness region of the stress-strain curve. A, B and m are parameters that were identified through least square fitting of the experimental data (Fig. 4.4.a). Their values are reported in Table 2 for directions *f* and *cf*, for the anterior and posterior leaflet.

Second, $E_f(\varepsilon)$ and $E_{cf}(\varepsilon)$ were obtained as the first derivative of the corresponding fitted function with respect to ε:

$$E_i(\varepsilon) = \frac{d\sigma_i}{d\varepsilon_i}; \quad i = f, cf$$

(Eq. 4.8)

As regards chordae tendineae, k was defined as:

$$k = \frac{E(\varepsilon)A_{cross\_0}}{l_0}$$

(Eq. 4.9)

where $\boldsymbol{l_0}$ and $\boldsymbol{A_{cross\_0}}$ are the initial length and cross-sectional area of the chorda, respectively, and $\boldsymbol{E(\varepsilon)}$ is the strain-dependent elastic modulus of chordae tissue. As for the leaflets, $E(\varepsilon)$ was defined through two steps. First, stress-strain data from uniaxial tensile tests on marginal, basal chordae[33] were approximated with a parabolic polynomial function while structural chordae[36] were approximated with a cubic polynomial function:

$$\sigma = a\varepsilon^3 + b\varepsilon^2 + c\varepsilon + d$$

(Eq. 4.10)

where the parameters a, b, c, d were identified for each chorda type via least square fitting (Fig. 4.4b and Table 4.2). Second, $\boldsymbol{E(\varepsilon)}$ was obtained as the first derivative of the fitting function.

Table 4.2 – Parameters defining the stress-strain behavior of MV tissues in the mass-spring models.

		Leaflets		
	Anterior Fiber	**Anterior Cross-Fiber**	**Posterior Fiber**	**Posterior Cross-Fiber**
m [Pa]	10^4	10^4	10^4	10^4
A [Pa]	0.18	0.13	0.11	$6.98 \cdot 10^{-3}$
B [-]	73.83	96.22	57.52	63.23
$\boldsymbol{\varepsilon_{lim}}$ **[-]**	0.12	0.17	0.17	0.20
		Chordae Tendineae		
	Marginal	**Basal**	**Structural**	
a [kPa]	0	986086	0	
b [kPa]	200595	-24028	152585	
c [kPa]	678.02	1082.3	515.75	
d [kPa]	-43.11	-4.30	-32.79	
$\boldsymbol{A_{cross}}$ **[m²]**	$0.40 \cdot 10^{-6}$	$0.70 \cdot 10^{-6}$	$1.20 \cdot 10^{-6}$	

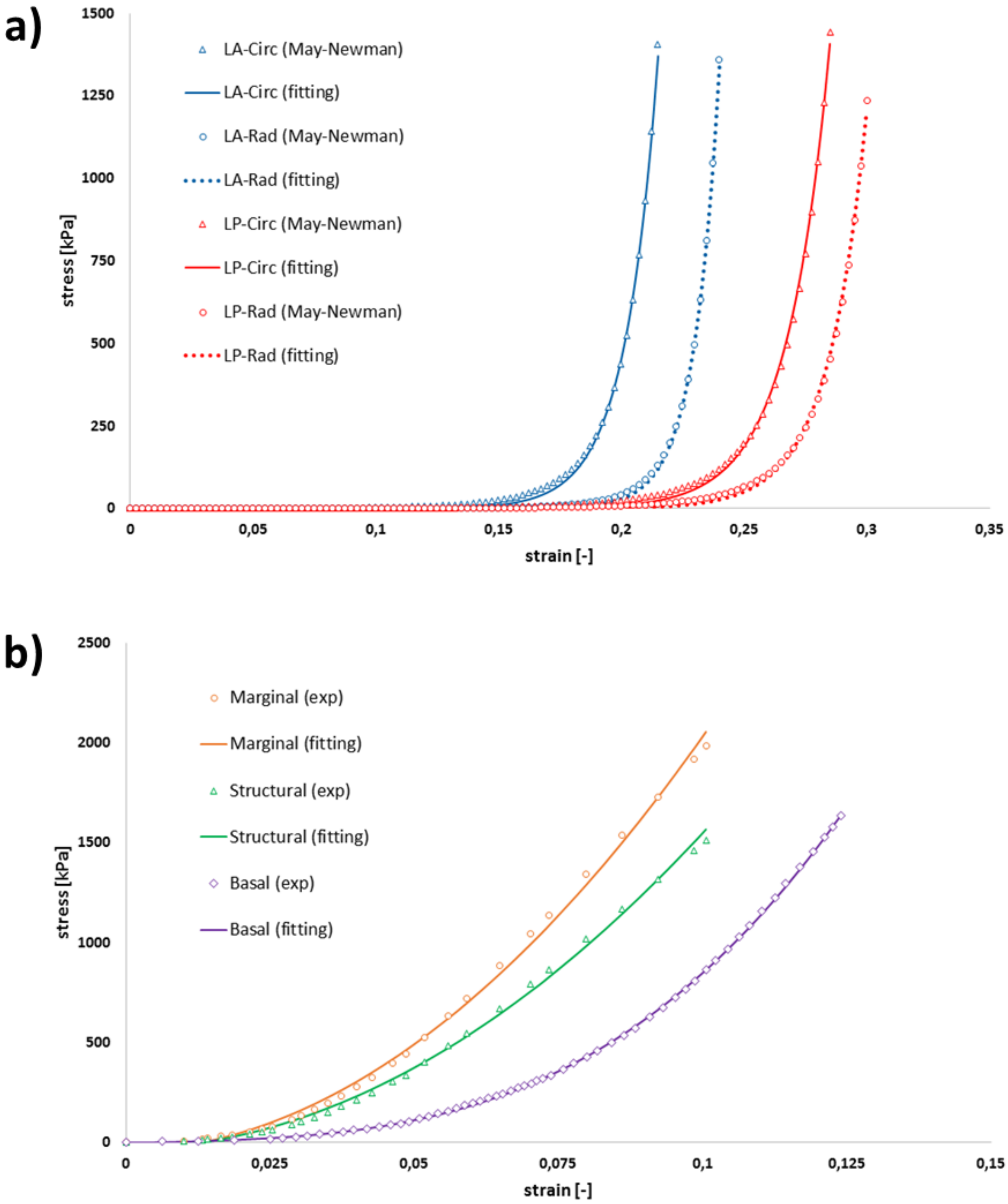

Figure 4.4 – Experimental stress-strain data and fitting functions used for the (a) leaflets and (b) chordae material model.

Owing to the non-linearity of the springs, $\boldsymbol{F_{tissue}}$ was computed through the following linearization:

$$\boldsymbol{F_{tissue}}(t) = \sum_i \left[\left\| \boldsymbol{F_{tissue\_i}}(t - \Delta t) \right\| + k_i(t)\left(l_i(t) - l_i(t - \Delta t)\right) \right] \boldsymbol{u_i}(t)$$

(Eq. 4.11)

where $\left\|\boldsymbol{F_{tissue\_i}}(\boldsymbol{t}-\Delta\boldsymbol{t})\right\|$ is the magnitude of the force of the i-th spring insisting on the node at the previous step, $\boldsymbol{l_i}(\boldsymbol{t})$ and $\boldsymbol{l_i}(\boldsymbol{t}-\Delta\boldsymbol{t})$ represent the corresponding length of the spring at current and previous time step, respectively, $\boldsymbol{k_i}(\boldsymbol{t})$ is the corresponding stiffness at the current step defined by either Eq. 4.2 or Eq. 4.6, and $\boldsymbol{u_i}(\boldsymbol{t})$ is the corresponding unitary vector defining the current direction of the spring.

$\boldsymbol{F_{press}}$ is the force due to the time-dependent transvalvular pressure, which was the same imposed in the FE models (Eq. 4.1). $\boldsymbol{F_{press}}$ was defined as:

$$\boldsymbol{F_{press}} = \frac{P\sum_i A_i \boldsymbol{n_i}}{3}$$

(Eq. 4.12)

where $\boldsymbol{P}$ is the pressure and $\sum_{\boldsymbol{i}} \boldsymbol{A_i n_i}$ is the vectorial sum of the oriented surface areas of the triangular elements sharing the node.

$\boldsymbol{F_{cont}}$ is the force due to contact interactions involving a node, and is computed through an *ad hoc* algorithm. Given two triangulated surfaces S_A and S_B, the nodal masses of each surface can interact with the triangular faces of the complementary surface. This interaction is managed through the following steps:

- in the initial configuration of the MV, for every triangular element the maximum distance between its center of mass and each of its three nodes is computed:

$$d_j^{max} = max\left(\left\|\frac{\sum_{i=1}^{3}\boldsymbol{X}_i}{3} - \boldsymbol{X}_i\right\|\right) \qquad i = 1,2,3$$

(Eq. 4.13)

where $\boldsymbol{X}_i$ is the position of the i-th nodes in the j-th element. A threshold distance $\bar{\boldsymbol{d}}^{\boldsymbol{e}}$ is set as the average of $\boldsymbol{d_j^{max}}$ over the triangular elements.

- contact between, e.g., a nodal mass m_i of S_A and an element e_j of S_B occurs at time t if two conditions are fulfilled. First, at time t the distance d_{ij}^{e} from m_i to the center of mass of e_j is shorter than $\bar{d}^e$. Second, at time $(t+\Delta t)$ the signed distance d_{ij}^{π} from m_i to the plane π_j of e_j is shorter than a second threshold value $\bar{d}^{\pi}$, empirically set to 1 mm. In this case, the contact force [25] was computed as:

$$\boldsymbol{F_{cont}}(\boldsymbol{t}) = \begin{cases} \|\boldsymbol{F}(\boldsymbol{t})\| e^{-\frac{k d_{ij}^{\pi}(\boldsymbol{t})}{F_{tot}}}\boldsymbol{n} & d_{ij}^{\pi}(\boldsymbol{t}) > 0 \\ \left(\|\boldsymbol{F}(\boldsymbol{t})\| - k d_{ij}^{\pi}\right)\boldsymbol{n}(\boldsymbol{t}) & d_{ij}^{\pi}(\boldsymbol{t}) \leq 0 \end{cases}$$

(Eq. 4.14)

where k is equal to 10 N/m.

To reduce computational expense, contact was modeled between each of three regions in the anterior leaflet (A1, A2, A3) and the corresponding region in the posterior leaflet (P1, P2 and P3) (Fig. 4.5). Also, contact forces were updated every ten time increments. The contact algorithm was handled by a binary Mex file (C code).

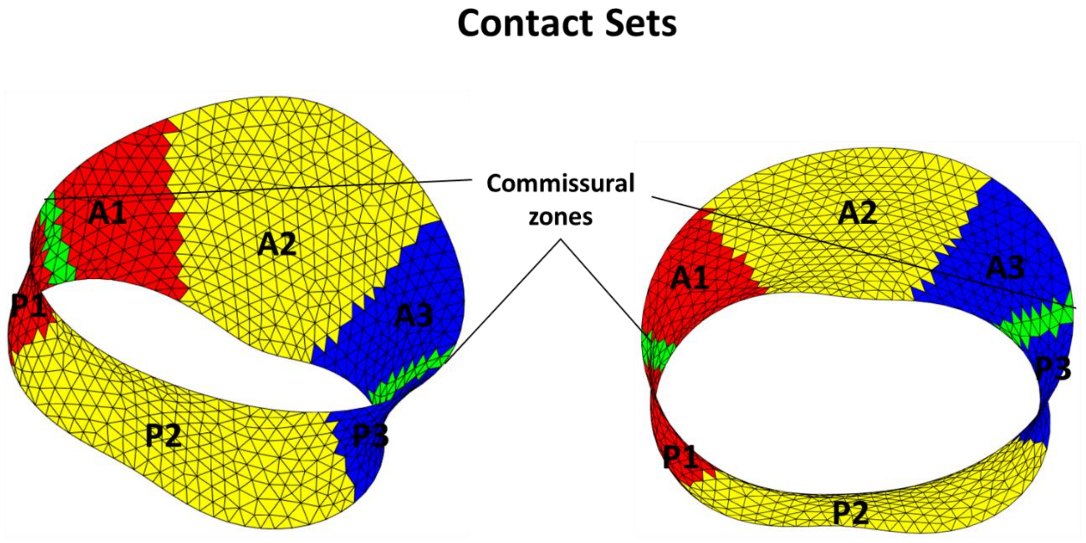

Figure 4.5 – MV leaflet regions identified when modeling contact. Each of the three posterior scallops (P1, P2, P3) interacts with the corresponding region on the anterior leaflet (A1, A2, A3). Correspondence is identified by color code. Contact modeling does not involve the commissural regions, highlighted in green.

$\boldsymbol{F_{visc}}$ is a viscous force that does not model any viscoelastic behavior of MV tissues, but it is a numerical contribute able to improve the solver stability. Of note, this approach is consistent with numerical integration strategies available in commercial solvers, e.g. Abaqus[37].

$\boldsymbol{F_{visc}}$ is defined as:

$$\boldsymbol{F_{visc}} = -\eta \dot{\boldsymbol{x}}$$

(Eq. 4.15)

where $\dot{\boldsymbol{x}}$ is the velocity of the considered node and η is the viscosity, which was set to 0.001 Pa·s[25].

As for FE simulations, time-dependent kinematic boundary conditions were imposed to the nodes representing the annulus and the PMs to simulate the corresponding motion, based on cMR images.

MSM simulations were run on a desktop pc (Intel Core i5 processor, 16 GB RAM) on a single CPU. The computational expense associated to contact forces computation and linearization of $\boldsymbol{F}_{\boldsymbol{tissue}}$ was assessed using the Matlab® profiler.

4.5 Results

4.5.1 Computed mitral valve systolic configuration

MV leaflets' geometry at peak systole as computed through numerical models was compared vs. ground truth data. To this aim, the leaflet surface was manually traced on cMR images at peak systole, identified as the frame halfway between the tele-diastolic frame and the tele-systolic frame, which was defined as the last frame preceding transient leaflet opening. The coordinates of the traced points were regularized via locally weighted non-parametric regression fitting and triangulated to obtain the discretized surface of the ground truth data. For each numerical model, the Euclidian node-to-ground truth surface distance was computed as field variable (Fig. 4.6). For subjects 2 and 3, a similar pattern was observed: in the anterior leaflet a relatively broad region was characterized by peak distance values up to 3.2 mm, while in the posterior leaflets isolated hot spots up to 3.7 mm were computed. For both subjects, the MSMs and the corresponding FE model yielded consistent distance patterns and the region-dependent peak values. Differently, for subject 1 wide regions of high node-to-surface distance values were obtained on both leaflets, ranging between 2.4 and 4.7 mm. This pattern was consistently captured by the FE model and by the MSMs, but peak distance values were smaller in the MSMs as compared to those obtained for the FE model.

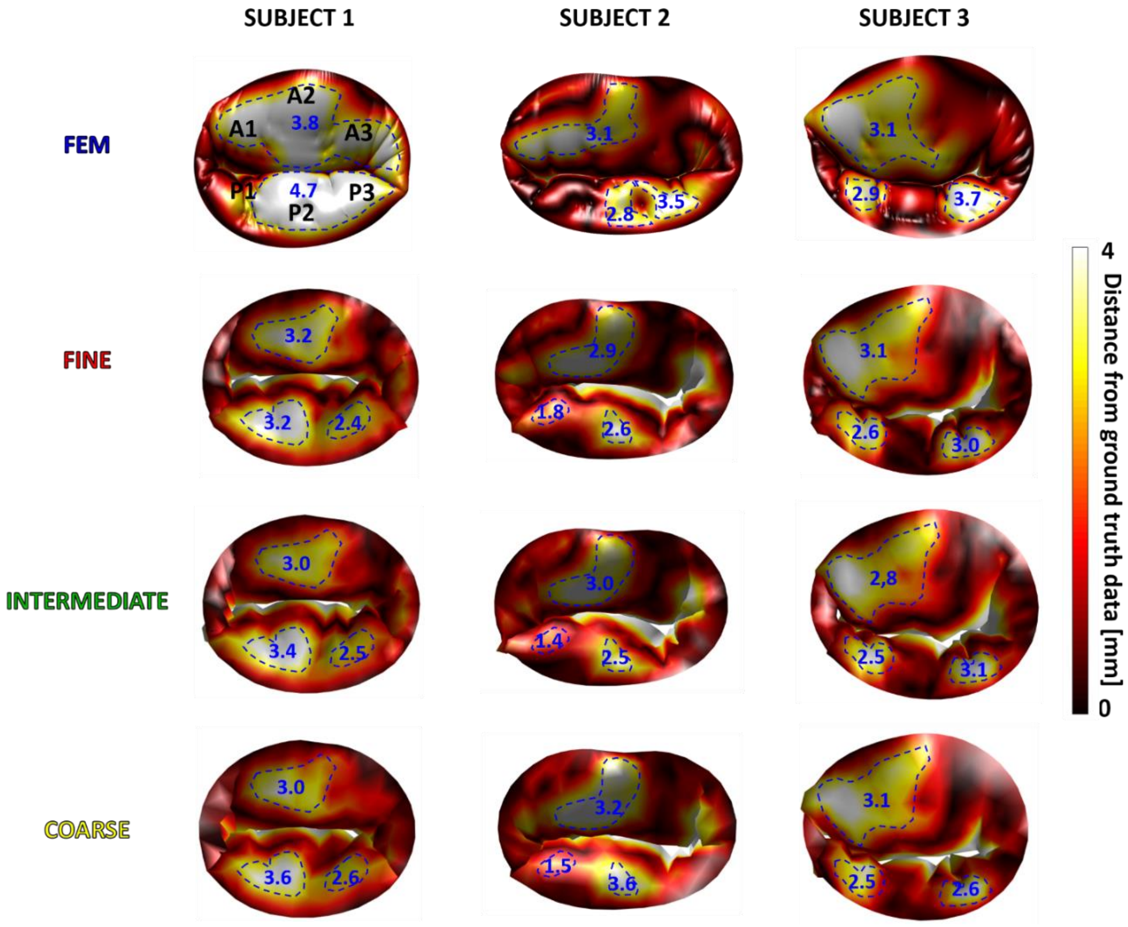

Figure 4.6 - Heat map of the Euclidian node-to-surface distance between nodes of the models (MSM and FE) and the corresponding ground truth surface of the MV leaflets at peak systole (transmitral pressure P=120 mmHg).

For each subject and for each model, regions characterized by high distance values are silhouetted by a dashed line, and the corresponding median value (in mm) is indicated.

This analysis was further deepened by comparing the leaflet profile computed by numerical models vs. the corresponding ground truth datum on a two-chamber view, where both the anterior and posterior leaflets are visible (Fig. 4.7). For every simulated MV, leaflets' profile was displaced towards the atrial cavity as compared to ground truth data. This issue was more evident for the anterior, where such displacement was in the range 2.7÷4.1 mm and 2.0÷4.1 mm for the FE models and MSMs, respectively. Nonetheless, physiological coaptation was obtained in every model: the mean value of MV leaflets' tenting height defined as the local signed apical-oriented distance from the 3D surface that interpolates the MV orifice[38], ranged from 1.76 to 3.6 mm, slightly overestimating data from healthy subjects[38,39].

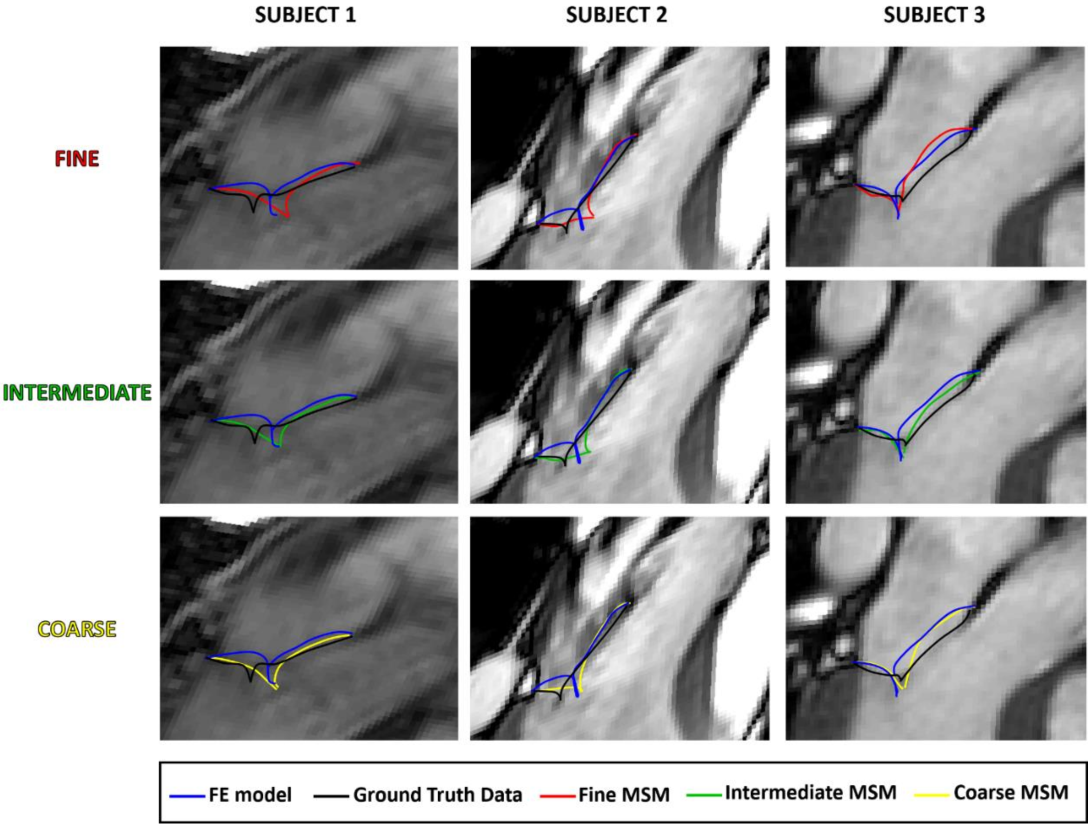

Figure 4.7 – Detail of the MV leaflets profile at peak systole on a two-chamber view, as computed by FE models (blue line) and by MSMs with fine (red line), intermediate (green line), and coarse (yellow line) mesh. Computed profiles are visually compared to the corresponding ground truth data (black line) from the same cross-sectional plane.

Also, differences in leaflets' configuration as obtained through FE models and MSMs were quantified. The Euclidean node-to-surface distance between MSM leaflet nodes and the corresponding FE leaflet surface was computed (Fig. 4.8). Peak distances were always within 4 mm, and were located at P2, P3 and A3 for subjects 1, 2 and 3, respectively. For each simulated MV, no relevant effect of the mesh refinement level in the MSMs was observed on the distance distribution over the leaflets.

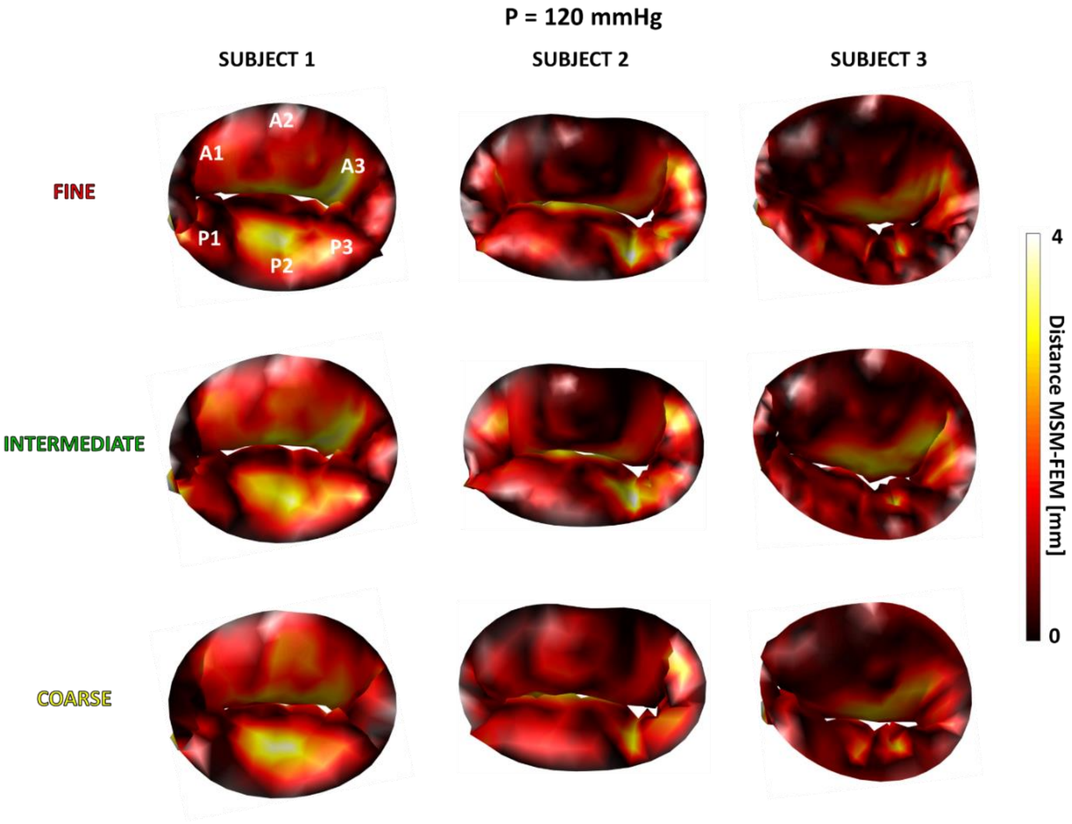

Figure 4.8 – Heat map of the node-to-surface distance between MSM nodes and the corresponding FE model surface of the MV leaflets at peak systole (transmitral pressure P=120 mmHg).

4.5.2 Computed mitral valve closure dynamics

The distribution of the Euclidian node-to-surface distances between MSM leaflet nodes and the corresponding FE leaflet surface was analyzed throughout MV transient closure for progressively higher pressure values (P=10, 80, and 120 mmHg). For each pressure value, differences between results yielded by different MSM mesh refinement levels were statistically assessed through Kruskal-Wallis test (Dunn's post hoc) in GraphPad Prism 7 (GraphPad Software Inc., La Jolla, CA, USA), with a p-value < 0.05 considered significant (Fig. 4.9). At a 10 mmHg pressure, i.e., when the MV was still open, statistically significant differences between different MSM mesh refinement levels were observed. In particular, the 95th percentile of the distance distribution increased up to 4 mm for coarse meshes, and decreased to less than 2 mm for intermediate meshes. At 80 and 120 mmHg pressures, no statistically significant differences between different MSM mesh refinement levels were found. For these two loading conditions, the 75th of the distance distribution was lower than 1.5 and 2 mm, respectively, and the 95th of the distance distribution was lower than 3 mm.

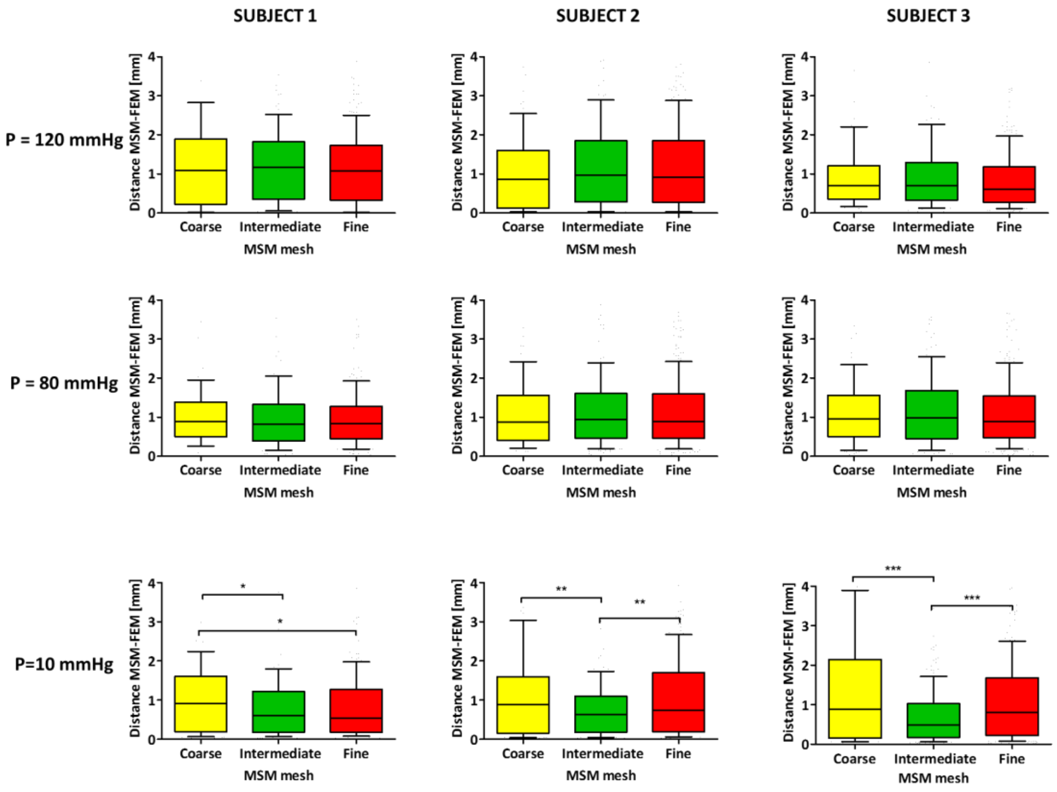

Figure 4.9 - Boxplots of the distribution of the node-to-surface distance between leaflet nodes of the MSMs and the leaflet surface of the corresponding FE model. For each modeled MV, data are reported through boxplots for three different values of trans-mitral pressure (P=120 mmHg, top row; P=80 mmHg, mid row; P=10 mmHg, bottom row) and for three levels of mesh refinement: red=fine; green=intermediate; yellow=coarse. Boxes indicate values ranging from the 25th to the 75th percentile, and the horizontal line within each box indicates the median value; whiskers indicate the 5th and 95th percentile, respectively. For each pressure value, data obtained with different mesh refinement levels were statistically compared through Kruskal-Wallis test (Dunn’s post hoc): *=$p<0.02$; **=$p<0.01$; ***=$p<0.0001$.

4.5.3 Computational expense of Mass-spring and finite element models

FE simulations required 73-98 minutes. Simulations run through MSMs required less than 10 minutes when coarse meshes were used, and up to 37-61 minutes when fine meshes were used (Table 4.3). This increase in computational expense is mostly due to contact modeling, which requires 3-4 minutes for coarse meshes, and 26-49 minutes for fine meshes. On the opposite, the modeling of tissues’ non-linear mechanical properties only marginally affects the computational expense of MSMs, independently of the mesh refinement level.

Table 4.3 – Computational expense of the simulations performed through MSMs. The percentage expense associated to the modeling of contact and of tissues' non-linear mechanical properties is highlighted.

Computational Cost					
		Total Time [min]	**Contacts Time [%]**	**Non-Linearity Time [%]**	**Time of the other Characteristic [%]**
Subject 1	fine	36.67	71.86	8.09	20.05
	intermediate	16.47	55.57	11.23	33.2
	coarse	9.25	40.36	12.97	46.67
Subject 2	fine	56.45	79.24	6.52	14.23
	intermediate	24.12	64.89	9.61	25.5
	coarse	8.8	39.58	13.26	47.16
Subject 3	fine	60.77	80.17	6.23	13.6
	intermediate	26.6	67.23	9.27	23.5
	coarse	9.85	43.15	12.69	44.16

4.6 Novelty of the study

The simulation of MV function through MSMs accounting for anatomically detailed geometry was previously proposed by different authors as a possible tool to support surgical planning. Hammer and colleagues exploited the high-fidelity data yielded by micro-CT to model the *in vitro* closure of an isolated mitral valve and compare numerical results vs. *in vitro* evidence obtained under controlled conditions[21], but in absence of annular dynamics and PMs motion. Skornitzke and co-workers[40] based their geometrical model on 3D ultrasound data acquired in vivo, yet they neglected the motion of PMs and annulus. Also, in both these studies the mechanical response of MV leaflet tissue was described either as linear[40] or piecewise-linear[21], and the differences between the anterior and posterior leaflet were neglected.

To the best of our knowledge, in the present work we presented the first MV MSM based on *in vivo* images able to combine the modeling of both PMs and annulus motion with the different anisotropic and non-linear mechanical properties of MV leaflets.

4.7 Comparative analysis of mass-spring models reliability vs. finite element models

The deformed configuration of MV leaflets as computed by MSMs was compared vs. the corresponding configuration obtained through FE modeling, and vs. ground truth data. At peak systole, both numerical approaches moderately overestimated the displacement of the leaflets towards the atrium as compared to ground truth data. The largest mismatches were about three times the in-plane resolution of the cMR images used in the study. Somewhat counterintuitively, for every simulated MV such mismatch was smallest when the configuration obtained through MSMs with an intermediate level of mesh refinement was considered.

When systolic peak configurations computed by MSMs were compared to those obtained through FE modeling, mismatches by less than twice the in-plane resolution of cMR data were detected over 75% of the leaflets' surface (Fig. 8), independently of the mesh refinement and of the specific MV considered. These mismatches were unlikely caused by the presence of a bias, as suggested by variability of magnitude and location of the peak mismatches in the different simulated MVs. Greater mismatches between the deformed configurations yielded by FE models and MSMs were observed during transient closure, mostly when coarse meshes for the MSMs were considered. This result could be due to the fact that larger nodal masses are inherently associated to the use of a coarser mesh; these necessarily have a greater inertia during transient closure, resulting in a delayed motion of the leaflets.

4.8 Analysis of mass-spring models performance

The modeling of leaflet tissue anisotropic and non-linear mechanical properties had a minor impact on the performance of MSMs. The computational cost of simulations was largely determined by contact modeling. Of note, the time expense of contact modeling typically depends more than linearly on the number of nodal masses; yet, in our MSMs the time required by MSM simulations increased almost linearly with the number of nodal masses as progressively finer leaflet meshes were used.

4.9 Limitations

Our analyses highlighted three main limitations.

The first limitation is related to the simplifying assumptions we adopted when modeling the geometry of the MV, and more specifically, the chordal apparatus. The number of chordae, their branching pattern and the location of their insertions onto the leaflets are described based on a standard template[27]. This limitation likely has an impact on the systolic configuration of the leaflets, particularly in the basal region, where the amount and the location of chordal insertions is highly variable over different valves.

The second limitation is inherent to the MSM approach, which allows for computing the loaded configuration of a structure but does not allow for a reliable computation of the associated stress field, as shown in the elegant analysis reported in[21]. Therefore, in the context of simulating the effects of MV surgical repair, this approach would be suitable to predict post-surgery MV geometry, but not to test whether clinically relevant mechanical stimuli characterize such geometry.

The third limitation is due to our implementation of the MSM approach, and in particular of our modeling of contacts. The algorithm we implemented cannot robustly treat the contact between elements that share nodes when these nodes behave as hinge points. As a consequence, we could not model contact in the commissural regions, where leaflet tissue folds and nodes at the commissures function as hinges for the anterior and posterior leaflet, respectively. Moreover, with the aim to reduce the computational expense of MSM simulations, we assumed that contact could occur only between each cusp of the posterior leaflet (P1, P2, P3) and the corresponding region of the anterior one (A1, A2, A3). As a result, we did not account neither for contacts between not corresponding regions, e.g., between P1 and A2, nor for potential self-contacts. Overall, these simplifications led to minor leaflet penetrations, although these did not impact on the loaded MV configuration (Fig. 4.8).

4.10 Applicative perspective

Altogether, data on MSMs computational performance and data from the comparison of MSMs vs. FE models suggest that, as long as the focus of the analysis is computing the MV configuration at high systolic pressure values, MSMs with intermediate or coarse meshes can be as reliable as state-of-the-art FE models, while reducing computational expense to few minutes even when a standard laptop is used. Hence, MSMs could represent a suitable trade-off between almost real-time simulations and reliability, with the potential to be used in surgical planning or in virtual surgical training. In the context of surgical planning, MSMs could be exploited to simulate different surgical options[41], e.g., neochordoplasty, annuloplasty, leaflet resection, and their potential combination, to compare the corresponding systolic MV configurations in terms of those geometrical indexes that are indicators of repair durability, such as coaptation length and tenting height[42,43]. In the context of surgical training, the possibility to simulate MV surgical repair on a wide cohort of valves, to reproduce on each valve different techniques, and to tune the corresponding key features (e.g. annuloplasty ring size, neochordae length, extent and shape of the resected leaflet tissue), would facilitate the understanding of the criteria underlying the choice and the tuning of MV repair techniques for a given clinical scenario, thus making the learning curve faster. Furthermore, the potential of MSMs in the context of surgical training could be amplified by the use of virtual reality and of haptic technologies allowing for the physically realistic interaction with the model[44].

4.11 Bibliography

1. Yacoub, M. Anatomy of Mitral Valve, Chordae and Cusps. *J. Cardiovasc.* (1976).
2. Nkomo, V. T. *et al.* Burden of valvular heart diseases: a population-based study. *Lancet* (2006). doi:10.1016/S0140-6736(06)69208-8
3. Nishimura, R. A. *et al.* 2014 AHA/ACC guideline for the management of patients with valvular heart disease: A report of the American College of Cardiology/American Heart Association Task Force on Practice Guidelines. *YMTC* **148,** e1–e132 (2014).
4. Vahanian, A. *et al.* Guidelines on the management of valvular heart disease (version 2012). *Eur. Heart J.* (2012). doi:10.1093/eurheartj/ehs109
5. Drake, D. H., Zimmerman, K. G., Hepner, A. M. & Nichols, C. D. Echo-Guided Mitral Repair. *Circ. Cardiovasc. Imaging* **7,** 132–141 (2014).
6. Anyanwu, A. C. & Adams, D. H. Etiologic Classification of Degenerative Mitral Valve Disease: Barlow’s Disease and Fibroelastic Deficiency. *Semin. Thorac. Cardiovasc. Surg.* **19,** 90–96 (2007).
7. Enriquez-Sarano, M., Akins, C. W. & Vahanian, A. Mitral regurgitation. *Lancet* **373,** 1382–1394 (2009).
8. Votta, E. *et al.* The Geoform Disease-Specific Annuloplasty System: A Finite Element Study. *Ann. Thorac. Surg.* (2007). doi:10.1016/j.athoracsur.2007.03.040
9. Kunzelman, K. S., Reimink, M. S. & Cochran, R. P. Flexible versus rigid ring annuloplasty for mitral valve annular dilatation: a finite element model. *J. Heart Valve Dis.* **7,** 108–116 (1998).
10. Votta, E. *et al.* 3-D computational analysis of the stress distribution on the leaflets after edge-to-edge repair of mitral regurgitation. *J. Heart Valve Dis.* **11,** (2002).
11. Avanzini, A., Donzella, G. & Libretti, L. Functional and structural effects of percutaneous edge-to-edge double-orifice repair under cardiac cycle in comparison with suture repair. *Proc. Inst. Mech. Eng. H.* **225,** 959–971 (2011).
12. Wong, V. M. *et al.* The effect of mitral annuloplasty shape in ischemic mitral regurgitation: A finite element simulation. *Ann. Thorac. Surg.* (2012). doi:10.1016/j.athoracsur.2011.08.080
13. Votta, E. *et al.* Toward patient-specific simulations of cardiac valves: State-of-the-art and future directions. *J. Biomech.* (2013). doi:10.1016/j.jbiomech.2012.10.026

14. Sturla, F. *et al.* Is it possible to assess the best mitral valve repair in the individual patient? Preliminary results of a finite element study from magnetic resonance imaging data. *J. Thorac. Cardiovasc. Surg.* **148,** 1025–1034 (2014).

15. Sturla, F. *et al.* Biomechanical drawbacks of different techniques of mitral neochordal implantation: When an apparently optimal repair can fail. *J. Thorac. Cardiovasc. Surg.* (2015). doi:10.1016/j.jtcvs.2015.07.014

16. Sturla, F. *et al.* Functional and Biomechanical Effects of the Edge-to-Edge Repair in the Setting of Mitral Regurgitation: Consolidated Knowledge and Novel Tools to Gain Insight into Its Percutaneous Implementation. *Cardiovasc. Eng. Technol.* (2015). doi:10.1007/s13239-014-0208-4

17. Choi, A., Rim, Y., Mun, J. S. & Kim, H. A novel finite element-based patient-specific mitral valve repair: Virtual ring annuloplasty. in *Bio-Medical Materials and Engineering* (2014). doi:10.3233/BME-130816

18. Ge, L. *et al.* Measurement of mitral leaflet and annular geometry and stress after repair of posterior leaflet prolapse: Virtual repair using a patient-specific finite element simulation. *Ann. Thorac. Surg.* (2014). doi:10.1016/j.athoracsur.2013.12.036

19. Rim, Y., Choi, A., McPherson, D. D. & Kim, H. Personalized computational modeling of mitral valve prolapse: Virtual leaflet resection. *PLoS One* (2015). doi:10.1371/journal.pone.0130906

20. Baillargeon, B. *et al.* Human Cardiac Function Simulator for the Optimal Design of a Novel Annuloplasty Ring with a Sub-valvular Element for Correction of Ischemic Mitral Regurgitation. *Cardiovasc. Eng. Technol.* (2015). doi:10.1007/s13239-015-0216-z

21. Hammer, P. E., Sacks, M. S., Del Nido, P. J. & Howe, R. D. Mass-spring model for simulation of heart valve tissue mechanical behavior. *Ann. Biomed. Eng.* (2011). doi:10.1007/s10439-011-0278-5

22. Mansi, T. *et al.* An integrated framework for finite-element modeling of mitral valve biomechanics from medical images: Application to MitralClip intervention planning. *Med. Image Anal.* (2012). doi:10.1016/j.media.2012.05.009

23. Grbic, S. *et al.* Personalized mitral valve closure computation and uncertainty analysis from 3D echocardiography. *Med. Image Anal.* (2017). doi:10.1016/j.media.2016.03.011

24. Zhang, F. *et al.* Towards patient-specific modeling of mitral valve repair: 3D transesophageal echocardiography-derived parameter estimation. *Med. Image Anal.* (2017). doi:10.1016/j.media.2016.09.006

25. Hammer, P. E., Del Nido, P. J. & Howe, R. D. Anisotropic mass-spring method accurately simulates mitral valve closure from image-based models. in *Lecture Notes in Computer Science (including subseries Lecture Notes in Artificial Intelligence and Lecture Notes in Bioinformatics)* (2011). doi:10.1007/978-3-642-21028-0_29

26. Tenenholtz, N. A. *et al.* Fast simulation of mitral annuloplasty for surgical planning. in *Lecture Notes in Computer Science (including subseries Lecture Notes in Artificial Intelligence and Lecture Notes in Bioinformatics)* (2013). doi:10.1007/978-3-642-38899-6_13

27. Stevanella, M. *et al.* Mitral Valve Patient-Specific Finite Element Modeling from Cardiac MRI: Application to an Annuloplasty Procedure. *Cardiovasc. Eng. Technol.* (2011). doi:10.1007/s13239-010-0032-4

28. Kunzelman, K. S., Einstein, D. R. & Cochran, R. P. Fluid-structure interaction models of the mitral valve: function in normal and pathological states. *Philos. Trans. R. Soc. Lond. B. Biol. Sci.* **362,** 1393–1406 (2007).

29. Degandt, A. A., Weber, P. A., Saber, H. A. & Duran, C. M. G. Mitral Valve Basal Chordae: Comparative Anatomy and Terminology. *Ann. Thorac. Surg.* (2007). doi:10.1016/j.athoracsur.2007.05.008

30. Lam, J. H., Ranganathan, N., Wigle, E. D. & Silver, M. D. Morphology of the human mitral valve. I. Chordae tendineae: a new classification. *Circulation* **41,** 449–458 (1970).

31. Sturla, F. *et al.* In vitro and in silico approaches to quantify the effects of the Mitraclip® system on mitral valve function. *J. Biomech.* **50,** 83–92 (2016).

32. Lee, C. H., Amini, R., Gorman, R. C., Gorman, J. H. & Sacks, M. S. An inverse modeling approach for stress estimation in mitral valve anterior leaflet valvuloplasty for in-vivo valvular biomaterial assessment. *J. Biomech.* (2014). doi:10.1016/j.jbiomech.2013.10.058

33. Kunzelman, K. S. & Cochran, R. P. Mechanical properties of basal and marginal mitral valve chordae tendineae. *ASAIO Trans.* **36,** M405-8 (1990).

34. Stevanella, M., Votta, E., Lemma, M., Antona, C. & Redaelli, A. Finite element

modelling of the tricuspid valve: A preliminary study. *Med. Eng. Phys.* **32,** 1213–1223 (2010).

35. May-Newman, K. & Yin, F. C. Biaxial mechanical behavior of excised porcine mitral valve leaflets. *Am. J. Physiol.* **269,** H1319-27 (1995).

36. Ritchie, J., Jimenez, J., He, Z., Sacks, M. S. & Yoganathan, A. P. The material properties of the native porcine mitral valve chordae tendineae: An in vitro investigation. *J. Biomech.* (2006). doi:10.1016/j.jbiomech.2005.01.024

37. in *Abaqus 6.10 Documentation* (ed. Dassault Systèmes, Providence, RI, U.) Section 2.4.5 at <http://abaqusdoc.ucalgary.ca/pdf_books/CAE.pdf>

38. Sotaquira, M., Fusini, L., Lang, R. M. & Caiani, E. G. Nearly-Automated Quantification of Mitral Annulus and Leaflet Morphology from Transesophageal Real-Time 3D Echocardiography. *Comput. Cardiol. (2010).* **38,** 145–148 (2012).

39. Topilsky, Y. *et al.* Real-time 3-dimensional dynamics of functional mitral regurgitation: A prospective quantitative and mechanistic study. *J. Am. Heart Assoc.* **2,** 1–17 (2013).

40. Skornitzke, S. *et al.* Mass-spring systems for simulating mitral valve repair using 3D ultrasound images. *Comput. Med. Imaging Graph.* **45,** 26–35 (2015).

41. Adams, D. H., Anyanwu, A. C., Rahmanian, P. B., Filsoufi, F. C. & Adams A C Anyanwu P B Rahmanian F Filsoufi, D. H. Current concepts in mitral valve repair for degenerative disease. *Hear. Fail Rev* **11,** 241–257 (2006).

42. Calleja, A. *et al.* Quantitative Modeling of the Mitral Valve by Three-Dimensional Transesophageal Echocardiography in Patients Undergoing Mitral Valve Repair: Correlation with Intraoperative Surgical Technique. *J. Am. Soc. Echocardiogr.* **28,** 1083–1092 (2015).

43. Ciarka, A. *et al.* Predictors of Mitral Regurgitation Recurrence in Patients With Heart Failure Undergoing Mitral Valve Annuloplasty. *AJC* **106,** 395–401 (2010).

44. Tenenholtz, N. A., Hammer, P. E., Schneider, R. J., Vasilyev, N. V & Howe, R. D. On the Design of an Interactive, Patient-Specific Surgical Simulator for Mitral Valve Repair. *Proceedings of the ... IEEE/RSJ International Conference on Intelligent Robots and Systems. IEEE/RSJ International Conference on Intelligent Robots and Systems* **2011,** 1327–1332 (2011).

Chapter 5

Preliminary morphological and mechanical characterization of the myxomatous mitral valve

5.1 Introduction

Degenerative/myxomatous mitral valve disease (DMVD) is a frequent disorder that affects around 1% of the population[1] and encompasses a spectrum of conditions in which morphological changes in the connective tissue of the mitral valve (MV) cause structural lesions preventing normal function of the MV apparatus. DMVD scenario ranges between two well-known pathologies, namely the fibro-elastic deficiency (FED) and the Barlow's disease (BD). The former is characterized by a single-scallop prolapse or flail with the other segments having generally a normal functioning, although these may be characterized by thinner tissue; the latter exhibits markedly thickened and redundant leaflets tissue with multiple chordal elongation or rupture[2]. Nonetheless, the etiology and the precise evolution of DMVD is still unsure and demanding[2].

Three-dimensional (3D) real-time transesophageal echocardiography (RT-TEE) has been used to accurately assess both the morphological differences[3,4] and the dynamic behavior of DMVD during the cardiac cycle[5,6]. Indeed, several studies proved that such analyses may provide insights to surgical[7,8] or interventional[9,10] repair of DMVD. However, state-of-the-art analyses still suffer of four main issues.

<u>Estimation of MV leaflets thickness</u> - Only recently, Ali et al.[11] performed a quantitative analysis of the MV leaflet thickness in the A2-P2 segments using both 2D TTE and 2D TEE modalities. Pouch et al.[12] and Sotaquira et al.[13] developed semi-automatic software for the 3D morphological characterization of the MV including the regional thickness of the leaflets. However, adopting approximation algorithms within the reconstruction process resulted in nearly homogeneous thickness patterns, thus not allowing to clearly evaluate the local differences between the pathological and physiological tissue.

<u>Mechanical characterization of DMVD tissue disorders</u> - Given that MV tissue in DMVD is characterized by a connective disorder, the mechanical response of myxomatous MV is altered and, to the best of our knowledge, the study proposed by Barber et al.[14] is the unique one which tried to elucidate this aspect. By means of mono-axial tensile tests, they proved the pathological leaflets' tissue to be more extensible as compared to the physiological one. However, such a mechanical test does not effectively mimic the loading condition experienced by MV leaflets during the cardiac cycle, so it does not completely describe the real stress-strain behavior of the tissue.

Numerical simulation of surgical techniques in BD - Moreover, it is known that myxomatous disease can lead to the MV regurgitation[15], which can effectively be treated only repairing the valve through surgical or percutaneous intervention. Nevertheless, the MV anatomical and functional complexity makes surgical treatment technically demanding, requiring low learning curves and much more expertise in the selection of the most effective technique for a given scenario[16]. To aid decision-making process, different research groups proposed computational models based on finite element (FE) approach to reproduce the repair techniques[17–19] simulating MV systolic closure. However, most of the works focus on the simulation of FED disorder, mainly because an accurate description of the BD tissue mechanical responses is still missing.

Optimization of imaging protocols for numerical simulations - As regards, MV biomechanical analysis, the model implementation mainly relies on 3D full volume RT-TEE data. These are elaborated to obtain the MV patient-specific geometrical model. However, to allow for both the reconstruction of a patient-specific MV anatomy and the definition of the kinematic boundary conditions, some demanding technical requirements have to be addressed in the volumetric images acquisitions. In detail, all the MV substructures (annulus, leaflets, papillary muscles - PMs) should be entirely encompassed in the field of view of the acquisition during the full cardiac cycle. Moreover, to correctly define both the annulus and the PMs movement as an input for the simulations, the frame rate of the acquisition should be set at least 20 frames per second[17]. Finally, the image quality of the acquisition should allow for clearly detecting the MV substructures limiting the presence of artifacts. The trade-off among these acquisition features and the inter-observer variability make the definition of the best parameters combination complicated (e.g., wider the field of view is, the larger the voxel dimension will be and less detailed the resulting images), and yet not exhaustively addressed in literature.

In the scenario previously described, we identified the following aims to be tackled:

I. Validation of the method for the annulus reconstruction
II. Quantification of the regional leaflet thickness normal, FED and BD patients
III. Quantification of the mechanical properties of myxomatous leaflets tissue
IV. Application of the patient-specific thickness and the pathological mechanical properties in FE simulation of the valve closure and the evaluation of their effects on final systolic configuration.

5.2 Preliminary validation of the mitral valve annulus reconstruction

The validation process was performed on 21 MVs acquired using the ultrasound imaging system (Philips) equipped with a fully sampled matrix-array TEE transducer (X7-2t). In specific, we analyzed 7 MVs affected by FED, 7 valves affected by BD and 7 normal valves accounted for as controls group.

Data were analyzed with the Mitral Valve Navigator tool (Philips, Amsterdam, The Netherlands), considered as the gold standard, and an in-house custom software tool developed in MATLAB® (The MathWorks Inc., Natick, USA) for the reconstruction of the heart valves.

At the frame of end systole (ES), an expert operator performed the segmentation of MV annulus with the two software tools. The segmentation of the MV complex with the custom software was performed in the following steps:

- The main axes of the mitral valve passing through its centroid was identified
- 18 image planes evenly rotated along the main axes were generated
- On each plane the annulus points, i.e., the hinge points of the leaflets, were defined
- The 36 points obtained were fitted though 4th order Fourier functions to obtain a continuous 3D annular profile[20]

The Antero-Posterior (A-P) diameter was defined as the diameter connecting the local maximum of the anterior annulus to its centroid, while the Anterolateral-Posteromedial (Al-Pm) diameter was computed as the longest distance between two points of the annulus in the direction orthogonal to the A-P diameter.

The normality of data analyzed was tested through D'Agostino and Pearson test and the data are reported as mean ± standard deviation (Tab. 5.1). The correlation coefficient (r) of the measurement obtained with the two software were compared and the Bland-Altmann analysis was performed (Tab. 5.1).

Table 5. 1 Values of the area (2D A) and the perimeter (3D) of mitral annulus and the measures of the antero-posterior and anterolateral-posteromedial (Al-Pm) diameters, the Bland-Altman analysis and the correlation.

	Custom Software	**Mitral Valve Navigator**	**Bland-Altman**		**Correlation**
	Mean ± SD	**Mean ± SD**	**Bias [%]**	**CV [%]**	**r**
$D_{Al\text{-}Pm}$ [mm]	47.6 ± 6.8	47.3 ± 7.0	-0.58	2.52	0.97
$D_{A\text{-}P}$ [mm]	41.5 ± 5.3	42.2 ± 5.8	1.39	4.51	0.96
3D P [mm]	146.4 ± 19.1	149.4 ± 20.1	2.02	2.75	0.97
2D A [mm2]	1567.2 ± 418.9	1564.6 ±430.7	-0.27	3.23	0.98

Overall, measured variables were characterized by **r** values higher than 0.95 and the maximum absolute bias and the coefficient of variation were 2.02% and 4.51% respectively. This preliminary analysis, underlines the excellent agreement between the measurements performed with the two software and highlights the accuracy of the custom software.

5.3 Assessment of leaflet thickness distribution in controls, Fibro Elastic Deficiency and Barlow Mitral Valve

Using a GE Vivid 9 system (GE Healthcare, Horten, Norway) with a 3D zoom single beat acquisition, the analysis was performed on 20 patients diagnosed with severe MV regurgitation of degenerative etiology, involving at least the posterior mid-scallop (P2). In particular, 10 patients presented FED of the MV, defined by echocardiographic assessment as an isolated prolapse or flail of P2 with none or moderate annular dilatation. The other 10 patients were affected by BD, defined as prolapse of both leaflets or involving multiple scallops with chordal elongation and with severe annular dilatation[2]. In addition, 10 subjects with normal MV anatomy undergoing TEE for different clinical reasons were included as control group.

Acquisitions were free from artifacts and were characterized by an almost isotropic spatial resolution in the range of 0.3-0.6 mm. The frame ranged from 5 to 12 frames per second.

Each dataset was semi-automatically processed exploiting a novel custom platform completely developed in MATLAB® (The MathWorks Inc., Natick, USA). The segmentation was performed at the frame of mid-systole that was defined as midway frame between the closure and the opening of MV.

The corresponding volume was navigated and MV commissures and the inter-commissural diameter were manually defined. Subsequently, 10 long-axis equally spaced cut planes were defined between 20% and 80% of the extent of the inter-commissural diameter (Fig. 5.1.a), to obtain a clear distinction between anterior and posterior in all the analyzed planes. Each cut plane was perpendicular to the MV annular plane and has a normal inter-commissural diameter. On each cut plane, the annulus and the free margin were traced on both leaflet profiles (Fig. 5.1.b). Finally, an expert operator defined the cut-planes in which the anterior or the posterior leaflet were prolapsing.

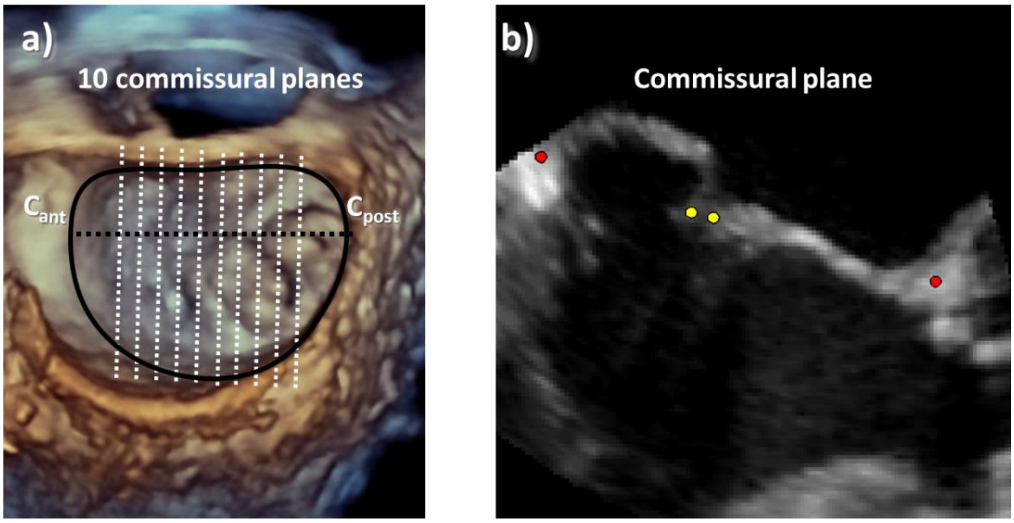

Figure 5.1 – Top view of mitral valve from 3D TEE with a schematic representation of **a)** the 10 commissural planes. The annulus is depicted with a black line while C_{ant} e C_{post} indicate the two commissures of the valve. **c)** Representation of one commissural plane in which the annulus (red points) and free margin (yellow points) of the MV leaflets are highlighted.

After the definition of the binary mask of the leaflet derived from the cut plane (Fig 5.2.a-b), real-time extraction of the local leaflet skeleton (Fig. 5.2.b), i.e. the leaflet medial axis, the atrial (superior part of light blue pixels in Fig. 5.2.c) and ventricular (inferior part of light blue pixels in Fig. 5.2.c) borders were automatically accomplished following an established approach[13]. Finally, the local thickness of the leaflet (Fig. 5.2.c) was locally computed as the distance between the ventricular and the atrial border. The local thickness was computed at three different positions along the leaflet profile: distal, middle and proximal, respectively (Fig. 5.2.d).

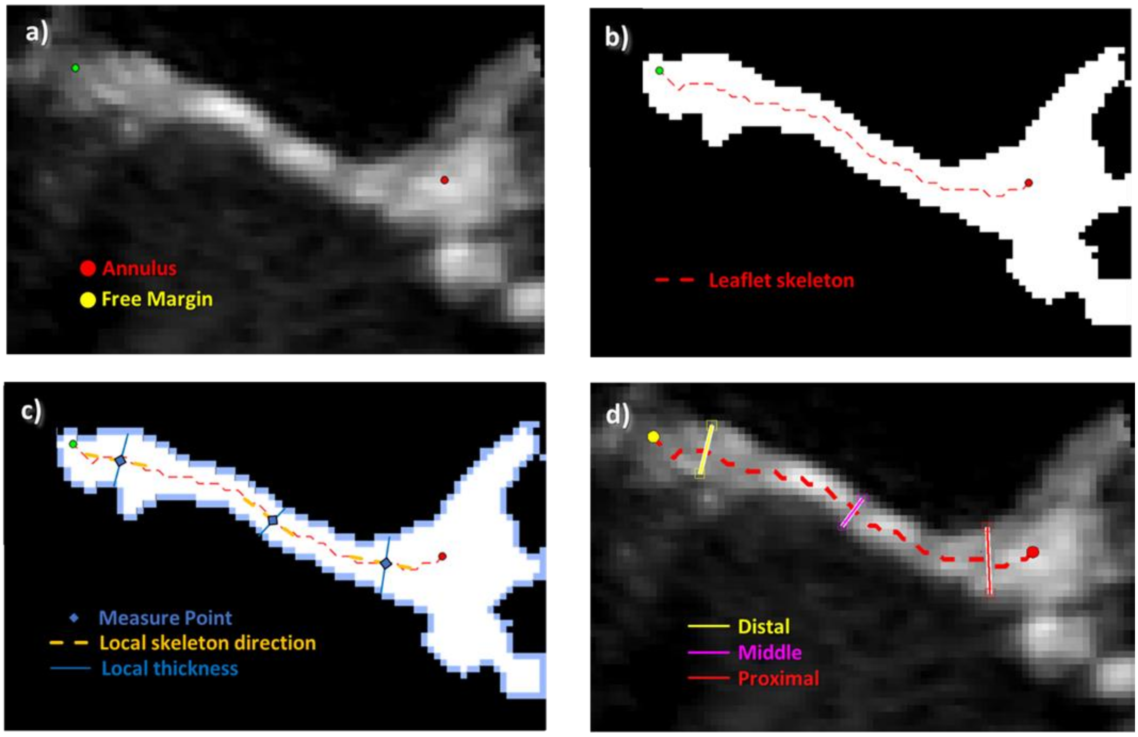

Figure 5. 2 – **a)** Zoom of one leaflet plane in which the annulus (red point) and free margin (yellow point) are highlighted. **b)** Binary mask of the leaflet with its skeleton (red dashed line). **c)** Measure points (blue squares) of the thickness (blue lines) defined using the local skeleton direction (orange dashed line) and the borders of the mask (light blue pixels). **d)** Representation of the thickness measured in proximal (red), middle (magenta) and distal (yellow) position.

In order to obtain the surface of each leaflet, we converted in a 3D space the plane coordinates of the skeleton leaflet points obtained from the 10 commissural planes (Fig. 5.3.a). Subsequently, we oversampled the raw points of the skeleton using a 3D spline (Fig. 5.3.b-c) and we generated a surface that we used to represent the regional thickness yielded fitting the thickness measurements (Fig. 5.3.d).

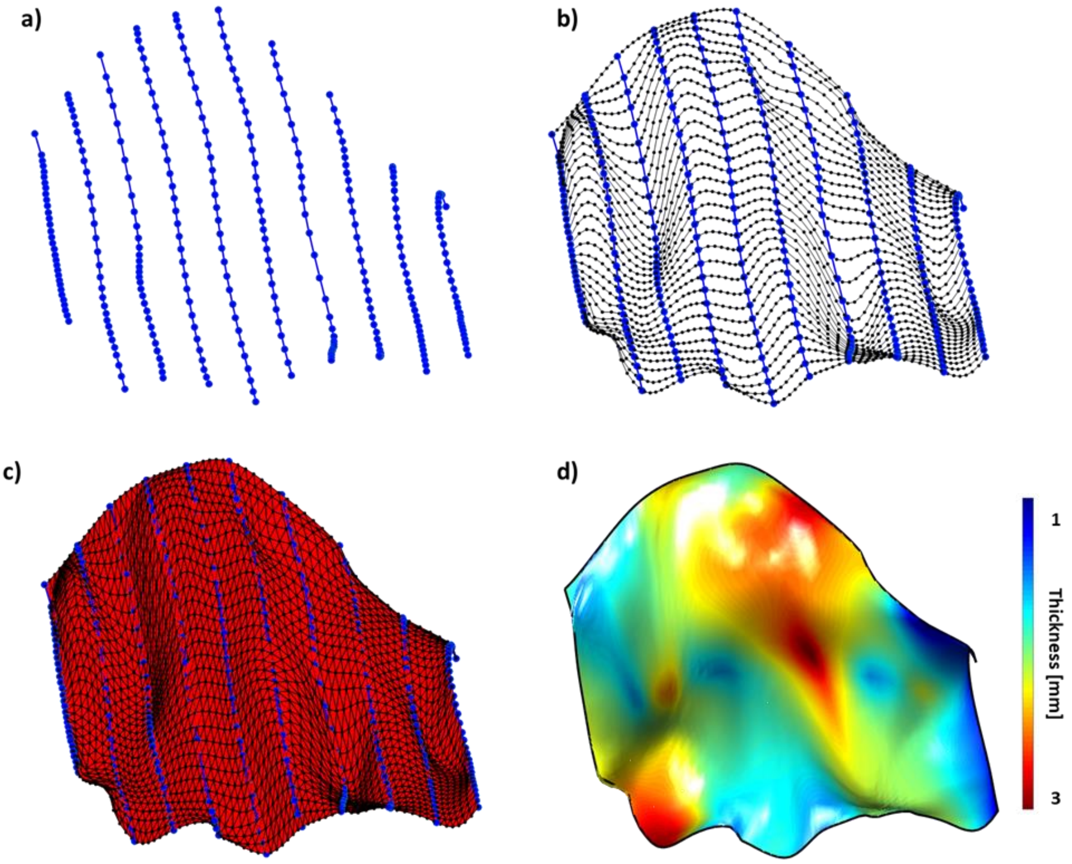

Figure 5.3 – **a)** 3D coordinates of the skeleton (blue lines with dots) leaflets points obtained from the 10 commissural planes. **b)** Oversample of the initial raw points using 3D splines (black lines). **c)** Mesh of triangular elements that represent leaflet surface. d) Colormap of the regional thickness obtained fitting the thickness measurements.

The thickness of the anterior and posterior leaflets was computed considering the respective measurements performed in all the planes in distal, mid and proximal position. Analogously, the thickness of prolapsing region was computed considering only the measurements obtained in the prolapse segments of the leaflets.

Data are expressed through the median, 25th and 75th percentile. Comparison of measurements among the different groups was performed through non-parametric Kruskal-Wallis test and Post hoc Dunn's test. Differences were considered statistically significant with $p<0.05$. All the statistical computations were performed in GraphPad Prism 7 (GraphPad Software Inc., La Jolla, CA, USA).

In a subset of 6 randomly selected patients (2 Normal, 2 FED and 2 BD) resulting in a total of 360 thickness measurements, intra-observer and inter-observer variability of thickness data were evaluated. Thickness measurements were re-performed 4 weeks later by the main investigator and by a second independent observer in double-blind conditions. Intra- and inter-variability was evaluated using the coefficient of variability (CV) (defined by the ratio of the standard deviation of the pair measures as a percent of their mean) and Bland-Altman analysis.

5.3.1 Qualitative analysis

For each group, the MV models of three subjects, reconstructed at mid-systole, were represented and color-coded according to their measured regional thickness (Fig. 5.4).

Both in FED and BD valves, according with the literature[2,15], the prolapsing zone is evident but in the first case this zone is narrow and is located mainly in the P2 zone, while in the second it comprises a wider zone that can include both anterior and posterior thickness (Fig. 5.4).

The MV of the normal group are characterized by a physiological configuration (no prolapsing zone) and homogenous distribution of the thickness.

On the contrary, FED valves were characterized by a clear discontinuity between the thickness of the prolapsing region and the other parts of the tissue, which indeed have a thickness distribution comparable to that of normal valves.

The thickness distribution of BD valves appeared markedly different respect to normals and FED, both considering the regional extension of high-thickness regions and the pattern inhomogeneity over the entire valve.

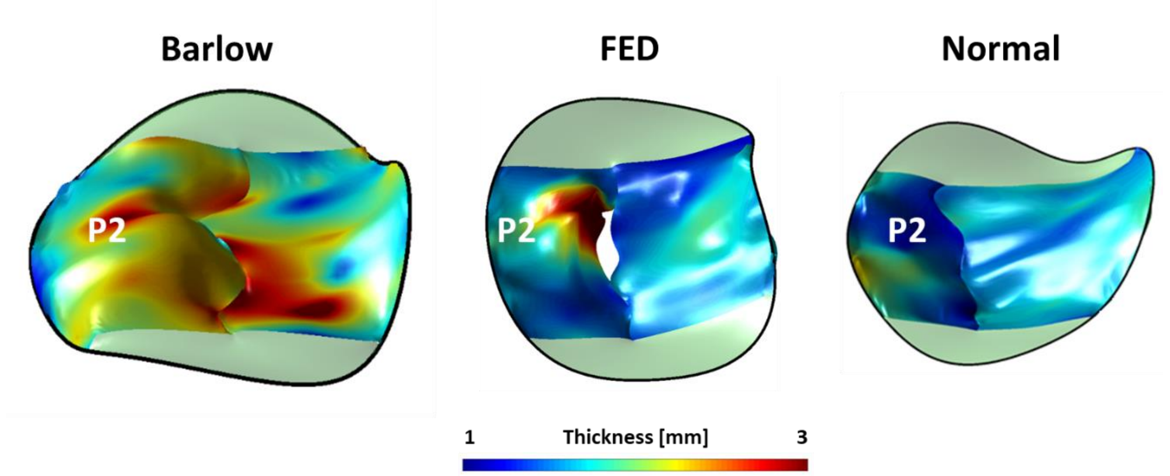

Figure 5.4 – Illustrative mitral valve models of three subjects (1 Barlow, 1 FED and 1 Normal) representing the respective thickness distribution.

5.3.2 Quantitative analysis

Quantitative analysis was performed comparing the measurements performed on the anterior and posterior leaflet, and those one measured on the prolapsing and no-prolapsing region (Tab. 5.2).

Measurements performed on the anterior leaflet of the three groups are significantly different (P value adjusted < 0.0001). In particular, the Dunn's test confirmed the qualitative hypothesis that anterior thickness of Barlow Patients is significantly bigger than FED (P value adjusted = 0.0001) and normal (P value adjusted = 0.0001).

For the three groups, the thickness measurements in the no prolapsing region were significantly different and the adjusted P-value of BD vs. FED and BD vs. normal was lower than 0.001.

Similarly, for the measurements on the posterior leaflet, the thickness distribution of the three groups differed significantly (P value adjusted < 0.0001).

Considering FED and BD groups, we compared the thickness measurements in the prolapsing region with the other ones. In BD valves, no significant differences were observed (P value adjusted equal to 0.7321), whereas in FED they were significantly different with an adjusted P-value lower than 0.0001.

Both inter- and intra- observer had a coefficient of variation lower than 20.0%. In particular, 15.2% and 9.7% respectively, and in both cases the bias is negligible (-0.5% for inter- and -1.4% for intra- observer analysis).

Table 5.2 – Thickness values for the three groups analyzed (Barlow, FED and Normal). Data are expressed as median (25th – 75th percentile). Kruskal-Wallis test (Dunn's post hoc): * $p < 0.05$ versus normal; $^{\#}$ $p < 0.05$ versus FED.

Leaflet thickness [mm]	**BD**	**FED**	**Normal**	***P***
Anterior Leaflet	2.02 (1.75 – 2.35) $^{*\#}$	1.49 (1.34 – 1.69)	1.49 (1.29 – 1.72)	< .0001
Posterior Leaflet	1.85 (1.60 – 2.26) $^{*\#}$	1.65 (1.44 – 1.91) *	1.42 (1.23 – 1.65)	< .0001
Prolapsing Region	1.93 (1.65 – 2.38)	1.83 (1.56 – 2.25)	–	0.0549
No-Prolapsing Region	1.96 (1.66 – 2.27) $^{*\#}$	1.50 (1.34 – 1.71) *	1.46 (1.26 – 1.69)	< .0001

5.3.3 Application of patient specific thickness in finite element mitral valve model

The workflow described in the previous chapter was used to define the patient-specific thickness of the FE model to evaluate the effects of this characteristic on the final computed systolic configuration.

A preliminary analysis was performed on a single case of BD-affected MV. The volumetric data were acquired using a GE Vivid 9 system (GE Healthcare, Horten, Norway) with a full volume acquisition gated on six cardiac cycles with 31 frames per cycle and a spatial resolution of 0.56mmX0.56mmX0.62mm.

In this case, the segmentation was performed on 18 radial planes evenly rotated along the long axis of the MV at the frame of late diastole because these parameter setting is required to correctly the initial MV model of the FE simulation. In Fig. 5.5 is depicted the computed patient-specific thickness pattern.

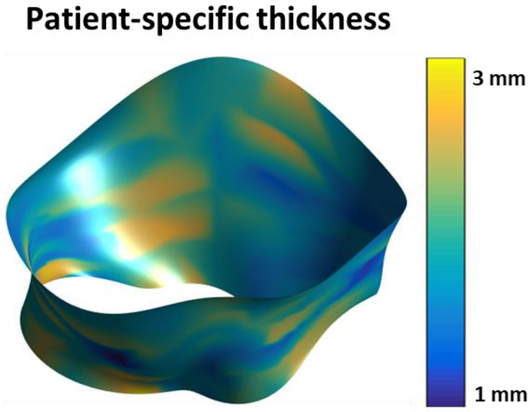

Figure 5.5 – Colormap of the mitral valve patient-specific regional thickness.

The physiologic systolic closure was simulated through the same FE modeling as in[21], in two variants, i.e., with the paradigmatic thickness pattern[22] and with the computed patient-specific distribution.

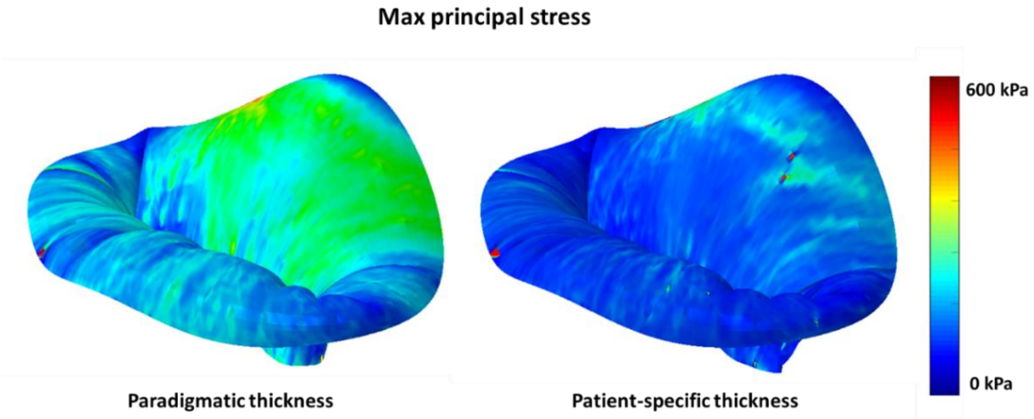

Figure 5.6 – Colormap of the maximum principal stress on the valve simulated with paradigmatic thickness (left) and with the patient specific pattern (right).

The different thickness pattern strongly affects the stress distribution on the MV leaflets. In particular, in the anterior leaflet the mean maximum principal stress with the paradigmatic thickness is 145 kPa while the same parameter obtained with the patient-specific thickness is equal to 54 kPa.

5.4 Mechanical analysis of the myxomatous leaflet tissue

Six specimens of human myxomatous MV leaflets resected during surgical repair were saved and preserved at -80 °C. Square-shaped samples (approximate size 3500x3500 µm) were cut from the specimens, with the sides parallel and normal to the annulus, i.e. aligned with the radial and circumferential direction of the leaflets. After defreezing, displacement-controlled equi-biaxial tests were run on the samples at constant temperature (in a 37 °C phosphate-buffered saline (PBS) bath) and strain rate (60 µm/s). Following five preconditioning loading-unloading cycles, samples were biaxially stretched up to 40% nominal deformation. A BioTester machine (Cellscale) with a 1.5 N loadcell was used.

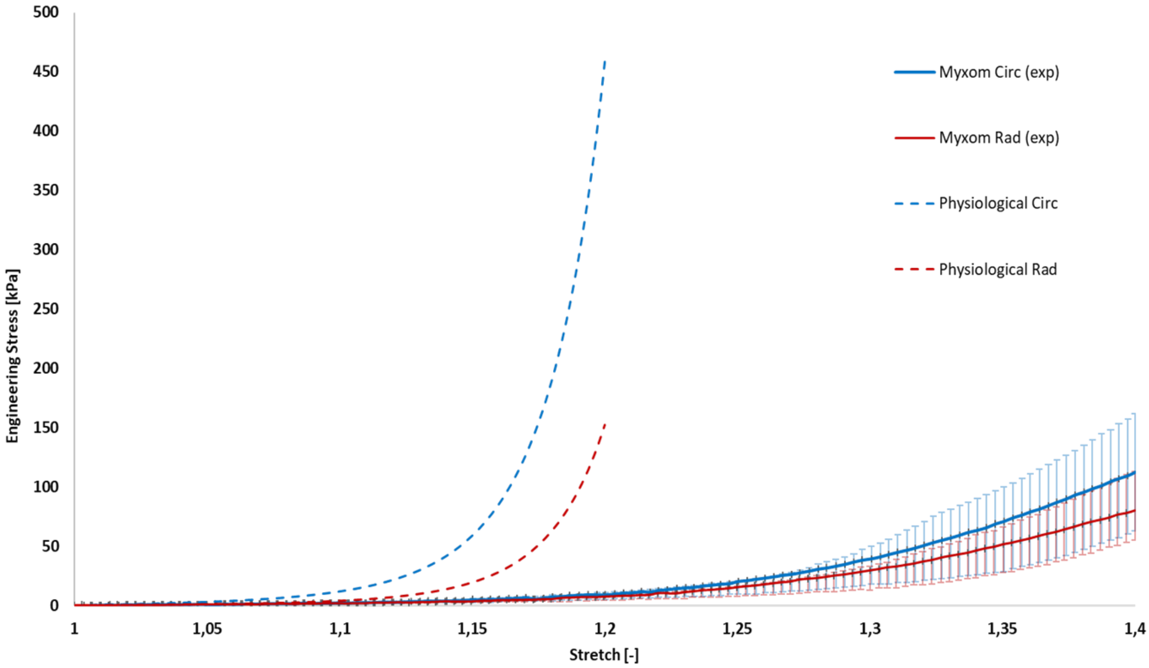

Figure 5.7 – Experimental Stretch-Stress curves of physiological[23] (dashed lines) and myxomatous (continuous lines) leaflet tissue in radial (red) and circumferential (blue) direction. The myxomatous curves are represented with the 25th and 75th percentile of the stress values.

Stress-strain data were fitted to identify the constitutive parameters of the hyperelastic and transversely isotropic strain energy function by Lee[24].

The physiologic closure of an anatomically detailed MV was simulated through FE modeling as in[21], and in two variants, i.e. with physiological and pathological mechanical properties of MV leaflets, respectively.

5.4.1 Biaxial testing

Myxomatous leaflets resulted less anisotropic and more extensible than physiological leaflets[23] (Fig. 5.7). In both directions, the toe-region of the stress-strain curves was shifted by approximately 15% in nominal strains. Peak stresses were lower by 78% and 54% in the circumferential and radial direction, respectively.

5.4.2 Finite element simulations

At peak systole, the two variants of the model yielded a different configuration of MV leaflets, whose position locally differed by 0-9.8 mm (50th percentile equal to 2.17 mm). Consistently, computed maximum principal strains were dramatically larger when accounting for the mechanical properties of myxomatous leaflets (Fig. 5.8).

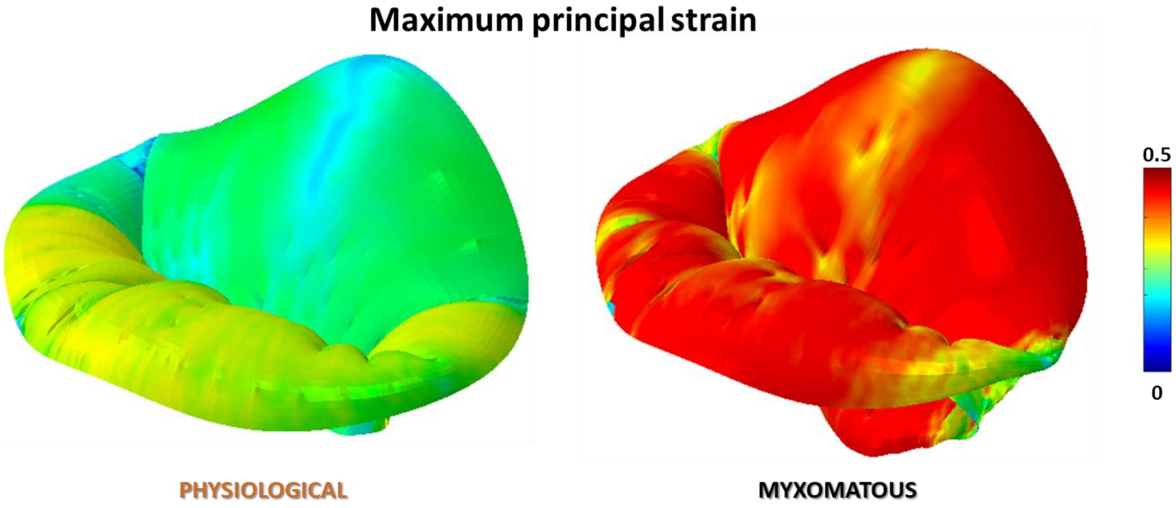

Figure 5.8 – Colormap of the maximum principal strain on the valve simulated with physiological (left) and myxomatous tissue conditions (right).

5.5 Conclusions

First, the comparison between the results obtained by the commercial and the custom software showed an excellent match highlighting the reliability of the developed method for the reconstruction of mitral valve annular sub-structure.

Second, both the qualitative and quantitative analysis of the thickness measurements confirmed data reported in literature, but yielded a more realistic patient-specific 3D pattern.

Third, myxomatous leaflets resulted less anisotropic and more extensible than physiological leaflets. Finally, the implementation of the data obtained by the morphological and mechanical analysis of the myxomatous tissue in the FE simulation affects strongly the final systolic configuration and its biomechanics. Consequently, in the future, these new parameters should be included to improve the specificity of the biomechanical models.

5.6 Bibliography

1. Adams, D. H., Rosenhek, R. & Falk, V. Degenerative mitral valve regurgitation: Best practice revolution. *Eur. Heart J.* **31,** 1958–1967 (2010).
2. Anyanwu, A. C. & Adams, D. H. Etiologic Classification of Degenerative Mitral Valve Disease: Barlow's Disease and Fibroelastic Deficiency. *Semin. Thorac. Cardiovasc. Surg.* **19,** 90–96 (2007).
3. Chandra, S. *et al.* Characterization of degenerative mitral valve disease using morphologic analysis of real-time three-dimensional echocardiographic images objective insight into complexity and planning of mitral valve repair. *Circ. Cardiovasc. Imaging* **4,** 24–32 (2011).
4. Maffessanti, F. *et al.* Quantitative analysis of mitral valve apparatus in mitral valve prolapse before and after annuloplasty: A three-dimensional intraoperative transesophageal study. *J. Am. Soc. Echocardiogr.* **24,** 405–413 (2011).
5. Grewal, J. *et al.* Mitral annular dynamics in myxomatous valve disease: new insights with real-time 3-dimensional echocardiography. *Circulation* **121,** 1423–31 (2010).
6. Clavel, M. A. *et al.* Dynamic phenotypes of degenerative myxomatous mitral valve disease: quantitative 3-dimensional echocardiographic study. *Circ. Cardiovasc. Imaging* **8,** (2015).
7. David, T. E., Armstrong, S., McCrindle, B. W. & Manlhiot, C. Late Outcomes of Mitral Valve Repair for Mitral Regurgitation Due to Degenerative Disease. *Circulation* **127,** 1485–1492 (2013).
8. Suri, R. M. *et al.* Robotic mitral valve repair for all prolapse subsets using techniques identical to open valvuloplasty: establishing the benchmark against which percutaneous interventions should be judged. *J. Thorac. Cardiovasc. Surg.* **142,** 970–9 (2011).
9. Ancona, F. *et al.* Multimodality imaging of the tricuspid valve with implication for percutaneous repair approaches. *Heart* **103,** 1073–1081 (2017).
10. Delgado, V., van der Kley, F., Schalij, M. J. & Bax, J. J. Optimal imaging for planning and guiding interventions in structural heart disease: a multi-modality imaging approach. *Eur. Hear. J. Suppl.* **12,** E10–E23 (2010).
11. Ali, S. G. *et al.* Detailed Transthoracic and Transesophageal Echocardiographic Analysis of Mitral Leaflets in Patient Undergoing Mitral Valve Repair. *Am. J.*

Cardiol. **118,** 113–120 (2016).

12. Pouch, A. M. *et al.* Modeling the Myxomatous Mitral Valve With Three-Dimensional Echocardiography. *Ann. Thorac. Surg.* **102,** 703–710 (2016).
13. Sotaquira, M. *et al.* Semi-automated segmentation and quantification of mitral annulus and leaflets from transesophageal 3-D echocardiographic images. *Ultrasound Med. Biol.* **41,** 251–67 (2015).
14. Barber, J. E. *et al.* Mechanical properties of myxomatous mitral valves. *J. Thorac. Cardiovasc. Surg.* **122,** 955–962 (2001).
15. Adams, D. H., Anyanwu, A. C., Rahmanian, P. B. & Filsoufi, F. Current concepts in mitral valve repair for degenerative disease. *Heart Fail. Rev.* **11,** 241–257 (2006).
16. Drake, D. H., Zimmerman, K. G., Hepner, A. M. & Nichols, C. D. Echo-Guided Mitral Repair. *Circ. Cardiovasc. Imaging* (2013). at <http://circimaging.ahajournals.org/content/early/2013/11/11/CIRCIMAGING.112.000458.abstract>
17. Sturla, F. *et al.* Biomechanical drawbacks of different techniques of mitral neochordal implantation: When an apparently optimal repair can fail. *J. Thorac. Cardiovasc. Surg.* **150,** 1303–1312 (2015).
18. Stevanella, M. *et al.* Mitral Valve Patient-Specific Finite Element Modeling from Cardiac MRI: Application to an Annuloplasty Procedure. *Cardiovasc. Eng. Technol.* **2,** 66–76 (2011).
19. Rim, Y., Laing, S. T., McPherson, D. D. & Kim, H. Mitral valve repair using ePTFE sutures for ruptured mitral chordae tendineae: A computational simulation study. *Ann. Biomed. Eng.* **42,** 139–148 (2014).
20. Sturla, F. *et al.* Dynamic and quantitative evaluation of degenerative mitral valve disease: A dedicated framework based on cardiac magnetic resonance imaging. *J. Thorac. Dis.* **9,** (2017).
21. Sturla, F. *et al.* In vitro and in silico approaches to quantify the effects of the Mitraclip system on mitral valve function. *J. Biomech.* (2016). doi:10.1016/j.jbiomech.2016.11.013
22. Kunzelman, K. S., Einstein, D. R. & Cochran, R. P. Fluid-structure interaction models of the mitral valve: function in normal and pathological states. *Philos. Trans. R. Soc. Lond. B. Biol. Sci.* **362,** 1393–1406 (2007).

23. Pham, T., Sulejmani, F., Shin, E., Wang, D. & Sun, W. Quantification and comparison of the mechanical properties of four human cardiac valves. *Acta Biomater.* **54,** 345–355 (2017).

24. Lee, S. J. *et al.* Midterm results of mitral valve repair with lifting annuloplasty strip for acute phase infective endocarditis. *J. Cardiothorac. Surg.* **10,** 139 (2015).

Chapter 6

Conclusive Remarks

6.1 Main findings

This work was focused on the morphological and biomechanical analysis of the heart valves exploiting the volumetric data.

Novel methods were implemented to perform cardiac valve structure and sub-structure segmentation by defining long axis planes evenly rotated around the long axis of the valve. These methods were exploited to successfully reconstruct the 3D geometry of the mitral, tricuspid and aortic valve structures. Firstly, the reconstructed models were used for the morphological analysis providing a detailed description of the geometry of the valve structures, also computing novel indexes that could improve the description of the valvular apparatus and help their clinical assessment. Additionally, the models obtained for the mitral valve complex were adopted for the development of a novel biomechanical approach to simulate the systolic closure of the valve, relying on highly-efficient mass-spring models thus obtaining a good trade-off between the accuracy and the computational cost of the numerical simulations.

In specific:

- First, an innovative and semi-automated method was implemented to generate the 3D model of the aortic valve and of its calcifications, to quantitively describe its 3D morphology and to compute the anatomical aortic valve area (AVA) based on multi-detector computed tomography images. The comparison of the obtained results vs. effective AVA measurements showed a good correlation. Additionally, these methods accounted for asymmetries or anatomical derangements, which would be difficult to correctly capture through either effective AVA or planimetric AVA.

- Second, a tool to quantitively assess the geometry of the tricuspid valve during the cardiac cycle using multidetector CT was developed, in particular focusing on the 3D spatial relationship between the tricuspid annulus and the right coronary artery. The morphological analysis of the annulus and leaflets confirmed data reported in literature. The qualitative and quantitative analysis of the spatial relationship could standardize the analysis protocol and be pivotal in the procedure planning of the percutaneous device implantation that interact with the tricuspid annulus.

- Third, we simulated the systolic closure of three patient specific mitral valve models, derived from CMR datasets, by means of the mass spring model approach. The comparison of the obtained results vs. finite element analyses (considered as the gold-standard) was performed tuning the parameters of the mass spring model, so to obtain the best trade-off between computational expense and accuracy of the results. A configuration mismatch between the two models lower than two times the in-plane resolution of starting imaging data was yielded using a mass spring model set-up that requires, on average, only ten minutes to simulate the valve closure.

- Finally, in the last chapter, we performed a comprehensive analysis which aimed at exploring the morphological and mechanical changes induced by the myxomatous pathologies in the mitral valve tissue. The analysis of mitral valve thickness confirmed the data and patterns reported in literature, while the mechanical test accurately described the behavior of the pathological tissue. A preliminary implementation of this data into finite element simulations suggested that the use of more reliable patient-specific and pathology-specific characterization of the model could improve the realism and the accuracy of the biomechanical simulations.

6.2 Future Developments

On the basis of the present work, a few main research directions appear as important steps for future developments. In this PhD project, the potential and possible clinical impact of the developed tools has been shown. Despite the algorithms for the quantitative description of the 3D morphology are completely automatic, the segmentation process still requires numerous inputs of the end-user, thus increasing the time necessary to process a single dataset. This aspect could limit the use of the tools especially considering large cohort patients. However, to overcome this limit, machine learning algorithms based on adaptive models or deep learning could be implemented and exploited to drastically reduced the segmentation step current time. Good results using this technology has been reported in literature[1–4] , even though, in the initial phase, this class of algorithms require several datasets to implement the training process of the machine learning models. The exploitation of such automated approaches would require a robust validation process of the reconstruction algorithms. This issue could be addressed, for example, performing imaging acquisitions (e.g., 3D echocardiography) on ex-vivo beating heart mock loops[5]; in this way, virtually reconstructed models, and all their morphological characteristics (e.g., leaflets thickness), could be compared with physical measurements of the same valvular leaflet tissue.

Finally, to test the diagnostic and prognostic potential of the computed variables and proposed indexes, a retrospective study on a large cohort of patients is suggested.

6.3 Bibliography

1. Zreik, M. *et al.* Deep learning analysis of the myocardium in coronary CT angiography for identification of patients with functionally significant coronary artery stenosis. *Med. Image Anal.* **44,** 72–85 (2018).
2. Lugo-Fagundo, C., Vogelstein, B., Yuille, A. & Fishman, E. K. Deep Learning in Radiology: Now the Real Work Begins. *J. Am. Coll. Radiol.* (2017). doi:10.1016/j.jacr.2017.08.007
3. Grbic, S. *et al.* Personalized mitral valve closure computation and uncertainty analysis from 3D echocardiography. *Med. Image Anal.* **35,** 238–249 (2017).
4. Grbic, S. *et al.* Complete valvular heart apparatus model from 4D cardiac CT. *Med. Image Anal.* **16,** 1003–1014 (2012).
5. Vismara, R. *et al.* Transcatheter Edge-to-Edge Treatment of Functional Tricuspid Regurgitation in an Ex Vivo Pulsatile Heart Model. *J. Am. Coll. Cardiol.* **68,** 1024–1033 (2016).